Beauty and the leptons.

par **Francesco Polci**

Thèse d'habilitation a diriger la recherche

Thèse présentée et soutenue publiquement le 18/12/2025

Membres du jury:

Examinateur: M. Benjamin Fuks

Rapporteuse: Mme. Emi Kou

Rapporteuse: Mme. Julie Malcles

Examinateur: M. Jose Ocariz

Rapporteuse: Mme. Isabelle Ripp-Baudot

Examinatrice: Mme. Ana Margarida Teixeira

Contents

Introduction

The Standard Model of particle physics remains the most successful theoretical framework for describing the fundamental interactions among elementary particles. Developed in the 1960s, it provides a remarkably predictive and mathematically consistent description of known particles and their interactions. Its predictions have been extensively tested and validated over decades, particularly through high-precision experiments at various facilities, among which the Large Hadron Collider (LHC) in recent years. Despite its remarkable achievements, the Standard Model is incomplete: it cannot account for several key experimental observations, such as neutrino oscillations, dark matter, or the matter-antimatter asymmetry of the universe. Moreover, it offers no clear resolution to some deep theoretical issues, including the hierarchy problem, the origin of flavor, or the strong CP problem.

A variety of experimental strategies have been developed to test the Standard Model in different sectors, and flavor physics plays a particularly important role in this effort. Within this field, studying b-quark transitions with leptons in the final state presents distinct advantages. From an experimental standpoint, electrons and muons yield clean and identifiable signatures. From a theoretical perspective, these processes offer a valuable window to explore new effects and deepen our understanding of the underlying symmetries and limitations of the Standard Model.

The LHCb experiment, that I joined in 2011, is a perfect environment for these studies. The LHC has furnished and keeps delivering a large luminosity to the experiment. Therefore, decays that where previously observed in a limited dataset are now collected in relevant number, so that their branching fractions and properties can be measured with a good precision. In particular, semileptonic decays of the type $b \to s\ell\ell$, where ℓ represents a lepton, give access to a number of observables for which Standard Model predictions can be done and compared with experimental results. In addition, decays never observed before are now at hands. The features of the LHCb detector allow to identify leptons of the three families, providing the capability of performing lepton flavor universality tests and searches for lepton flavor violating decays, which are both very powerful for constraining physics beyond the Standard Model.

In the past few years, some discrepancies with respect to the Standard Model predictions have been observed in the angular distributions and branching fractions measurements of $b \to s\ell\ell$ decays. Some of them have been confirmed by recent results and by other experiments, some others not. Phenomenological studies based on effective field theory show that these deviations could be sign of physics beyond the Standard Model, generically mediated by a new vector boson Z' or leptoquarks. However, the current precision of these measurements is

not enough to claim such an evidence. Additional studies and larger data sets are needed to keep clarifying the nature of these deviations.

This document provides an overview of the $b \to s\ell\ell^{(\prime)}$ searches in which I have been involved. The first is the angular analysis of $B^0 \to K^{*0}\mu^+\mu^-$ decays. Its branching ratio can be written as function of four kinematic variables, the invariant mass of the di-muon system and the three angles describing the distribution of the final state particles. The coefficients multiplying the functions of the three angles in a defined helicity basis are called "angular observables". Comparing their measurements with the theoretical predictions provides a test of the Standard Model. The analysis discussed here was published in 2016 [1] and uses all the data collected in the first run of LHC, corresponding to an integrated luminosity of 3 fb^{-1}. The compatibility of the measurement with the Standard Model predictions was at 3.4 standard deviations. The theoretical community interpreted the result has a possible underestimation of some hadronic uncertainties or by possible hints of new physics contributions.

The second measurement is a test of lepton flavor universality. This expression design the characteristic of the Standard Model gauge bosons of coupling with the same magnitude to all the leptons, independently of the generation they belong to, apart from mass effects. For example, the ratio R_{K^*} between the $B^0 \to K^{*0}\mu^+\mu^-$ and $B^0 \to K^{*0}e^+e^-$ branching ratios is expected to be the unity. This is a very precise theoretical prediction, as kinematic effects due to the different mass of electrons and muons are lower than percent. The first measurement of R_{K^*}, described here, was published in 2017 [2]. It was performed in two regions of the invariant mass of the di-lepton system, characterized by different elementary processes, and showed a compatibility with the Standard Model at the level of 2.5 standard deviations.

Finally, three searches for lepton flavor violating decays will be discussed, covering the three possible lepton flavor combinations in $b \to s\ell\ell^{'}$ decays: $B^+ \to K^+\mu^\pm e^\mp$ [3], $B^0 \to K^{*0}\tau^\mp\mu^\pm$ [4] and $B^0 \to K^{*0}\tau^\mp e^\pm$ [5]. These decays, extremely suppressed in the Standard Model and well beyond any current experimental sensitivity, are enhanced to an observable level in some new physics scenario. Therefore, their observation would be an unambiguous proof of physics beyond the Standard Model. When not observed, the upper limits set on their branching fractions provide strong constraints on alternative models.

The document will underline the common aspects and specific features of each of these measurements. The first chapter 1 will provide an overview of the theoretical framework and the definition of the observables that will be measured. Chapter 2, instead, provides an overview of the strategy used to select the decay candidates and reject the various categories of backgrounds which affect these analyses. The following chapters will describe the angular analysis (chapter 3), the test of lepton flavor universality (chapter 4) and the searches for lepton flavor violating decays (chapter 5), respectively. Within these three chapters it will be shown how the relevant distributions of the candidates surviving the selections undergo extended maximum likelihood fits to statistically discriminate the residual backgrounds and determine the observables of interest. The determination of the systematic uncertainties are also described. Despite the fact that, in all the analyses discussed here, the systematic uncertainties are significantly smaller than the statistical uncertainties, it is important to address their impact. In fact, with future larger data sets, the statistical uncertainty will

reduce, challenging the systematic limitations. The last chapter 6 discusses the current status of these searches and the future prospects, including an overview of my future research projects.

The works described in this document are the outcome of the collaborations with various LHCb colleagues. These include PhD students and postdocs that I had the opportunity to supervise and to whom I wish to give credits for this work: Samuel Coquereau for the angular analysis and the lepton flavor universality test; Giulio Dujany, Andrea Mogini and Steffen George Weber for the $B^0 \to K^{*0}\tau^{\mp}\mu^{\pm}$ search and Tommaso Fulghesu for the $B^0 \to K^{*0}\tau^{\mp}e^{\pm}$ search.

Chapter 1

The $b \to s\ell\ell^{(\prime)}$ transitions: probes of physics beyond the Standard Model

The $b \to s\ell\ell$ transitions, where ℓ indicates a lepton, are flavour-changing neutral-current (FCNC) processes in which a quark changes its flavour without altering its electric charge. The Standard Model (SM) forbids FCNCs at tree level and only allows amplitudes involving loop Feynman diagrams. The absence of a dominant tree-level SM contribution implies that $b \to s\ell\ell$ transitions are rare and, therefore, sensitive to the existence of new particles that could intervene in the loops as virtual particles. Therefore, $b \to s\ell\ell$ decays are an ideal laboratory to test the SM and demonstrate the effects of new physics (NP). Their high sensitivity to the presence of new particles allows one to constrain many models alternative to the SM.

The $b \to s\ell\ell'$ transitions, where the two leptons have different flavours, imply that the lepton flavor is not conserved. Lepton-flavour violating decays are said to be forbidden in the SM because they could only happen at an extremely low rate, out of reach of any current experiment. The observation of a LFV decay would be a striking sign of new physics.

In this chapter we will discuss the origin of flavor and of the suppression of FCNC in the SM. Then, we will introduce the theoretical framework of the effective field theory, used to describes $b \to s\ell\ell'$ transitions and interpret related measurements. Finally, we will provide the definitions of the $b \to s\ell\ell'$ observables discussed in this document, including angular distributions, lepton flavor universality tests and lepton flavor violating searches, as well as the theoretical formalism used in their measurements.

1.1 Origin of flavor in the Standard Model

The origin of flavor in the Standard Model lies in the replication of fermion generations and in the structure of the Yukawa sector. Each type of fermion field — up-type quarks, down-type quarks, charged leptons, and neutrinos — appears in three copies (*flavors*), which are identical under gauge interactions but differ by their Yukawa couplings to the Higgs field.

The Yukawa Lagrangian is given by

$$\mathcal{L}_Y = -\,\bar{Q}_L^0\, Y_d\, H\, d_R^0 -\, \bar{Q}_L^0\, Y_u\, \tilde{H}\, u_R^0 -\, \bar{L}_L^0\, Y_\ell\, H\, \ell_R^0 -\, \bar{L}_L^0\, Y_\nu\, \tilde{H}\, \nu_R^0 + \text{h.c.}, \tag{1.1.1}$$

where Q_L^0 and L_L^0 are the left-handed quark and lepton doublets in the weak-interaction basis, u_R^0, d_R^0, ℓ_R^0, and ν_R^0 are the right-handed singlets, H is the Higgs doublet, $\tilde{H} = i\sigma_2 H^*$ with σ_2 the second Pauli matrix, and Y_f are general complex 3×3 Yukawa matrices in flavor space.

After electroweak symmetry breaking, the Higgs field acquires a vacuum expectation value $\langle H \rangle = v/\sqrt{2}$, generating fermion mass matrices:

$$M_f = \frac{v}{\sqrt{2}}\, Y_f, \qquad f = u, d, \ell, \nu. \tag{1.1.2}$$

These matrices are, in general, non-diagonal in the weak-interaction (flavor) basis, and thus mix different fermion fields. To describe physical fermions with definite masses, we must diagonalize each mass matrix by bi-unitary transformations:

$$U_{f_L}^\dagger\, M_f\, U_{f_R} = \text{diag}(m_{f_1}, m_{f_2}, m_{f_3}), \tag{1.1.3}$$

where U_{f_L} and U_{f_R} are unitary matrices that redefine the left- and right-handed fields as

$$f_L^0 = U_{f_L}\, f_L', \qquad f_R^0 = U_{f_R}\, f_R'. \tag{1.1.4}$$

Because the up- and down-type quarks require independent rotations, the weak charged-current interaction acquires a nontrivial mixing matrix. In the gauge (weak) basis, the left-handed charged-current interaction reads

$$\mathcal{L}_{\text{CC}} = \frac{g}{\sqrt{2}}\, \bar{u}_L^0\, \gamma^\mu\, d_L^0\, W_\mu^+ + \text{h.c.} \tag{1.1.5}$$

where g is the $SU(2)_L$ gauge coupling, γ^μ the Dirac matrices and W_μ^+ the charged weak boson. After rotation to the mass eigenbasis, using $u_L^0 = U_{u_L}\, u_L'$ and $d_L^0 = U_{d_L}\, d_L'$, one obtains

$$\mathcal{L}_{\text{CC}} = \frac{g}{\sqrt{2}}\, \bar{u}_L'\, \gamma^\mu\, (U_{u_L}^\dagger U_{d_L})\, d_L'\, W_\mu^+ + \text{h.c.}, \tag{1.1.6}$$

which defines the Cabibbo–Kobayashi–Maskawa (CKM) matrix:

$$V_{\text{CKM}} = U_{u_L}^\dagger\, U_{d_L} = \begin{pmatrix} V_{ud} & V_{us} & V_{ub} \\ V_{cd} & V_{cs} & V_{cb} \\ V_{td} & V_{ts} & V_{tb} \end{pmatrix}. \tag{1.1.7}$$

Analogously, in the lepton sector, when neutrinos are massive, the mismatch between the diagonalizations of M_ℓ and M_ν gives rise to the Pontecorvo–Maki–Nakagawa–Sakata (PMNS) matrix:

$$U_{\text{PMNS}} = U_{\ell_L}^\dagger\, U_{\nu_L} = \begin{pmatrix} U_{e1} & U_{e2} & U_{e3} \\ U_{\mu 1} & U_{\mu 2} & U_{\mu 3} \\ U_{\tau 1} & U_{\tau 2} & U_{\tau 3} \end{pmatrix}. \tag{1.1.8}$$

Thus, flavor mixing in the Standard Model arises from the misalignment between the fermion mass eigenstates and their weak-interaction eigenstates.

The structure of the neutral-current (NC) interaction is different from the one of charged current (CC). In the gauge (weak) basis, the NC interaction is given by

$$\mathcal{L}_{\mathrm{NC}} = \frac{g}{\cos\vartheta_W}\,\bar{f}_L^0\,\gamma^\mu\,(T_3 - Q\sin^2\vartheta_W)\,f_L^0\,Z_\mu, \tag{1.1.9}$$

where T_3 and Q are the weak isospin and electric charge operators, respectively. After rotating to the mass eigenbasis, using $f_L^0 = U_{f_L}\,f_L'$, one finds

$$\bar{f}_L^0\,\gamma^\mu\,f_L^0 = \bar{f}_L'\,U_{f_L}^\dagger\,\gamma^\mu\,U_{f_L}\,f_L' = \bar{f}_L'\,\gamma^\mu\,f_L', \tag{1.1.10}$$

since U_{f_L} is unitary. Therefore, the neutral-current interaction remains flavor-diagonal:

$$\mathcal{L}_{\mathrm{NC}} = \frac{g}{\cos\vartheta_W}\,\bar{f}_L'\,\gamma^\mu\,(T_3 - Q\sin^2\vartheta_W)\,f_L'\,Z_\mu. \tag{1.1.11}$$

This implies that, at tree level, the Standard Model predicts no flavor-changing neutral currents (FCNCs). Such processes can only occur through higher-order loop corrections, where they are strongly suppressed by the Glashow–Iliopoulos–Maiani (GIM) mechanism. The appearance of non-trivial mixing matrices (CKM or PMNS) in the charged-current sector but not in the neutral-current one is a direct consequence of the independent diagonalization of the fermion mass matrices.

In conclusion, flavor in the SM manifests both in the fermion mass spectrum and in the structure of weak interactions, giving rise to flavor-changing processes, CP violation, and the rich phenomenology of meson decays and neutrino oscillations.

1.2 Flavor Changing Neutral Currents in the Standard Model

Flavor Changing Neutral Currents (FCNCs) denote processes in which the flavor of a quark changes while interacting via a neutral gauge boson (photon, Z boson, or gluon). The previous section showed that, unlike charged current interactions mediated by the $W^\pm$ bosons, neutral gauge bosons in the SM couple diagonally in flavor space and therefore do not induce tree-level flavor changes. As a consequence, FCNC transitions are forbidden at tree level in the SM. They can only arise through higher-order loop diagrams, most notably:

- Penguin diagrams, in which a quark emits and reabsorbs a W boson inside the loop, with a photon, Z, or gluon emitted externally.
- Box diagrams, involving the exchange of two W bosons and virtual quark propagation.

Examples of these diagrams are shown in figure 1.2.1. These loop-induced mechanisms enable rare transitions such as $b \to s\gamma$, $b \to s\ell^+\ell^-$, and $s \to d\nu\bar{\nu}$.

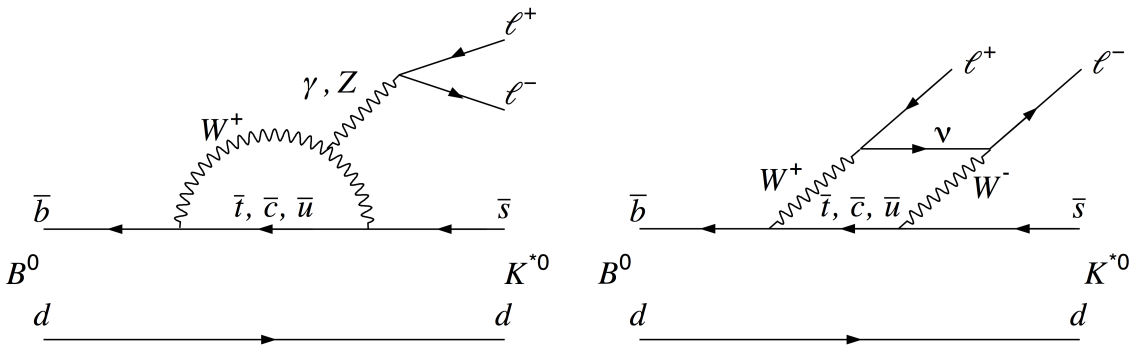

Figure 1.2.1: Feynman diagrams in the SM of the $B^0 \to K^{*0}\ell^+\ell^-$ decay for the (left) electroweak penguin and (right) box diagram.

The suppression of FCNCs is a direct consequence of the GIM mechanism. In this framework, the unitarity of the Cabibbo–Kobayashi–Maskawa (CKM) matrix enforces cancellations among loop contributions from up-type quarks. If all up-type quark masses were equal, the cancellation would be exact, leading to vanishing FCNC amplitudes. In practice, only mass splittings between the up, charm, and top quarks render the amplitudes non-zero. The resulting decay rates are therefore highly suppressed, with branching fractions typically of order 10^{-6} or smaller.

The rarity of FCNC processes makes them a powerful probe for physics beyond the Standard Model. New particles could intervene in the loops as virtual particles. Their presence could lead to a change in the angular distribution of the final-state particles or a sizeable modification of the rate of the decays, potentially in different ways depending on the lepton family. Many extensions of the SM, such as theories with new heavy Z' bosons, leptoquarks, or supersymmetric particles, can either enhance the loop contributions or generate FCNCs already at tree level. Precision measurements of FCNC decays, such as $B \to K^*\ell^-\ell^+$ in the b-sector or $K^+ \to \pi^+\nu\bar{\nu}$ in the s-sector, thus provide stringent tests of the SM and strong constraints on possible new physics scenarios.

1.3 Effective field theory

Effective theories rely on the principle that, under certain hypothesis, specific phenomena can be described in a simplified way, without knowing all the details of the unknown fundamental theory. The physics observables are well approximated by a limit in the wider range of validity of the full theory. The Newtonian mechanics, for example, is an effective theory of the special relativity for objects moving at a speed much lower than the speed of light. An example of effective theory in quantum field theory is the Fermi theory of weak interactions, describing the muon decay which occurs at a scale, the mass of the muon, much smaller than the W mass, so that the W propagator can be interpreted as a contact interaction mediated by the Fermi constant $G_F = g^2/(4\sqrt{2}m_W^2)$. The Fermi constant is the condition matching the effective theory to the full theory.

The main ingredients of an effective field theory (EFT) are the degrees of freedom for the physics we want to describe, the parameter in which we perform the expansion (called power counting), and the symmetries of the process. The general form of an EFT Lagrangian is:

$$\mathcal{L}_{\text{EFT}} = \mathcal{L}_{d\leq 4} + \sum_{n>4} \frac{C_n(\mu_s)}{\Lambda^{n-4}} O_n \tag{1.3.1}$$

Here μ_s is the renormalization scale, that should be larger than the relevant energy scale of the process. $\mathcal{L}_{d\leq 4}$ contains the renormalizable operators. The $\mathcal{O}_n$ are local operators of dimension $d_n > 4$, consistent with the symmetries and encoding the low-energy, long-distance contributions from the quarks. $C_n(\mu_s)$ are the Wilson coefficients, defined at the renormalization scale μ_s, representing the strength of the couplings and incapsulating the high-energy, short-distance contributions. Factors of $1/\Lambda$, where Λ is the energy scale, ensure that each term has total mass dimension 4.

The power counting and truncation process foresee that, if one aims for an accuracy at the order $(E/\Lambda)^n$, with E a typical process energy, one should keep all operators with dimension up to $d_{\max}$ such that $(E/\Lambda)^{d_{\max}-4}$ is at the desired accuracy. Then the relevant symmetries (gauge, Lorentz, discrete) restrict the set of $\mathcal{O}_n$.

The advantage of this formalism is that new physics contributes to the Wilson coefficients, which can be computed at the heavy scale Λ, $C_n(\mu_s = \Lambda)$ in the full theory and evolved down to the EFT scale using the renormalization group equations, and viceversa. Therefore, low-energy observables calculated in the EFT, truncating consistently at the chosen order, can be compared to experimental measurements and inform on the full theory, identifying the region of coefficient space where beyond the standard model (BSM) physics should reside. Uncertainties from neglected term should be calculated and associated to the prediction.

In the case of $b\to s\ell\ell$ transitions, the relevant energy scale of the decay is around 5 GeV/c^2, corresponding to the B mass. Heavy degrees of freedom, such as the top quark, the weak interaction bosons, the Higgs and any potential heavy new particle can be integrated out and would manifest only in the Wilson coefficients. The Lagrangian $\mathcal{L}_{\text{EFT}}$ of an EFT explaining BSM phenomena would assume the general form:

$$\mathcal{L}_{\text{EFT}} = \mathcal{L}_{\text{SM}} + \frac{1}{\Lambda} C^{(5)} O^{(5)} + \frac{1}{\Lambda^2} \sum_n C_n^{(6)} O_n^{(6)} + \mathcal{O}\left(\frac{1}{\Lambda^3}\right) \tag{1.3.2}$$

The renormalizable SM Lagrangian $\mathcal{L}_{\text{SM}}$ contains operators up to dimension four. The effective Lagrangian beyond the SM can be organized as an expansion in higher-dimensional operators, here presented up to dimension six. There is a single independent dimension-five operator $O^{(5)}$, the Weinberg operator, responsible for Majorana neutrino masses. At dimension six, several operators $O_n^{(6)}$ arise at leading order in the EFT expansion upon integrating out heavy degrees of freedom; higher-dimension terms (e.g. dimension seven) are suppressed by additional powers of $1/\Lambda$ and are typically negligible compared to dimension-six operators.

The dimension-six operators relevant for $b \to s$ transitions are listed in the following. The prime ($\prime$) is used to denote chirality-flipped operators, which in the SM are suppressed

(parametrically by ratios of light to heavy quark masses, e.g. m_s/m_b). Subscripts L, R denote left- and right-handed chirality projectors $P_{L,R} = (1 \mp \gamma^5)/2$, and ℓ_1, ℓ_2 label the two leptons in $b \to s\ell_1\ell_2$ decays.

- **Electromagnetic dipole operator** O_7:

$$O_7^{(\prime)} \propto m_b \, (\bar{s}_{L(R)} \, \sigma^{\mu\nu} \, b_{R(L)}) \, F_{\mu\nu}, \tag{1.3.3}$$

  where $\sigma^{\mu\nu} = \dfrac{i}{2}[\gamma^\mu, \gamma^\nu]$ and $F_{\mu\nu}$ is the electromagnetic field tensor.

- **Chromomagnetic dipole operator** O_8:

$$O_8^{(\prime)} \propto m_b \, (\bar{s}_{L(R)} \, \sigma^{\mu\nu} T^a \, b_{R(L)}) \, G^a_{\mu\nu}, \tag{1.3.4}$$

  with T^a the $SU(3)$ generators and $G^a_{\mu\nu}$ the gluon field-strength tensor.

- **Semileptonic operators** $O_9^{\ell_1\ell_2}$ and $O_{10}^{\ell_1\ell_2}$:

$$O_9^{(\prime)\,\ell_1\ell_2} \propto (\bar{s}_{L(R)}\gamma^\mu b_{L(R)}) \, (\bar{\ell}_1\gamma_\mu\ell_2), \tag{1.3.5}$$

$$O_{10}^{(\prime)\,\ell_1\ell_2} \propto (\bar{s}_{L(R)}\gamma^\mu b_{L(R)}) \, (\bar{\ell}_1\gamma_\mu\gamma_5\ell_2). \tag{1.3.6}$$

  Both O_9 and O_{10} receive loop-level contributions from photon and Z penguins and from box diagrams; the photon penguin is especially important for C_9 at low dilepton invariant mass.

- **Scalar, pseudoscalar and tensor operators**:

$$O_S^{(\prime)\,\ell_1\ell_2} \propto (\bar{s}_{L(R)} b_{R(L)}) \, (\bar{\ell}_1\ell_2), \tag{1.3.7}$$

$$O_P^{(\prime)\,\ell_1\ell_2} \propto (\bar{s}_{L(R)} b_{R(L)}) \, (\bar{\ell}_1\gamma_5\ell_2), \tag{1.3.8}$$

$$O_T^{\ell_1\ell_2} \propto (\bar{s} \, \sigma^{\mu\nu} b) \, (\bar{\ell}_1\sigma_{\mu\nu}\ell_2), \tag{1.3.9}$$

$$O_{T5}^{\ell_1\ell_2} \propto (\bar{s} \, \sigma^{\mu\nu} b) \, (\bar{\ell}_1\sigma_{\mu\nu}\gamma_5\ell_2). \tag{1.3.10}$$

  Tensor operators (O_T, O_{T5}) do not arise from tree-level matching of W or Z exchange in the SM and are zero (or highly suppressed) at that order; similarly, in simple SM matching one finds relations among some Wilson coefficients (e.g. $C_S \approx -C_P$, $C'_S \approx C'_P$ in certain normalizations).

In the Standard Model the dominant operators for $b \to s\ell\ell$ are O_7, O_9 and O_{10} (with small primed counterparts). From the effective Lagrangian one derives the interaction Hamiltonian, which in turn defines the Feynman rules used to compute the decay amplitudes. In the case of meson decays, the quark-level operators are embedded into hadrons, and their matrix elements are parametrized by hadronic form factors. Squaring the amplitudes, averaging over spins, and integrating over the Lorentz-invariant phase space yields the partial decay width. Finally, the branching fraction is obtained dividing by the total width. Measurements of the observables discussed in this document constraint the Wilson coefficient associated to the operators relevant for the decay, including those parameterizing potential new physics contributions.

1.4 Angular observables of $B^0 \to K^{*0}\mu^+\mu^-$ decays

The final state of the decay $B^0 \to K^{*0}\mu^+\mu^-$, with $K^{*0} \to K^+\pi^-$, can be described by four variables: the invariant mass squared of the dimuon system (q^2), and three decay angles $\vec{\Omega} = (\cos\vartheta_\ell, \cos\vartheta_K, \phi)$. Here, ϑ_ℓ is the angle between the μ^+ (μ^-) and the direction opposite to that of the B^0 ($\bar{B}^0$) in the rest frame of the dimuon system. The angle between the direction of the K^+ (K^-) and the B^0 ($\bar{B}^0$) in the rest frame of the K^{*0} ($\bar{K}^{*0}$) system is denoted ϑ_K. Finally, ϕ is the angle between the plane defined by the dimuon pair and the plane defined by the kaon and pion in the B^0 ($\bar{B}^0$) rest frame. These angles are represented in figure 1.4.1.

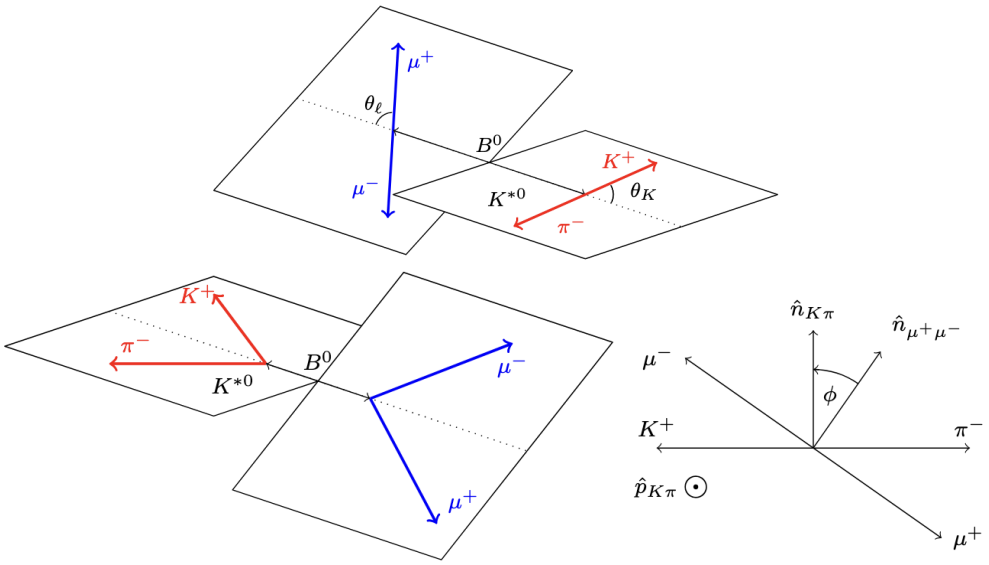

Figure 1.4.1: Definition of the ϑ_K, ϑ_L and ϕ angles in $B^0 \to K^{*0}\ell^+\ell^-$ decays.

The differential decay rates of $B^0 \to K^{*0}\mu^+\mu^-$ and $\bar{B}^0 \to \bar{K}^{*0}\mu^+\mu^-$ decays, in terms of these variables, are:

$$\frac{d^4\Gamma[\bar{B}^0 \to \bar{K}^{*0}\mu^+\mu^-]}{dq^2\, d\vec{\Omega}} = \frac{9}{32\pi}\sum_i I_i(q^2) f_i(\vec{\Omega}), \tag{1.4.1}$$

$$\frac{d^4\bar{\Gamma}[B^0 \to K^{*0}\mu^+\mu^-]}{dq^2\, d\vec{\Omega}} = \frac{9}{32\pi}\sum_i \bar{I}_i(q^2) f_i(\vec{\Omega}), \tag{1.4.2}$$

where Γ ($\bar{\Gamma}$) refers to decays involving a b ($\bar{b}$) quark and hence a $\bar{B}^0$ (B^0) meson, the terms $f_i(\vec{\Omega})$ are combinations of spherical harmonics, and the I_i ($\bar{I}_i$) are q^2-dependent angular observables.

The I_i terms can be expressed as bilinear combinations of six complex decay amplitudes $A^{L,R}_{0,\parallel,\perp}$, which correspond to the different transversity states of the K^{*0} meson ($0, \parallel, \perp$) and the different chiralities (left- and right-handed) of the dimuon system. An additional suffix s or c is conventionally added to some of the I_i terms to indicate that they are associated to a

$\sin^2\vartheta_K$ or $\cos^2\vartheta_K$ dependence. When q^2 is sufficiently large ($q^2 \gtrsim 1$ GeV$^2/c^4$), the muons can be considered massless. The list of the angular terms and observables that remain in this massless limit is given in Table 1.4.1.

Following the notation of Ref. [6], q^2-dependent CP-averaged observables, S_i, and CP asymmetries, A_i, can be defined:

$$S_i = \frac{I_i + \bar{I}_i}{\frac{d\Gamma}{dq^2} + \frac{d\bar{\Gamma}}{dq^2}}, \tag{1.4.3}$$

$$A_i = \frac{I_i - \bar{I}_i}{\frac{d\Gamma}{dq^2} + \frac{d\bar{\Gamma}}{dq^2}}. \tag{1.4.4}$$

CP-averaged angular distribution in the massless limit

In the massless limit, the following relations holds: $S_{1s} = 3S_{2s}$, $S_{1c} = -S_{2c}$, and $\frac{3}{4}(2S_{1s} + S_{1c}) - \frac{1}{4}(2S_{2s} + S_{2c}) = 1$ (see, for example, Ref. [6]). These reduce the number of independent CP-averaged observables from eleven to eight. The relations between the observables also hold to a good approximation for $q^2 < 1$ GeV$^2/c^4$ and are therefore often adopted for the full q^2 range.

The S_{1c} observable corresponds to the fraction of longitudinal polarisation of the K^{*0} meson and is more commonly referred to as F_L:

$$F_L = S_{1c} = \frac{|A_0^L|^2 + |A_0^R|^2}{|A_0^L|^2 + |A_0^R|^2 + |A_\parallel^L|^2 + |A_\parallel^R|^2 + |A_\perp^L|^2 + |A_\perp^R|^2}. \tag{1.4.5}$$

It is also conventional to replace S_{6s} by the forward-backward asymmetry of the dimuon system, $A_{\rm FB}$: $A_{\rm FB} = \frac{3}{4}S_{6s}$. The CP-averaged angular distribution of the $B^0 \to K^{*0}\mu^+\mu^-$ decay can then be written as:

$$\begin{aligned}\frac{1}{d(\Gamma+\bar{\Gamma})/dq^2}\frac{d^4(\Gamma+\bar{\Gamma})}{dq^2\, d\vec{\Omega}} = \frac{9}{32\pi}\Big[&\frac{3}{4}(1-F_L)\sin^2\vartheta_K + F_L\cos^2\vartheta_K \\ &+ \frac{1}{4}(1-F_L)\sin^2\vartheta_K\cos 2\vartheta_\ell \\ &- F_L\cos^2\vartheta_K\cos 2\vartheta_\ell + S_3\sin^2\vartheta_K\sin^2\vartheta_\ell\cos 2\phi \\ &+ S_4\sin 2\vartheta_K\sin 2\vartheta_\ell\cos\phi + S_5\sin 2\vartheta_K\sin\vartheta_\ell\cos\phi \\ &+ \frac{4}{3}A_{\rm FB}\sin^2\vartheta_K\cos\vartheta_\ell + S_7\sin 2\vartheta_K\sin\vartheta_\ell\sin\phi \\ &+ S_8\sin 2\vartheta_K\sin 2\vartheta_\ell\sin\phi + S_9\sin^2\vartheta_K\sin^2\vartheta_\ell\sin 2\phi\Big].\end{aligned} \tag{1.4.6}$$

Reducing form factor uncertainties: the P' observables

The set of observables defined above might be affected by the uncertainties on the $B \to K^{*0}$ form-factors uncertainties, which parametrize the hadronic matrix elements of quark currents

i	I_i	f_i
1s	$\frac{3}{4}\left(\lvert A_\parallel^L\rvert^2+\lvert A_\perp^L\rvert^2+\lvert A_\parallel^R\rvert^2+\lvert A_\perp^R\rvert^2\right)$	$\sin^2\vartheta_K$
1c	$\left(\lvert A_0^L\rvert^2+\lvert A_0^R\rvert^2\right)$	$\cos^2\vartheta_K$
2s	$\frac{1}{4}\left(\lvert A_\parallel^L\rvert^2+\lvert A_\perp^L\rvert^2+\lvert A_\parallel^R\rvert^2+\lvert A_\perp^R\rvert^2\right)$	$\sin^2\vartheta_K\cos 2\vartheta_\ell$
2c	$-\left(\lvert A_0^L\rvert^2-\lvert A_0^R\rvert^2\right)$	$\cos^2\vartheta_K\cos 2\vartheta_\ell$
3	$\frac{1}{2}\left(\lvert A_\perp^L\rvert^2-\lvert A_\parallel^L\rvert^2+\lvert A_\perp^R\rvert^2-\lvert A_\parallel^R\rvert^2\right)$	$\sin^2\vartheta_K\sin^2\vartheta_\ell\cos 2\phi$
4	$\sqrt{2}\,\mathrm{Re}(A_0^L A_\parallel^{L*}+A_0^R A_\parallel^{R*})$	$\sin 2\vartheta_K\sin 2\vartheta_\ell\cos\phi$
5	$\sqrt{2}\,\mathrm{Re}(A_0^L A_\perp^{L*}-A_0^R A_\perp^{R*})$	$\sin 2\vartheta_K\sin\vartheta_\ell\cos\phi$
6s	$2\,\mathrm{Re}(A_\parallel^L A_\perp^{L*}-A_\parallel^R A_\perp^{R*})$	$\sin^2\vartheta_K\cos\vartheta_\ell$
7	$\sqrt{2}\,\mathrm{Im}(A_0^L A_\parallel^{L*}-A_0^R A_\parallel^{R*})$	$\sin 2\vartheta_K\sin\vartheta_\ell\sin\phi$
8	$\sqrt{2}\,\mathrm{Im}(A_0^L A_\perp^{L*}+A_0^R A_\perp^{R*})$	$\sin 2\vartheta_K\sin 2\vartheta_\ell\sin\phi$
9	$\mathrm{Im}(A_\parallel^{L*} A_\perp^L+A_\parallel^{R*} A_\perp^R)$	$\sin^2\vartheta_K\sin^2\vartheta_\ell\sin 2\phi$
10	$\frac{1}{3}\left(\lvert A_S^L\rvert^2+\lvert A_S^R\rvert^2\right)$	1
11	$\sqrt{\frac{4}{3}}\,\mathrm{Re}(A_S^L A_0^{L*}+A_S^R A_0^{R*})$	$\cos\vartheta_K$
12	$-\frac{1}{3}\left(\lvert A_S^L\rvert^2+\lvert A_S^R\rvert^2\right)$	$\cos 2\vartheta_\ell$
13	$-\sqrt{\frac{4}{3}}\,\mathrm{Re}(A_S^L A_0^{L*}+A_S^R A_0^{R*})$	$\cos\vartheta_K\cos 2\vartheta_\ell$
14	$\sqrt{\frac{2}{3}}\,\mathrm{Re}(A_S^L A_\parallel^{L*}+A_S^R A_\parallel^{R*})$	$\sin\vartheta_K\sin 2\vartheta_\ell\cos\phi$
15	$\sqrt{\frac{8}{3}}\,\mathrm{Re}(A_S^L A_\perp^{L*}-A_S^R A_\perp^{R*})$	$\sin\vartheta_K\sin\vartheta_\ell\cos\phi$
16	$\sqrt{\frac{8}{3}}\,\mathrm{Im}(A_S^L A_\parallel^{L*}-A_S^R A_\parallel^{R*})$	$\sin\vartheta_K\sin\vartheta_\ell\sin\phi$
17	$\sqrt{\frac{2}{3}}\,\mathrm{Im}(A_S^L A_\perp^{L*}+A_S^R A_\perp^{R*})$	$\sin\vartheta_K\sin 2\vartheta_\ell\sin\phi$

Table 1.4.1: Angular observables I_i and their corresponding angular terms for dimuon masses much larger than twice the muon mass. The terms in the lower part of the table arise from the $K^+\pi^-$ S-wave contribution to the $K^+\pi^-\mu^+\mu^-$ final state. The $\bar{I}_i$ coefficients are obtained by the substitution $A\to\bar{A}$, i.e. by complex conjugation of the weak phases in the amplitudes.

between meson states. They are intrinsically non-perturbative quantities that cannot be computed directly in perturbative quantum chromo dynamics (QCD). Several complementary approaches are employed to determine them across different kinematic regimes. At low q^2 (large recoil), Light-Cone Sum Rules (LCSR) allow the calculation of hadronic matrix elements by combining an operator product expansion near the light cone with the light-cone distribution amplitudes of the K^* meson [7, 8]. At high q^2 (low recoil), Lattice QCD calculations offer first-principles determinations using numerical simulations of QCD on a discretized spacetime lattice [9, 10]. In the heavy-quark limit, QCD Factorization (QCDF) and Soft-Collinear Effective Theory (SCET) yield symmetry relations among the form factors, reducing them to two universal "soft" functions, $\xi_\perp$ and $\xi_\parallel$, up to perturbative and power

corrections [11–13]. Phenomenological approaches such as the light-front quark model or the covariant confined quark model [14, 15] are sometimes used to interpolate between these regimes. Modern global analyses typically combine LCSR and lattice inputs using analyticity-based parameterizations such as the z-expansion (BCL or BGL) [16, 17], providing consistent determinations of the form factors over the full kinematic range relevant for $B \to K^* \ell^+ \ell^-$ decays.

Additional sets of observables, for which the leading $B^0 \to K^{*0}$ form-factor uncertainties cancel, can be built from F_L and S_3–S_9. Examples of such optimised observables include the transverse asymmetry $A_T^{(2)}$ [18], where $A_T^{(2)} = \frac{2S_3}{1-F_L}$, and the P_i' series of observables [19]:

$$\begin{aligned} P_1 &= \frac{2S_3}{(1-F_L)} = A_T^{(2)}, \\ P_2 &= \frac{2}{3}\frac{A_{\rm FB}}{(1-F_L)}, \\ P_3 &= -\frac{S_9}{(1-F_L)}, \end{aligned} \tag{1.4.7}$$

$$\begin{aligned} P'_{4,5,8} &= \frac{S_{4,5,8}}{\sqrt{F_L(1-F_L)}}, \\ P'_6 &= \frac{S_7}{\sqrt{F_L(1-F_L)}}. \end{aligned} \tag{1.4.8}$$

It should be noted, though, that these observables might still be affected by next to leading order uncertainties on the form factors.

The S-wave component

In addition to the resonant K^{*0} contribution, which is a $K^+\pi^-$ system in a P-wave, the $B^0 \to K^{*0}\mu^+\mu^-$ decays selected by the experiments to perform the measurement can contain an irreducible contamination from the $K^+\pi^-$ system in an S-wave configuration. The addition of an S-wave component introduces two new complex decay amplitudes: A_S^L and A_S^R. The angular terms in the lower part of Table 1.4.1 arise from the interference between S- and P-wave components. The presence of a $K^+\pi^-$ system in an S-wave configuration modifies the angular distribution to:

$$\begin{aligned} \frac{1}{d(\Gamma+\bar{\Gamma})/dq^2}\frac{d^4(\Gamma+\bar{\Gamma})}{dq^2\, d\vec{\Omega}}\bigg|_{S+P} &= (1-F_S)\,\frac{1}{d(\Gamma+\bar{\Gamma})/dq^2}\frac{d^4(\Gamma+\bar{\Gamma})}{dq^2\, d\vec{\Omega}}\bigg|_{P} \\ &+ \frac{3}{16\pi}F_S \sin^2\vartheta_\ell \\ &+ \frac{9}{32\pi}(S_{11} + S_{13}\cos 2\vartheta_\ell)\cos\vartheta_K \qquad (1.4.9) \\ &+ \frac{9}{32\pi}(S_{14}\sin 2\vartheta_\ell + S_{15}\sin\vartheta_\ell)\sin\vartheta_K\cos\phi \\ &+ \frac{9}{32\pi}(S_{16}\sin\vartheta_\ell + S_{17}\sin 2\vartheta_\ell)\sin\vartheta_K\sin\phi, \qquad (1.4.10) \end{aligned}$$

where F_S denotes the S-wave fraction,

$$F_S = \frac{|A_S^L|^2 + |A_S^R|^2}{|A_S^L|^2 + |A_S^R|^2 + |A_0^L|^2 + |A_0^R|^2 + |A_\parallel^L|^2 + |A_\parallel^R|^2 + |A_\perp^L|^2 + |A_\perp^R|^2}, \tag{1.4.11}$$

and the terms S_{11}, S_{13}–S_{17} arise from interference between the S- and P-wave amplitudes. Note that F_S replaces the terms S_{10} and S_{12}, with $F_S = 3S_{10} = -3S_{12}$.

In early LHCb angular analysis, the S-wave contribution was considered as a systematic uncertainty, since the S-wave contribution was expected to be approximately 5%. In the analysis described in this document, F_S and the interference terms between the S- and P-wave were treated as nuisance parameters.

1.5 Lepton flavor universality tests

In the Standard Model, the couplings of the electroweak gauge bosons to the leptons are independent of lepton flavor. This is because lepton flavor enters only through the Yukawa interactions, shown in eq. 1.1.1, with different couplings for each lepton flavor (e, μ, τ). The gauge interactions, mediated by the photon, Z, and W bosons, remain diagonal and universal in flavor space, as gauge symmetry forbids flavor-dependent couplings: all lepton generations transform identically under the gauge group $SU(2)_L \times U(1)_Y$.

This feature of the Standard Model is well verified experimentally at the percent and per mille levels in W and Z bosons decays [20]. However, there is a priori no reason to believe that physics beyond the standard model should also express lepton universality. Lepton flavor universality tests are therefore powerful probes for new physics. In FCNC $b \to s\ell\ell$ and $b \to d\ell\ell$ transitions, they are defined as [21]:

$$R_H = \frac{\displaystyle\int \frac{d\Gamma(H_b \to H\ell_2^+\ell_2^-)}{dq^2}\, dq^2}{\displaystyle\int \frac{d\Gamma(H_b \to H\ell_1^+\ell_1^-)}{dq^2}\, dq^2},$$

where H_b represents a hadron containing a b quark, H represents a hadron containing at least one s (such as a K, a K^* or a ϕ meson) or one d quark (such a π or ρ meson), and leptons of two different families are generically represented as ℓ_1 and ℓ_2. The decay rate, Γ, is integrated over a range of the squared dilepton invariant mass, q^2.

The R_H ratios are convenient because hadronic uncertainties in the theoretical predictions cancel between numerator and denominator, in particular the form-factors uncertainties. The R_H ratios are expected to be close to unity in the SM [21–23], a part from effect due to phase space, like differences in the lepton masses. The remaining theoretical uncertainties are due to radiative corrections, which are precisely estimated below the percent level and have more impact at low q^2.

Some of the leading-order Feynman diagrams for the $B^0 \to K^{*0}\ell^+\ell^-$ decays in possible NP scenarios, are shown in figure 1.5.1. In these scenarios, the $b \to s\ell\ell$ transition is operated by a new gauge boson Z' (on the left) or by a leptoquark (on the right). If these new particles

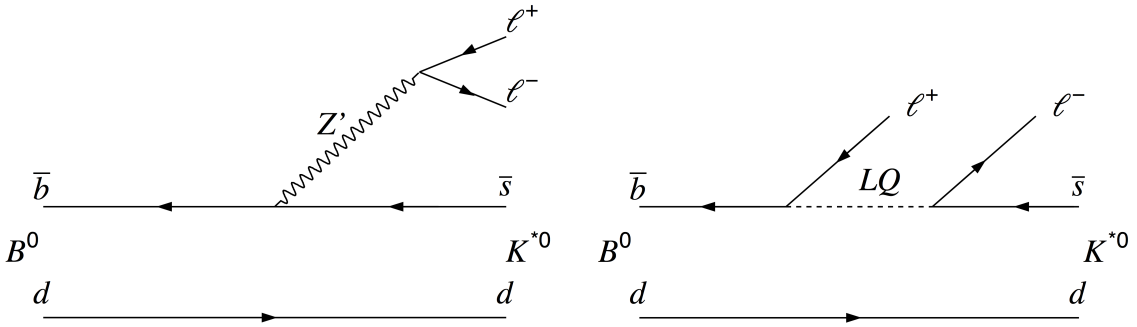

Figure 1.5.1: Feynman diagrams for possible NP contributions in $B^0 \to K^{*0}\ell^+\ell^-$ decay: (left) a tree-level diagram mediated by a new gauge boson Z' and (right) a tree-level diagram involving a leptoquark LQ.

have different couplings depending on the flavor of the lepton pair, this would result in lepton flavor universality violation.

It is worth to note that lepton flavor universality tests can be performed in other system, for example in flavor changing charged currents $b \to c\ell\nu_\ell$ transitions:

$$R_D = \frac{\displaystyle\int \frac{d\Gamma(H_b \to H_c \ell_1^- \bar{\nu}_{\ell_1})}{dq^2}\, dq^2}{\displaystyle\int \frac{d\Gamma(H_b \to H_c \ell_2^- \bar{\nu}_{\ell_2})}{dq^2}\, dq^2},$$

where H_c represents a hadron containing a c quark, like D mesons. These transitions are not suppressed as the FCNC and actually occur at tree level at leading order. However, also these decays could manifest a violation of the lepton flavor universality in some new physics models, for example with charged Higgs or leptoquarks.

1.6 Lepton flavor violating B decays

In the Standard Model, each lepton family has a different lepton number which is conserved in electroweak transitions: lepton-flavor-violation is not foreseen with mass-less neutrinos. However, the observation of neutrino oscillations provided the first evidence of a lepton-flavor-violating process, implying in turn that neutrinos have a non-zero mass. This fact can be integrated within the SM, introducing neutrino mixing through the PMNS matrix. The mechanism is analogous to the quark mixing described by the CKM matrix, with flavors eigenstates different from the mass eigenstates, but differs for the fact that what are accessible experimentally are the flavor eigenstates and not the mass eigenstates, and that the quark transitions are mediated by gauge bosons. Moreover, the hierarchical structures of the CKM and PMNS matrices are very different, as shown in figure1.6.1: quark flavour mixing is parametrised by a nearly diagonal CKM matrix, with a small mixing between heavy and light quarks, while the PMNS matrix features a more democratic hierarchy, with mostly large

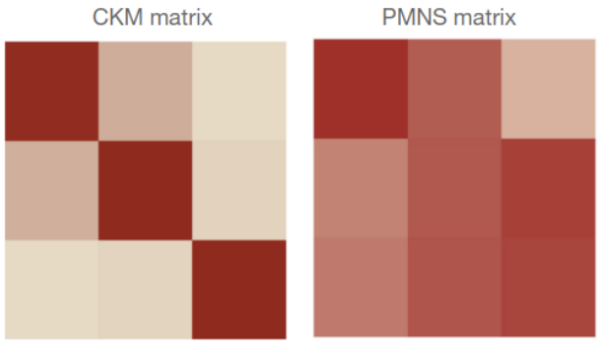

Figure 1.6.1: Graphical representation of CKM and PMNS matrices: darker color indicates an higher magnitude of the corresponding matrix element.

angles except for ϑ_{13}. At these already puzziling differencesit should be added the fact that there is evidence that all fermions directly mix, with couplings given by the CKM and PMNS unitary matrices, except the charged leptons, for which the mass eigenbasis seems to coincide with the weak interaction eigenbasis.

Charged lepton-flavor-violating (cLFV) processes could actually indirectly occur via diagrams with loops where a neutrino oscillates. However such processes will be suppressed by a factor $(\frac{\Delta m_{ij}}{M_W})^4$, where Δm_{ij} is the mass difference of the two neutrinos of different families i, j and M_W is the W boson mass. This ratio is extremely small and, adding up to additional CKM suppression factors, leads to a negligible rate, well below the experimental sensitivities. For instance, all diagrams involving cLFV in the second and third generations are suppressed by a factor $(\frac{\Delta m_{23}}{M_W})^4 \sim 10^{-49}$, on top of any other relevant term. For a charged lepton-flavor violating process to be observable, new particles should dramatically enhance its rate. New vector bosons and leptoquarks are again amon the most common models beyond the SM that could cause a large enhancement of these decays in some scenarios. Therefore, observing a charged lepton-flavor violating process would be a striking and unambigous sign of a physics beyond the standard model.

The hints of deviation from unity of the lepton flavor universality tests in the past years have increased expectations to observe charged lepton flavor violating decays. A natural scenario in presence of a new lepton non universal interaction is to have a CKM-like unitarity matrix responsible for rotating the charged leptons from their mass eigenbasis to the interaction one [24]. This would generally provide a mechanism for charged lepton mixing, assuming that non diagonal terms would be different from zero. However, a lepton universal physics allowing for lepton flavor violating processes is also not excluded. Therefore, despite the fact that recently LFU tensions have strongly reduced, the motivation to look for LFV processes still holds: there is no strong theoretical reason why new physics should have the same flavor structure as the standard model and, in addition, it is a fundamental question understanding why charged leptons are the only fermions not directly mixing, to our current knowledge.

Chapter 2

Collecting data and selecting signal

The physics measurements described in this document relies on the collection of data with the LHCb detector and on successive steps aiming at reducing as much as possible the amount of background. Some common tools and strategies can be identified, despite the specificity of each analysis. This chapter does not provide an exhaustive description of the selections and of the analysis procedures. The published articles are a better reference for this purpose. Instead, the objective is to provide an overview of the procedures leading to the sample of candidates on which the final measurements will be performed.

2.1 Overview of the selection procedure

The selection of data samples containing b-hadron decays in LHCb follows a number of successive steps, aimed at reducing at maximum the contribution from possible backgrounds sources. Two wide categories of backgrounds can be identified. The combinatorial background, coming from random combination of particles produced in the collisions, and physics backgrounds, either fully or partially reconstructed, which are physics processes similar to the decay which is searched for. Physics backgrounds are the most difficult to reject.

The selection starts already during data taking at the detector level, in particular with the hardware trigger selections, based on calorimeter and muon detector information. The online selection continues with the software trigger stage, which reconstructs the events and looks for displaced vertices compatible with a b-hadron decay.

The candidates selected by the trigger undergo additional centralised preselections, called "stripping", which are shared by decays of similar topology. Data filtered by the stripping selection are organized in different streams to facilitate the offline treatment. These preselections consist of loose kinematic, topological and particle identification requirements.

After the stripping, data are ready to be analysed offline. At this point, the selection is refined and optimised to reject the remaining backgrounds. Tighter kinematic, topological and particle identification criteria, usually combined in a multivariate approach, are particularly effective for rejecting the combinatorial background. Physics background are rejected investigating differences in topology, kinematics and particles isolation with respect to the signal, using dedicated vetoes in case of different intermediate states and applying

tight particle identification criteria in case of mis-identified particles.

All analyses presented here make use of a blinding approach to avoid selection choices that could bias the analysis in favour of specific results. Concretely, one common approach is that a region of data around the B mass, called signal region and containing almost the totality of signal events, is not analyzed until the selection and analysis procedures are finalized. This is for example the approach in lepton-flavor-violating searches. The definition of the signal region implies the definition of an upper sideband (on his right) and a lower sideband (on his left) which are instead dominated by backgrounds. In particular, the upper sideband is dominated by combinatorial background while the lower sideband is enriched in physics backgrounds. In the angular analysis, the blinding consists of masking the numerical result of the fit for the observables that should be measured by adding a random, unknown value.

Another common aspect is the use of normalization channels. Because of the uncertainty on the integrated luminosity and on the b production cross section, branching fraction measurements in LHCb are not absolute, but always relative to another abundant decays with precisely measured branching fraction, so that these uncertainties cancel out. If the normalization channel is similar to the decays channel, further uncertainties related to the reconstruction are cancelled or reduced. Normalization channels are often used also as control modes, because they provide a data sample that can be used to check the simulation performances.

2.2 The LHCb detector

The LHCb detector [25, 26] is a single-arm forward spectrometer covering the pseudorapidity $2 < \eta < 5$, designed for the study of particles containing b or c quarks. The detector, schematically represented in figure 2.2.1, includes a high-precision charged-particle reconstruction (tracking) system consisting of a silicon-strip vertex detector surrounding the pp interaction region [27], a large-area silicon-strip detector located upstream of a dipole magnet with a bending power of about $4\,\mathrm{T\,m}$, and three stations of silicon-strip detectors and straw drift tubes [28, 29] placed downstream of the magnet. The tracking system provides a measurement of the momentum, p, of charged particles with a relative uncertainty that varies from 0.5% at low momentum to 1.0% at $200\,\mathrm{GeV}/c$. The minimum distance of a track to a primary vertex (PV), the impact parameter (IP), is measured with a resolution of $(15 + 29/p_\mathrm{T})\,\mu\mathrm{m}$, where p_T is the component of the momentum transverse to the beam, in GeV/c. Different types of charged hadrons are distinguished from one another using information from two ring-imaging Cherenkov (RICH) detectors [30]. Photons, electrons and hadrons are identified by a calorimeter system consisting of scintillating-pad and preshower detectors, an electromagnetic (ECAL) and a hadronic calorimeter. Muons are identified by a system composed of alternating layers of iron and multiwire proportional chambers [31].

The online event selection is performed by a trigger [32, 33], consisting of a hardware stage, based on information from the calorimeter and muon systems, followed by a software stage, which performs full event reconstruction. In the hardware stage, selected events are required to have at least one high-p_T electron, muon or hadron. The software trigger is organised in two stages. The first requires a two-track secondary vertex with a significant displacement

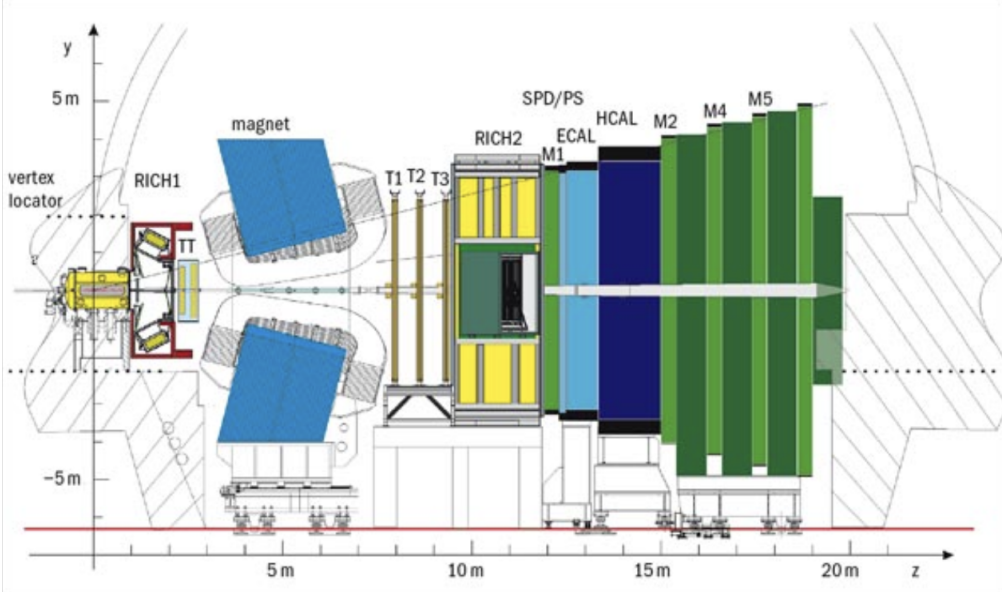

Figure 2.2.1: The basic layout of the LHCb detector up to 2018. The interaction point is to the left, within the vertex locator, and the LHC beam pipe passes through the center of the detector.

from any PV, and at least one charged particle with a minimum requirement on the transverse momentum that is also inconsistent with originating from a PV. The second stage is based on a multivariate algorithm [34, 35] exploiting kinematic, geometric, and lepton-identification criteria to select events containing secondary vertices consistent with the decay of a b hadron.

Simulation is used for various purposes, depending on the analysis: optimise the selections, determine signal and background models for the fits, evaluate residual background contributions, and obtain the selection efficiencies. In the simulation, pp collisions are generated using Pythia 8 [36] with a specific LHCb configuration [37]. The decays of unstable particles are described by EvtGen [38], in which final-state radiation is generated using Photos [39]. For analyses involving tau leptons, the τ decay is simulated using a dedicated model tuned with BaBar data [40] from the Tauola decay library. Finally, the interaction of the generated particles with the detector, and its response, are implemented using the Geant4 toolkit [41] as described in Ref. [42].

The detector is taking data since 2011. Data from 2011 and 2012 were collected in pp collisions at a centre-of mass energy of 7 and 8 TeV, respectively. In this phase, called "run 1", LHCb has collected a data sample corresponding to an integrated luminosity of 3 fb^{-1}. After an LHC shutdown, data collection restarted in 2015 until 2018 at an increased collision energy of 13 TeV. During this period, called "run 2", LHCb collected 6 fb^{-1}. The analyses presented in this document make use of these data samples.

2.3 Lepton reconstruction in LHCb

The study of $b \to s\ell\ell$ decays necessitates the reconstruction of charged leptons. The LHCb detector is not equally suited for the three type of leptons.

The detector has a very high efficiency for muon reconstruction. Muons provide a very clear signature, with a track traversing the whole spectrometer and being identified by hits in the muon chambers, located at the end of the detector.

Electrons might emit photons while travelling through the detector. In case this occurs upstream of the magnet, the electron momentum is underestimated and the photons and electron energies are deposited in different calorimeter cells. A dedicated procedure searches for energy deposits with transverse energy $E_T > 75$ MeV, not associated with charged tracks, within a region of the electromagnetic calorimeter defined by the extrapolation of the electron track upstream of the magnet. Such "bremsstrahlung clusters" are added to the measured electron momentum, improving its determination. The procedure is limited by the energy threshold of the clusters, the acceptance and resolution of the calorimeter, and by the presence of energy deposits wrongly interpreted as bremsstrahlung clusters. There is an impact on the B mass resolution of a decay with electrons in the final state depending on whether bremsstrahlung has been included in the momentum calculation of the electrons or not. Therefore, the invariant mass distribution of the signal needs to be modelled differently to account for this. If energy has been recovered, the distribution shows a smaller tail on the left of the nominal B mass. As drawback, the tail of the distribution on the right might be slightly enhanced due to overcorrection effects of the bremsstrahlung recovery algorithm. There are also notable differences in the hardware trigger for electrons and muons, that will be discussed in the following section.

Concerning tau leptons, they decay within the detector and therefore are reconstructed through their decay products. However, for conservation of lepton number, the decays always contain at least one neutrino, which escape detection. Hence, the B invariant mass of a decay containing a neutrino in the final state will peak at a value lower than the true B^0 meson mass and will exhibit degraded resolution. Approaches exploting the full kinematic of the decays are used to recover at least part of the energy loss, whenever possible.

2.4 Trigger

Trigger selections are defined in the most generic way, and each analysis selects events passing the most efficient triggers.

An analysis looking for events with a muon in the final state would choose as hardware trigger the muon trigger. The muon detector provides a very clear signature when a muon is present in the decay. Therefore, the muon hardware trigger, requiring at least one muon with transverse momentum higher than 1.5-1.8 GeV/c, depending on the data taking periods, has an efficiency higher than 90%. If the final state contains at least one muon, this is the best choice for the hardware trigger. It is, indeed what is used to select $B^0 \to K^{*0}\mu^+\mu^-$, $B^0 \to K^{*0}J/\psi(\to \mu^+\mu^-)$, $B^+ \to K^+\mu^\pm e^\mp$ and $B^0 \to K^{*0}\tau^\mp\mu^\pm$ decays.

For the decays $B^0 \to K^{*0}e^+e^-$, $B^0 \to K^{*0}J/\psi(\to e^+e^-)$ and $B^0 \to K^{*0}\tau^\mp e^\pm$, with no

muons in the final state, other hardware triggers need to be used. The electron and hadron triggers, based on an energy deposit in the electromagnetic and hadronic calorimeters higher than a threshold, are a natural choice. However, their efficiencies are much lower than the efficiency of the muon trigger. In fact, the calorimeters are subject to higher occupancy than the muon detector and therefore the energy thresholds needs to be higher than the one for the muons. For example, the threshold for the electron trigger require a transverse energy of the associated cluster in the electromagnetic calorimeter higher than 2.5 or 3.0 GeV, depending on the data taking period. In order to recover part of the efficiency, multiple trigger selections are used together. The B^0 mass resolution and the contributions of backgrounds will depend on the way in which the events were triggered. Therefore, in the analyses the candidates are separated in mutually exclusive categories, depending on the trigger selection.

In the R_{K^*} analysis, for example, the data samples of $B^0 \to K^{*0} e^+ e^-$ and $B^0 \to K^{*0} J/\psi (\to e^+ e^-)$ candidates are divided into three mutually exclusive categories, which in order of precedence contains: candidates for which one of the electrons from the B^0 decay satisfies the hardware electron trigger (L0E); candidates for which one of the hadrons from the K^{*0} decay meets the hardware hadron trigger (L0H) requirements; and candidates triggered by activity in the event not associated with any of the signal decay particles (L0I).

In the $B^0 \to K^{*0} \tau^{\mp} e^{\pm}$ analysis, a similar approach is followed. Signal candidates belong to three mutually exclusive categories depending on whether the events were selected by: a high-energy electron from the signal candidate (eTOS); a reconstructed particle not belonging to the signal candidate (TIS); a reconstructed hadron from the signal candidate (hTOS).[1] Candidates in each category should not satisfy the requirements of the previous ones.

The software trigger selection has the role of identifying the typical topologies of b decays. In fact, it selects events with a two-, three- or four-track secondary vertex, with a significant displacement from the primary vertex (PV). At least one charged particle is required to have significant p_{T} and be inconsistent with originating from any PV. A multivariate algorithm [34] is used for the identification of secondary vertices consistent with the decay of a b-hadron.

2.5 Kinematic, topological and particle identification variables

After the trigger selection, kinematic, topological and particle identification variables are used to further discriminate signal from background. These variables are used both at the stripping level, with looser cuts to remove obvious background contributions, and in the offline analysis, with tighter cuts based on more optimized approaches. Some of the most effective variables are:

- χ^2_{IP}, which is the difference in χ^2 of a PV reconstructed with and without the B candidate; the PV with smallest χ^2_{IP} is selected as the best PV;
- χ^2_{VTX}, which is the significance of the vertex displacement with respect to the PV;

[1] TOS: Trigger On Signal, TIS: Trigger Independent of Signal

- ϑ_{DIRA}, which is the angle between the B momentum and the vector connecting the PV and the B vertex;
- FD and χ^2_{FD}, which are the flight distance of the particle and its significance, respectively;
- $\chi^2_{\rm VD}$, which is the χ^2 on the measured distance between the PV and the decay vertex;
- transverse momentum p_T of the particles;
- invariant masses m of intermediate states.

Other variables exploit the full kinematics of the decay. For example, the variable HOP used to select $B^0 \to K^{*0} e^+ e^-$ decays, is particularly effective to reduce background from partially reconstructed decays. This variable is defined as the ratio of the K^{*0} and the dielectron momentum component transverse to the B^0 direction of flight. This is expected to be unity, unless the electrons have lost some energy due to bremsstrahlung that was not recovered (see figure 2.5.1). In the approximation that bremsstrahlung do not modify the dielectron direction significantly, which is particularly valid for low dilepton masses, this ratio can be used to correct the momentum of the dielectron pair. The invariant mass of the signal candidate calculated using the corrected dielectron momentum, $m_{\rm corr}$, has a poor resolution that depends on $\chi^2_{\rm VD}$. Nevertheless, since the missing momentum of background candidates does not originate from the dielectron pair, $m_{\rm corr}$ still acts as a useful discriminating variable. Signal and partially reconstructed backgrounds populate different regions of the two-dimensional plane defined by $m_{\rm corr}$ and $\chi^2_{\rm VD}$ (see figure 2.5.2). In the $R_{K^{*0}}$ analysis, a requirements on this plane is set to reject background. A similar approach is followed in the $B^+ \to K^+ \mu^\pm e^\mp$ analysis, though in this case the ratio HOP is directly used in a multivariate selection.

Particle identification variables are another extremely powerful tool for background rejection. They are based on information from the RICHes, the muon detector and calorimeters and allow to distinguish particles species, in particular protons, kaons, pions, electrons and muons. The information are often combined in a multivariate algorythm and expressed in terms of probability. Particle identification variables ensures the suppression of candidates from decays with misidentification of at least one particle.

The performance of the PID is not perfectly simulated. This is because the simulation of the propagation of Cherenkov light in the RICHes is a particularly difficult problem. Reliable performances are measured using high-purity calibration data samples of muons from $B \to X J/\psi(\to \mu^+\mu^-)$ decays, electrons from $B^+ \to K^+ J/\psi(\to e^+e^-)$ decays, and kaons from $D^{*+} \to D^0(\to K^-\pi^+)\pi^+$ decays [43] are applied to simulation. The calibration data are binned in the particle's momentum and pseudorapidity, and in the detector occupancy. Particle identification variables for the simulated data sets are then sampled from the distributions of calibration data in the corresponding bin. Analogously, control samples are used to correct kinematic and topological variables which would show differences between data and simulation.

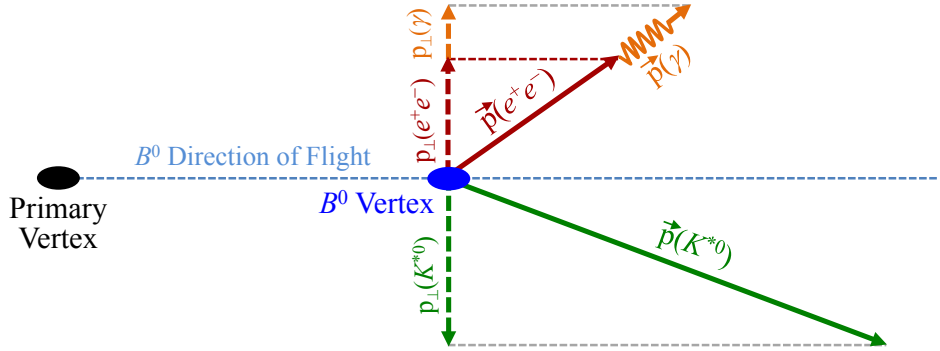

Figure 2.5.1: Sketch of the topology of a $B^0 \to K^{*0}e^+e^-$ decay. The transverse momentum lost via bremsstrahlung is evaluated as the difference between the $p_{\rm T}$ of the K^{*0} meson and that of the dielectron system, where both are calculated with respect to the B^0 meson direction of flight. Bremsstrahlung photons that are not recovered by the reconstruction are assumed to follow the dielectron momentum direction.

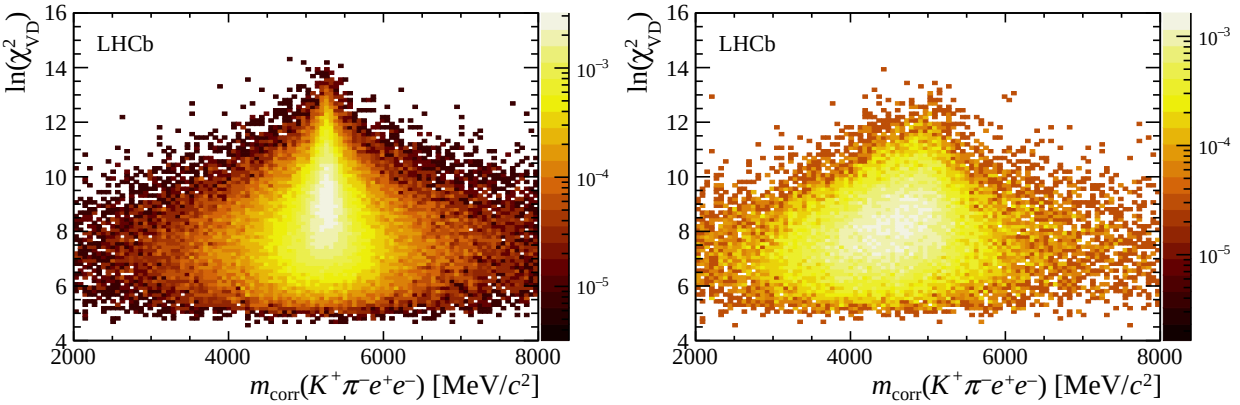

Figure 2.5.2: Distribution of $\chi^2_{\rm VD}$ as a function of $m_{\rm corr}$ for (left) $B^0 \to K^{*0}e^+e^-$ and (right) $B \to X(\to YK^{*0})e^+e^-$ simulated candidates. The distributions are normalised to the same number of candidates.

2.6 Offline selections

The offline selection is organised in successive steps with the aim of tackling the backgrounds of different nature. All analyses discussed in this document make use of multivariate approaches to combine efficiently the discriminating power of the various kinematic and topological variables and, in some cases, particle identification variables. If the multivariate training makes use of simulation, the variables are checked to well represent data using control samples and, in case discrepancies are found, correction factors are applied. As discussed above, this is always the case for particle identification variables, whose distributions are known to be

poorly reproduced by simulation.

Angular analysis

In the angular analysis, a boosted decision tree (BDT) [44, 45] trained using $B^0 \to J/\psi K^{*0}$ candidates as signal proxy and data in the upper mass sideband [5350, 7000] as background proxy is used to reject combinatorial background. A k-folding technique [46] with k=10 is adopted to fully exploit the training samples without biasing the output of the classifier. The selection is optimized maximizing the Punzi figure of merit, ensuring high signal significance. This BDT allows a rejection of 97% of background events while keeping 85% efficiency on signal.

It is particularly important to reject backgrounds that could alter the distributions of the selected candidates and therefore the measurement of the angular observables. Physics processes which constitute a source of background are summarized in table 2.6.1, indicating the background process and the selection strategy used to reduce or remove it. All of the sources of physics background are studied using samples of simulated events. After selection, they are sufficiently small to be neglected in the angular analysis but are considered further as sources of systematic uncertainty. The largest residual background is combinatorial in nature and varies smoothly $m(K^+\pi^-\mu^+\mu^-)$, $m(K^+\pi^-)$, and the decay angles.

Lepton universality test $R_{K^{*0}}$

In the lepton universality test, the separation of the signal from the combinatorial background is based on neural-network classifiers [47]. The same classifier is used for the resonant and nonresonant modes, but muon and electron channels are treated separately. The classifiers are trained using simulated $B^0 \to K^{*0}\ell^+\ell^-$ decays, corrected for known differences between data and simulation (see section 4.2), as signal proxy. Data candidates with $K^+\pi^-\ell^+\ell^-$ invariant masses larger than $5400\,\mathrm{MeV}/c^2$ and $5600\,\mathrm{MeV}/c^2$ are used as background proxies for the muon and electron channel, respectively. The training uses a k-folding technique with $k = 10$. The most discriminating variable in this case is χ^2_{fit}, which is the quality of the kinematic fit to the decay chain performed constraining the B^0 candidate to originate from the primary vertex. The selection is optimized maximizing the signal significance.

For the muon modes, a requirement on the four-body invariant mass of the B^0 candidate to be larger than $5150\,\mathrm{MeV}/c^2$ excludes backgrounds due to partially reconstructed decays, $B \to K^{*0}\mu^+\mu^- X$, where one or more of the products of the B decay, denoted as X, are not reconstructed. A kinematic fit that constrains the dielectron mass to the known J/ψ mass allows the corresponding background to be separated from the $B^0 \to K^{*0} J/\psi(\to e^+e^-)$ signal by requiring the resulting four-body invariant mass to be at least $5150\,\mathrm{MeV}/c^2$.

After the full selection, 1 to 2% of the events contain multiple candidates. This fraction is consistent between the resonant and nonresonant modes, and between final states with electrons and muons. About half of the multiple candidates are due to cases where the kaon is misidentified as the pion and vice versa. Only one candidate, chosen randomly, is retained.

The distribution of q^2 as a function of the four-body invariant mass for the B^0 candidates is shown in figure 2.6.1 for both muon and electron final states. The requirements on the

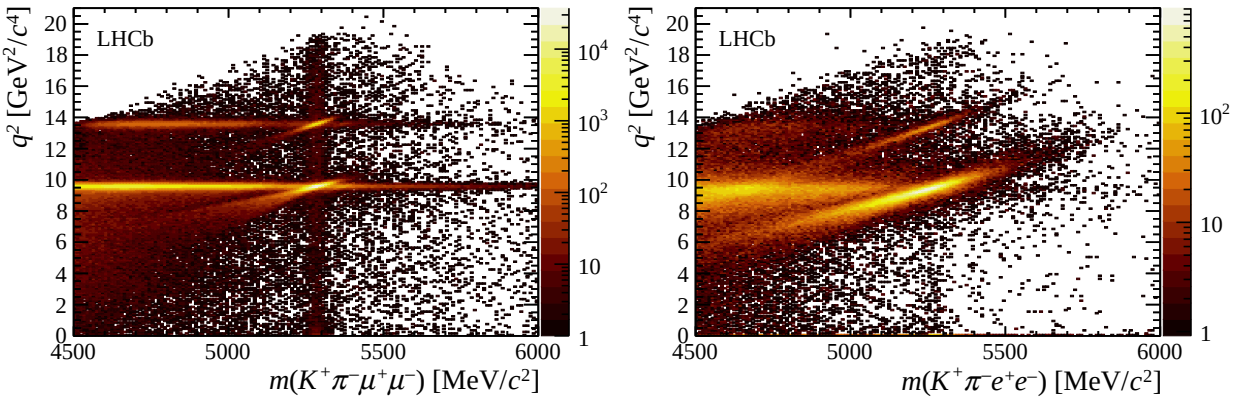

Figure 2.6.1: Number of candidates for $B^0 \to K^{*0}\ell^+\ell^-$ final states with (left) muons and (right) electrons as a function of the dilepton invariant mass squared, q^2, and the four-body invariant mass of the B^0.

neural-network classifier is not applied. In each plot, the contributions due to the charmonium resonances are clearly visible at the J/ψ and $\psi(2S)$ masses. For electrons, these distributions visibly extend above the nominal mass values due to the calorimeter resolution affecting the bremsstrahlung recovery procedure. The empty region in the top left corresponds to the kinematic limit of the $B^0 \to K^{*0}\ell^+\ell^-$ decay.

Physics background are summarized in table 2.6.1, indicating the process and the selection strategy used to reduce or remove it. They are more abudant for the electron channels. The residual ones are parameterized in the fit to the data, as discussed in 4.

Lepton flavor violating searches

The lepton-flavor-violating analyses described in this document make use of multiple multivariate selections in sequence, specifically dedicated to the rejection of combinatorial background or partially reconstructed and physics backgrounds.

Search for $B^+ \to K^+\mu^\pm e^\mp$ decays

In the case of $B^+ \to K^+\mu^\pm e^\mp$, obvious backgrounds from double semileptonic B decays and decays involving charmonium resonances are removed at an early stage by vetoes on D mesons and J/ψ. The most significant backgrounds originate from partially reconstructed B^+ decays, *e.g.* from double semileptonic $B^+ \to \overline{D}^0 X \ell^+ \nu_\ell$ with $\overline{D}^0 \to K^+ Y \ell'^- \overline{\nu}_{\ell'}$ decays, where X and Y represent hadrons, while ℓ and ℓ' are leptons. They are removed by imposing the requirement $m(K^+\ell^-) > 1885\,\text{MeV}/c^2$. Kaon and electron candidates that have hits in the muon stations consistent with their trajectories are rejected.

The combinatorial background is reduced by a BDT combining a set of topological and kinematic variables, trained on simulated $B^+ \to K^+\mu^\pm e^\mp$ events corrected using $B^+ \to K^+ J/\psi(\to \mu^+\mu^-)$ and $B^+ \to K^+ J/\psi(\to e^+e^-)$ data control samples. Corrections are applied to the B-meson production kinematics, vertex quality, and detector occupancy, the latest

being represented by the number of tracks per event in the detector. The upper-mass sideband, corresponding to $m(K^+\mu^\pm e^\mp) \in [5385, 6000]\,\mathrm{MeV}/c^2$, is used as a proxy for the background, as this region is known to be dominated by combinatorial background. The training is performed using a k-folding with ten folds. The optimal requirement on the BDT classifier is chosen generating toys for evaluating the best expected upper limits on the branching fractions $\mathcal{B}(B^+ \to K^+\mu^\pm e^\mp)$.

The candidates surviving this first multivariate selection are used to train a second BDT, dedicated to reject background from partially reconstructed and physics b-hadron decays. The background sample for the training is taken from the lower-mass sideband in data, corresponding to $m(K^+\mu^\pm e^\mp) \in [4550, 4985]$ MeV/c^2, where the partially reconstructed background is expected to contribute in a dominant way. The signal proxy, instead, is the same as for the first BDT. The training procedure shares the k-folding approach and the same set of discriminating variables used to construct the first multivariate discriminant, with the addition of the HOP variable described in the previous section, particularly effective against partially reconstructed backgrounds. The requirements on this second BDT are optimized in the same manner as for the first BDT.

Particle identification criteria are finally applied to reject backgrounds from physics decays with at least one particle misidentified.

The potential contamination from b-hadron decays in the signal mass region after selection is analysed using dedicated simulated samples. Two categories are analysed: fully reconstructed B decays, with at least one particle in the final state misidentified, such as the semileptonic decays $B^+ \to K^+\ell^+\ell^-$ and $B^+ \to K^+ J/\psi(\to \ell^+\ell^-)$, or fully hadronic B^+ decays as $B^+ \to K^+\pi^+\pi^-$; partially reconstructed decays in which at least one particle is not reconstructed and one or more particles are misidentified, such as $B^0 \to K^{*0}\ell^+\ell^-$, $\Lambda_b^0 \to pK^-\ell^+\ell^-$, $\Lambda_b^0 \to pK^- J/\psi(\to \ell^+\ell^-)$ and $B^+ \to \overline{D}{}^0\ell^+\nu_\ell$ transitions, where the $\overline{D}{}^0$ meson decays further to $K^+\pi^-$ or $K^+\ell^-\overline{\nu}_\ell$. The expected number of candidates from each possible background source after the selection is evaluated from simulation and is found to be negligible.

Search for $B^0 \to K^{*0}\tau^\pm\mu^\mp$ and $B^0 \to K^{*0}\tau^\pm e^\mp$ decays

In the case of $B^0 \to K^{*0}\tau^\pm\mu^\mp$ and $B^0 \to K^{*0}\tau^\pm e^\mp$ decays, the amount of background is much larger, due to the higher number of particles in the final state and to the variety of charmed mesons that can fake hadronic tau decays. Fully reconstructed physics backgrounds are double semileptonic decays like and $B^0 \to D^{*-}\mu^+\nu$ with $D^{*-} \to \bar{D}{}^0\pi^-$ and $\bar{D}{}^0 \to K^+\pi^-\pi^+\pi^-$ for $B^0 \to K^{*0}\tau^-\mu^+$ channel. Note that an analogous does not exist for the $B^0 \to K^{*0}\tau^+\mu^-$ channel, which gives an example on how the two charge combination can be affected by different backgrounds. A special case is represented by fully reconstructed physics backgrounds where one or more particles are misidentified. This is the case, for example, for $B^0 \to D^{*-}\tau^+ nu$ with $D^{*-} \to \bar{D}{}^0\pi^-$ and $\bar{D}{}^0 \to K^+\mu^-\bar{\nu}$ and $\tau \to \pi^+\pi^-\pi^+\bar{\nu}$ for $B^0 \to K^{*0}\tau^+\mu^-$ channel. The presence of misidentification in general implies a mass shift of these backgrounds with respect to the signal. Unfortunately, despite the shift, many of these backgrounds are still affecting the signal region, given the poor mass resolution of the B candidates because of missing neutrinos.

The first stage of the selection is the multivariate discrimination exploiting the different

topologies of signal decays and combinatorial background, also making use of events from the upper sideband as proxy for the combinatorial background. The following step is used to reject charm meson decaying into three prongs faking taus. It exploits the kinematics of the tau hadronic decay into three pions and a neutrino. This proceeds through the decay chain $\tau \to a_1(\to \rho(\to \pi\pi)\pi)\nu$, which is sensibly different from the dynamic of a charmed meson decays. Particle identification criteria are used to reject physics backgrounds with misidentified particles. Additionally, requirements on the K^{*0} invariant mass and tau mass transverse to the B direction of flight are applied. A multivariate discriminant is used to combine different variables exploiting the isolation property of the signal. A particle selected from a partially reconstructed background is usually surrounded by other particles of the decays which are not used to reconstruct the event. The training uses events from the lower mass sideband as proxy for physics backgrounds. A powerful variable against physics backgrounds used at the last stage is the tau flight distance significance χ^2_{FD}, which further rejects charmed mesons. Even after these selection procedure, some physics background with charm meson remains. They are identified performing all possible combinations of invariant mass of subset of particles in the final state, including also the possibility of misidentification, and whenever a peaking structure compatible with a charm meson is identified, it is removed by a dedicated veto.

After the whole selection, the remaining background is a combination of partially reconstructed physics processes and a data driven approach using control regions is used to parameterize their contribution in a maximum likelihood fit, as will be discussed in 5.

Table 2.6.1: Summary of relevant background decays and selection strategies for the angular and $R_{K^{*0}}$ analyses.

Background decay	**Selection**
$B^0 \to K^{*0} V(\to \ell^+\ell^-)$ $V = \rho$, ω, or ϕ	In angular: $q^2 \notin (0.98, 1.10)$ GeV$^2/c^4$ In $R_{K^{*0}}$: contamination $< 2\%$, negligible as similar for μ and e
$B^0 \to K^{*0} J/\psi(\to \mu^+\mu^-)$ $B^0 \to K^{*0}\psi(2S)(\to \mu^+\mu^-)$	$q^2 \notin (8, 11)$ GeV$^2/c^4$ $q^2 \notin (12.5, 15.0)$ GeV$^2/c^4$
$B^0 \to K^{*0} J/\psi(\to \mu^+\mu^-)$ $B^0 \to K^{*0}\psi(2S)(\to \mu^+\mu^-)$ with swapped identity of one hadron (h) and one μ.	$m(h_\mu\mu)^2 \notin (8, 11)$ GeV$^2/c^4$ $m(h_\mu\mu)^2 \notin (12.5, 15)$ GeV$^2/c^4$ (h_μ is swapped hadron under muon mass hypothesis)
$B^0 \to D^-(\to K^{*0}\ell^-\overline{\nu})\ell^+\nu$ Non-peaking background with a branching fraction four orders of magnitude larger than the signal.	In angular: D veto In $R_{K^{*0}}$: $\lvert\cos\vartheta_\ell\rvert < 0.8$
$B^+ \to K^+\ell^+\ell^-$ Combined with a low-momentum π^- from the rest of the event, populates the upper mass sideband region used for training the neural-network classifiers.	In angular: $m(K^+\mu^+\mu^-) \notin (5220, 5340)$ MeV/c^2 In $R_{K^{*0}}$: $m(K^+\ell^+\ell^-) < 5100$ MeV/c^2. Candidates where the π^- from the K^* is misidentified as a kaon and paired with a π^+ are similarly rejected.
$B_s^0 \to \phi(\to K^+K^-)\ell^+\ell^-$ One kaons is misidentified as a pion.	In angular: Tight PID criteria if $m(K\pi_K\mu\mu)$ and $m(K\pi_K)$ are consistent with the known B_s^0 and ϕ masses. In $R_{K^{*0}}$: $m(K\pi_K) > 1040\,\text{MeV}/c^2$.
$B^{0,+} \to K^{*0,+}\ell^+\ell^-$ Pion from $K^{*0,+}$ replaced by another pion in the event.	Not peaking, included in combinatorial parameterization
$B^0 \to K^{*0}\ell^+\ell^-$ Can be background to $\bar{B}^0 \to \bar{K}^{*0}\ell^+\ell^-$ (and vice versa) if the K^+ (K^-) is misidentified as the π^+ (π^-) and the π^- (π^+) is misidentified as the K^- (K^+).	Tight PID criteria.
$\Lambda_b^0 \to pK^-\mu^+\mu^-$ Proton misidentified as pion.	Tight pion PID if $m(\pi_p K\mu\mu)$ close to $m(\Lambda_b^0)$
$\Lambda_b^0 \to pK^-\mu^+\mu^-$ Double misidentification of the hadrons, i.e., where the proton is misidentified as a kaon and the kaon is misidentified as a pion.	Tight PID criteria.

Chapter 3

The angular analysis of $B^0 \to K^{*0}\mu^+\mu^-$ decays

The angular analysis of $B^0 \to K^{*0}\mu^+\mu^-$ decays [1] described in this chapter and published in 2016 is based on an integrated luminosity of 3 fb^{-1} recorded by the LHCb detector in pp collisions at centre-of-mass energy of 7 and 8 TeV during 2011 and 2012, respectively. Previous analyses had only fitted simplified angular distributions, whereas this paper could take advantage of a data sample large enough to measure for the first time the full angular distribution. This was a pivotal step in the field, because it allowed the evaluation of correlations among variables and therefore the use of all the observables in simultaneous phenomenological global fits. The global tension with the SM seen in this analysis, corresponding to about 3.4 standard deviations, has been confirmed by later LHCb updates and by measurements in other experiments which have found similar or compatible deviations, and still stands as one of the puzzling results in FCNC measurements.

3.1 Analysis strategy

Three separate techniques have been used to study the angular distributions and measure the related observables:

- **Unbinned maximum likelihood fit.** It is used to determine the CP-averaged observables F_L, $A_{\rm FB}$, and S_3–S_9, as well as the CP asymmetries A_3–A_9, averaged over bins of q^2. In addition, the P_i' observables are determined by reparameterising the likelihood fit. The data are analysed in q^2 bins of approximately 2 GeV$^2/c^4$ width. Measurements are done also in the wider $1.1 < q^2 < 6.0$ GeV$^2/c^4$ and $15.0 < q^2 < 19.0$ GeV$^2/c^4$ bins, for which there are particularly precise theoretical predictions.

- **Method of moments.** The same set of observables described above are also determined using principal angular moments. The advantage of this method [48, 49] is that it does not require a complex angular fit, is robust and allows to extract simultaneously many observables with few events. The results can be calculated using a larger number of bins, giving additional shape information as function of q^2. In this analysis, approximately

1 GeV$^2/c^4$ wide q^2 bins are used. On the other hand, the statistical precision of the measurement is lower if compared to a likelihood fit approach: it gives an approximately 15% less precise determination of the observables.

- **Amplitude analysis.** The observables S_4, S_5, and $A_{\rm FB}$ vary as a function of q^2 and are known to change sign in the Standard Model. By fitting for the decay amplitudes as a function of q^2, the zero-crossing points, i.e. the q^2 values at which these observables are zero, can be determined. At leading order, the zero-crossing points are free from $B^0 \to K^{*0}$ form-factor uncertainties [50, 51]. The method is applied in the range $1.1 < q^2 < 6.0$ GeV$^2/c^4$

These three methods are complementary, but their results are correlated and cannot be combined.

3.2 The angular acceptance

The distributions of the B candidates as function of q^2 and the decay angles ϑ_ℓ, ϑ_K and ϕ depend on the physics properties of the decay. However, the criteria used to trigger, reconstruct and select the candidates introduce an acceptance which is not uniform, distorting these distributions. A relevant effect comes from momentum and impact parameter requirements. In particular, the implicit momentum threshold required for tracks to traverse the magnetic spectrometer removes low-momentum particles. This is the reason why the $cos(\vartheta_\ell)$ and $cos(\vartheta_K)$ distributions are depleted at the borders. The effect is symmetric for $cos(\vartheta_\ell)$ because the two leptons have the same mass, while it is asymmetric for $cos(\vartheta_K)$ because of the different mass of the kaon and the pion.

It is therefore crucial to correctly evaluate and parametrise the acceptance as function of the four variables. The efficiency is parametrised in four dimensions, according to:

$$\varepsilon(\cos\vartheta_\ell, \cos\vartheta_K, \phi, q^2) = \sum_{i,j,m,n} c_{ijmn}\, L_i(\cos\vartheta_\ell)\, L_j(\cos\vartheta_K)\, L_m(\phi)\, L_n(q^2). \tag{3.2.1}$$

The terms $L_h(x)$, with $x = cos\vartheta_\ell$, $cos\vartheta_K$, ϕ or q^2, denote Legendre polynomials of order h. The sum includes $L_h(x)$ up to fourth, fifth, sixth and fifth order for $\cos\vartheta_\ell$, $\cos\vartheta_K$, ϕ, and q^2, respectively. The observables are rescaled to the range $-1 < x < +1$ when evaluating the polynomial. The coefficients c_{ijmn} are determined using a principal moment analysis of simulated three-body $B^0 \to K^{*0}\mu^+\mu^-$ phase-space decays. As the efficiency is parametrised in terms of all the relevant kinematic variables needed to describe the decay, it does not depend on the model used in the simulation. The phase-space simulation has the advantage of covering uniformly the distributions of the angles, providing enough events in each region to precisely determine the acceptance.

The angular acceptance in $\cos\vartheta_\ell$, $\cos\vartheta_K$ and ϕ is shown for $0.10 < q^2 < 0.98$ GeV$^2/c^4$ and $18.0 < q^2 < 19.0$ GeV$^2/c^4$ in Figure 3.2.1. The acceptance varies smoothly as a function of q^2 between these extremes. The acceptance as a function of q^2, after integrating over the decay angles, is also shown.

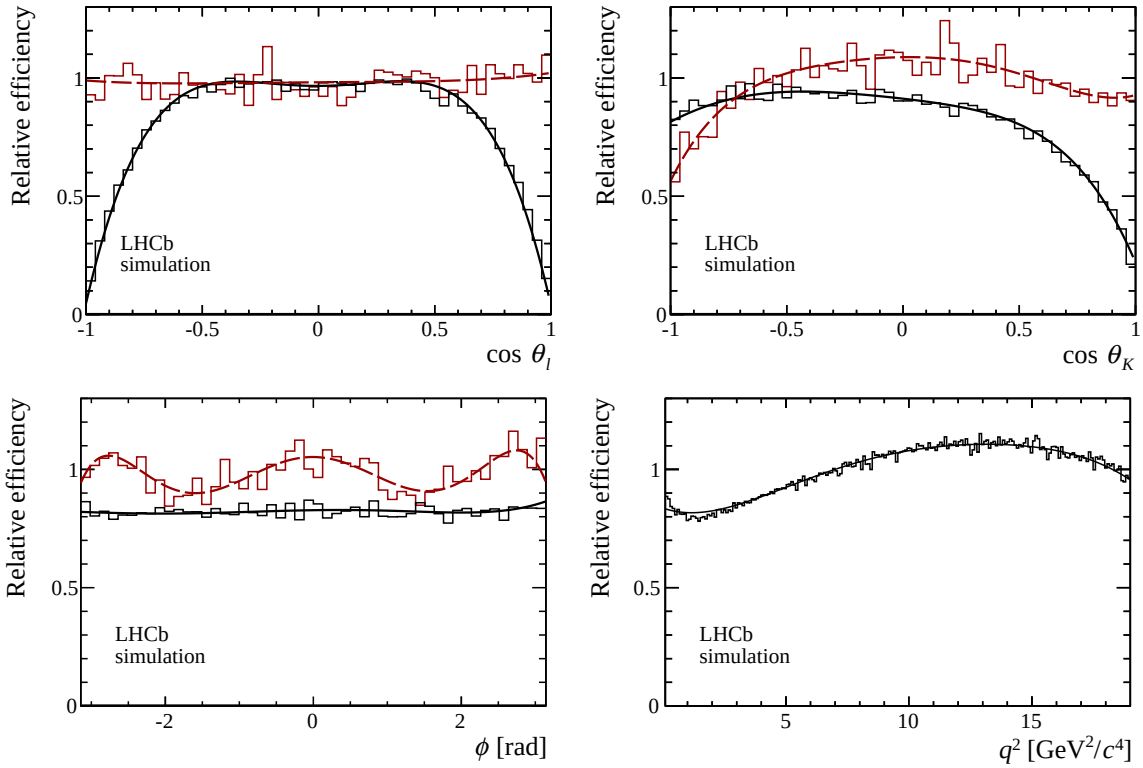

Figure 3.2.1: Relative efficiency in $\cos\vartheta_\ell$, $\cos\vartheta_K$ and ϕ for the regions $0.10 < q^2 < 0.98$ GeV$^2/c^4$ (black solid) and $18.0 < q^2 < 19.0$ GeV$^2/c^4$ (red dashed). The relative efficiency as function of q^2 is shown in the bottom right plot.

The description of the angular acceptance is cross-checked using the decay $B^0 \to J/\psi K^{*0}$. This decay can be selected in the data with background contamination below 1%. The acceptance correction derived using the method described above is used in an angular fit of the $B^0 \to J/\psi K^{*0}$ data. The result is consistent with the angular structure previously determined by the BaBar, Belle, and LHCb collaborations [52–54].

3.3 Unbinned maximum likelihood fit

The angular observables introduced in Section 1.4 are measured in each q^2 bin by an unbinned maximum likelihood fit to the distributions of $m(K^+\pi^-\mu^+\mu^-)$ and the three decay angles $\cos\vartheta_\ell$, $\cos\vartheta_K$ and ϕ.

The $K^+\pi^-\mu^+\mu^-$ invariant mass effectively operates the discrimination between signal and background. The signal component is modelled using the sum of two Gaussian functions with a common mean, each with a power-law tail on the low-mass side. The parameters of this shape are extrapolated from a fit to $B^0 \to J/\psi K^{*0}$ candidates on data, where contamination from $\bar{B}^0_s \to J/\psi K^{*0}$ decays, negligible for $B^0_s \to K^{*0}\mu^+\mu^-$ decays but at a level of 0.8% of the $B^0 \to J/\psi K^{*0}$ signal yield, is accounted for to avoid biases. A scale factor, evaluated on

$B^0 \to K^{*0}\mu^+\mu^-$ simulated events and ranging between 2-8%, is used to correct the width of the Gaussian functions in the different q^2 bins. Combinatorial background, instead, is modelled by a single exponential distribution.

The selected $K^+\pi^-$ system is dominated by a P-wave, but could be contaminated by an S-wave component. A fit to the $m(K^+\pi^-)$ distribution, using a relativistic Breit–Wigner function for the P-wave component, the LASS parametrisation [55] for the S-wave component and a linear function for the combinatorial background, allows to constraint the S-wave component. Concerning the possible contributions from the tails of higher-mass K^* states, simulation studies indicate that any bias arising from these states is negligible compared to the statistical uncertainty on the angular observables.

For the angular distributions, the signal component is described using Eq. 1.4.10 and taking into account the effect of the acceptance, in a different way depending on the q^2 range. In the narrow q^2 bins, the acceptance is treated as constant across each bin and therefore included in the fit by multiplying Eq. 1.4.10 by the acceptance function evaluated at the bin centre. In the wider $1.1 < q^2 < 6.0$ GeV$^2/c^4$ and $15.0 < q^2 < 19.0$ GeV$^2/c^4$ bins, instead, the shape of the acceptance can vary significantly across the bin. In this case, the candidates are weighted in the likelihood fit by the inverse of their efficiency. The event weights are scaled such that the fit has confidence intervals with the correct coverage. For the background, the angular distribution is modelled with second-order polynomials in $\cos\vartheta_\ell$, $\cos\vartheta_K$ and ϕ, the parameters of which are left free in the fit. The background angular distribution is assumed to factorise in the three decay angles, an assumption validated in the upper mass sideband.

The $B^0 \to K^{*0}\mu^+\mu^-$ signal yield, integrated over the q^2 ranges $0.1 < q^2 < 8.0$ GeV$^2/c^4$, $11.0 < q^2 < 12.5$ GeV$^2/c^4$ and $15.0 < q^2 < 19.0$ GeV$^2/c^4$, is determined to be 2398 ± 57. The signal yield in the range $1.1 < q^2 < 6.0$ GeV$^2/c^4$ is 624 ± 30.

The signal fraction and F_S are common parameters in the simultaneous fits to the $m(K^+\pi^-)$ distribution and to the angular and $m(K^+\pi^-\mu^+\mu^-)$ distributions. Figure 3.3.1 shows the projections of the fitted probability density function on the angular and mass distributions for the $1.1 < q^2 < 6.0$ GeV$^2/c^4$ bin. Good agreement of the fitted function with the data is observed also for the other q^2 bins.

The P_i' observables introduced in Section 1.4 are determined by reparametrising Eq. 1.4.10 using a basis comprising F_L, P_1, P_2, P_3 and P_4', P_5', P_6', P_8'. The CP asymmetries are determined by modifying the angular convention, introducing a relative sign between the angular terms $f_3(\vec{\Omega})$–$f_9(\vec{\Omega})$ for B^0 and $\bar{B}^0$ decays, such that Eq. 1.4.10 is given in terms of F_L and the CP asymmetries A_3–A_9. The B^0 or $\bar{B}^0$ flavour is determined from the charge of the final-state kaon.

To ensure correct coverage for the uncertainties of the angular observables, the Feldman–Cousins method [56] is used with nuisance parameters treated according to the plug-in method [57]. Angular observables are considered one at a time, with the other angular observables treated as nuisance parameters. The nuisance parameters also include the signal fraction, the background parameters, F_S, and the angular terms that arise from interference between the S- and P-wave.

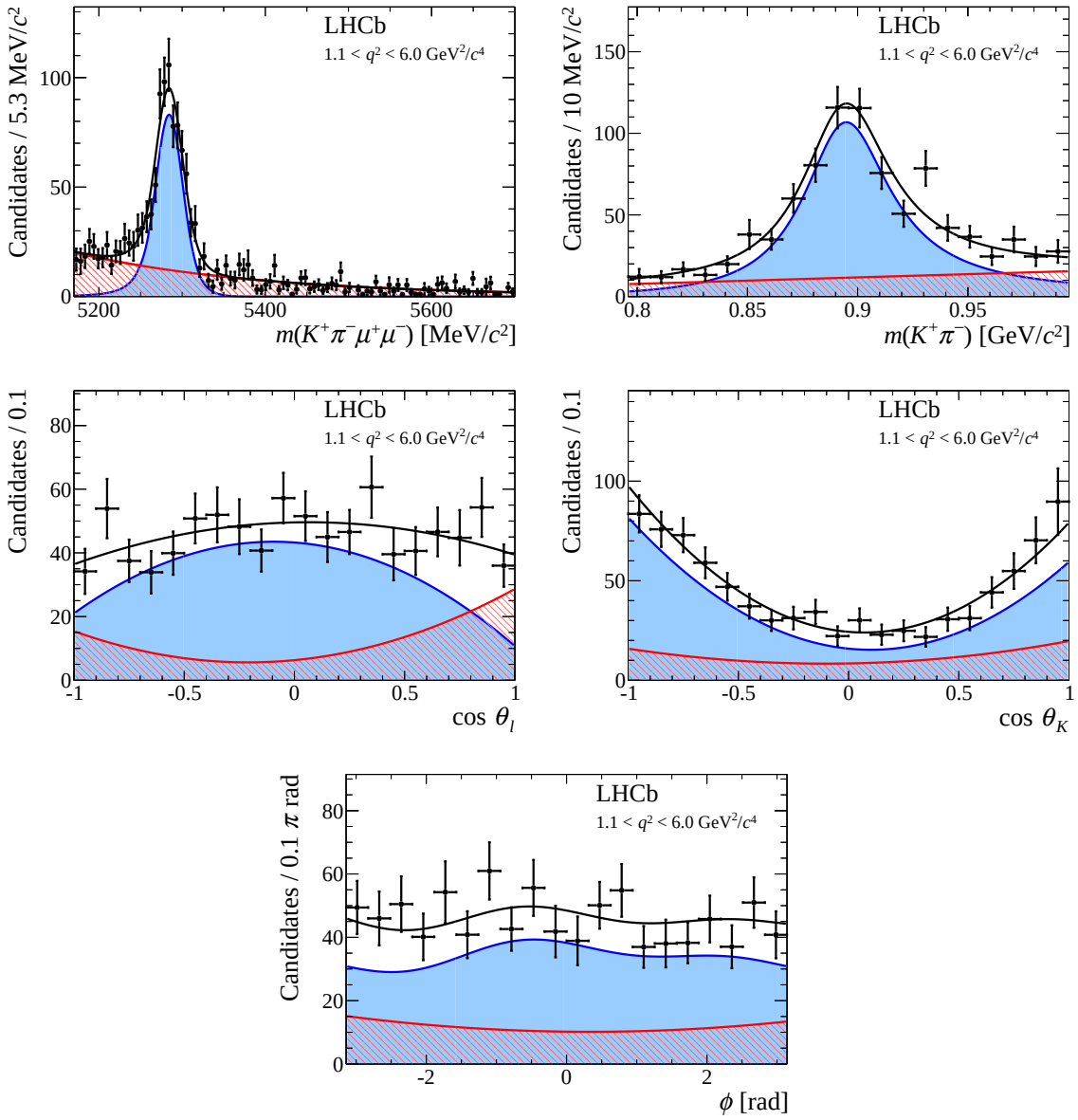

Figure 3.3.1: Fit of the mass and angular distributions in the $1.1 < q^2 < 6.0$ GeV$^2/c^4$ region. Candidates have been weighted to account for the acceptance. The blue and red areas indicates the signal and background contributions, respectively.

3.4 Method of Moments

A principal moment analysis of the angular distribution allows to determine the angular observables without performing a fit to the data. The moments of the angular distribution as

function of q^2 are defined by:

$$M_i(q^2) = \frac{1}{\dfrac{d(\Gamma+\bar{\Gamma})}{dq^2}} \int \frac{d^4(\Gamma+\bar{\Gamma})}{dq^2\, d\vec{\Omega}}\, f_i(\vec{\Omega})\, d\vec{\Omega}, \tag{3.4.1}$$

where $f_i(\vec{\Omega})$ are the angular functions defined in Eq. 1.4.11, and $\vec{\Omega} = (\cos\vartheta_\ell, \cos\vartheta_K, \phi)$ represents the decay angles. The function $d^4(\Gamma+\bar{\Gamma})/dq^2\, d\vec{\Omega}$ denotes the differential decay rate summed over B^0 and $\bar{B}^0$ decays.

The average $M_i(q^2)$ in a bin of q^2 is estimated by replacing the integral in Eq. 3.4 with a sum over the candidates in the dataset. The angular acceptance is accounted for by weighting the candidates with w_e, i.e. the reciprocal of the candidate's efficiency:

$$\hat{M}_i = \frac{\sum_e w_e f_i(\vec{\Omega}_e)}{\sum_e w_e}, \tag{3.4.2}$$

The sum is evaluated over all candidates within ± 50 MeV/c^2 of the B^0 mass, containing more than 95% of the signal candidates. This sum is also computed for a control and sideband regions to estimate background contributions and subtract it. The functions f_i are given in Table 1.4.1. Due to their dependence on spherical harmonics, most of the angular terms are orthogonal. For f_i with $i = 3$–9,

$$\int f_i(\vec{\Omega}) f_j(\vec{\Omega})\, d\vec{\Omega} = \kappa_i\, \delta_{ij}, \tag{3.4.3}$$

such that the moments give the CP-averaged observables S_3 to S_9 with a coefficient κ_i that takes into account the normalisation. In the limit of massless muons, the moments are related to the observables by the expressions

$$M_i = \begin{cases} \frac{8}{25}(1-F_S)S_i & \text{if } i = 3,4,8,9, \\ \frac{2}{5}(1-F_S)S_i & \text{if } i = 5,6s,7, \\ \frac{2}{5}(1-F_S)(2-F_L) + \frac{2}{3}F_S & \text{if } i = 1s. \end{cases} \tag{3.4.4}$$

where $A_{\rm FB} = \frac{3}{4}S_{6s}$. The relevant signal and background yields, and the S-wave fraction F_S, are determined from a two-dimensional extended unbinned maximum likelihood fit to the $m(K^+\pi^-\mu^+\mu^-)$ and $m(K^+\pi^-)$ distributions.

The statistical uncertainties of the angular moments are estimated using a bootstrapping technique [58]. Confidence intervals are defined such that they include the 16th–84th percentiles of the bootstrap distribution of the observables. When computing the $P_i^{(\prime)}$ observables, bootstrapped data with unphysical F_L ($F_L < 0$ or $F_L > 1$) are added at $\pm\infty$ to ensure that the resulting intervals do not undercover. As in the likelihood method, the CP asymmetries are determined by flipping the sign of the relevant B^0 angular terms. The resulting moments are then used to determine the CP asymmetries by substituting A_i for S_i in Eq. (3.4.4).

In the moment analysis, an additional angular observable that is not present in the massless limit is determined. This observable, sensitive to large new scalar or tensor contributions to the decay, is associated with a new forward-backward asymmetry of the dimuon system, $f_{6c}(\vec{\Omega}) = \cos^2\vartheta_K \cos\vartheta_\ell$. It is highly correlated to $A_{\rm FB}$, but can be determined from the moments M_{6c} and M_{6s} as: $S_{6c} = 8M_{6c} - 2M_{6s}$.

3.5 Determination of zero-crossing points using the decay amplitudes

The amplitudes $A^{L,R}_{0,\parallel,\perp}$, appearing in Table 1.4.1, can be determined in the $1.1 < q^2 < 6.0\,\mathrm{GeV}^2/c^4$ region using a smoothly varying q^2-dependent parametrisation. A parametrisation for $q^2 \gtrsim 6.0\,\mathrm{GeV}^2/c^4$ is complicated by the presence of resonant $c\bar{c}$ states and below $1.1\,\mathrm{GeV}^2/c^4$ by the presence of light resonances.

The amplitudes $A^{L,R}_{0,\parallel,\perp}$ are complex functions of q^2 and therefore, at each point in q^2, the decay $B^0 \to K^{*0}\mu^+\mu^-$ is described by twelve real degrees of freedom. Exploiting the invariance of the angular distribution of the final-state particles under certain symmetry transformations [59], four components of the amplitudes can be set to zero. With this simplification, only eight independent degrees of freedom are needed to fully describe the $B^0 \to K^{*0}\mu^+\mu^-$ decay. In this analysis, following prescription in [60], the following choice is made:

$$\mathrm{Re}(A^R_0) = \mathrm{Im}(A^R_0) = \mathrm{Im}(A^L_0) = \mathrm{Im}(A^R_\perp) = 0. \tag{3.5.1}$$

and the P-wave amplitudes are parametrised as

$$A^{L,R}_{i=0,\parallel,\perp}(q^2) = \alpha^{L,R}_i + \beta^{L,R}_i q^2 + \frac{\gamma^{L,R}_i}{q^2}, \tag{3.5.2}$$

where $\alpha^{L,R}_i$, $\beta^{L,R}_i$, and $\gamma^{L,R}_i$ are complex coefficients.

Within the considered q^2 range, the S-wave amplitudes are expected to vary slowly [61]. They are therefore assumed to be constant in q^2 and described by a single complex parameter. The systematic uncertainty related to this approximation is negligible. After applying the symmetry constraints, the B^0 and $\bar{B}^0$ decays are each described by 24 real parameters for the P-wave amplitudes and 4 real parameters for the S-wave amplitudes. Given the 3 fb^{-1} dataset, it is not feasible to extract the parameters for B^0 and $\bar{B}^0$ decays independently. Therefore, it is assumed that CP symmetry holds in the decay, such that the amplitudes describing the B^0 and $\bar{B}^0$ decays are identical.

An unbinned maximum likelihood fit to the distributions of $m(K^+\pi^-\mu^+\mu^-)$, $\cos\vartheta_\ell$, $\cos\vartheta_K$, ϕ, and q^2 is used to determine the amplitude parameters. The integral of the angular distribution is required to match the number of signal candidates in the fit. For simplicity, $m(K^+\pi^-)$ is not included directly in the fit. The variation of the amplitudes with $m(K^+\pi^-)$ is taken into account by replacing products of amplitudes $A^{L,R}_i A^{L,R*}_j$ with

$$A^{L,R}_i A^{*L,R}_j \int g_i(m(K\pi))\, g^*_j(m(K\pi))\, dm(K\pi), \tag{3.5.3}$$

where $g_i(m(K\pi))$ describes the variation of the amplitude $A_i^{L,R}$ with $m(K^+\pi^-)$.

The acceptance as a function of $\cos\vartheta_\ell$, $\cos\vartheta_K$, ϕ and q^2 is included in the amplitude fit. The combinatorial background is modelled by a linear function in q^2. The background angular distribution is assumed to be independent of q^2 and is parametrised by a product of three second-order polynomials in the angular variables. The validity of this model and the factorisation assumption in decay angles and q^2 is checked using candidates in the $m(K^+\pi^-\mu^+\mu^-)$ sidebands.

The amplitude parameters are used to construct angular observables as continuous functions of q^2. The observables S_4, S_5 and $A_{\rm FB}$ exhibit zero-crossing points, which are extracted solving a quartic equation. The different solutions of this equation are separable based on the sign of the slope of the observable in the vicinity of the zero-crossing point. Only zero-crossing points in the range $1.1 < q^2 < 6.0$ GeV$^2/c^4$ with a local slope consistent with the data above 6.0 GeV$^2/c^4$ are retained.

The large number of parameters floating in the fit, coupled with the limited number of signal candidates present in the dataset, results in a non-parabolic likelihood surface. Therefore, as in the determination of the angular moments, the statistical uncertainties of the q^2-dependent observables and their corresponding zero-crossing points are determined using a bootstrapping technique [58]. The statistical coverage of the resulting intervals is checked using simulated events and is found to be correct for the observables S_4, S_5, and $A_{\rm FB}$. Despite the coverage being correct, approximately 10% of the bootstrapped datasets result in no zero-crossing point with the correct slope in the q^2 range $1.1 < q^2 < 6.0$ GeV$^2/c^4$. In these cases, the zero-crossing point is added to the bootstrap distribution at $\pm\infty$ to ensure that the method does not undercover.

The determination of the q^2-dependent amplitudes in principle allows the full observable basis to be determined. However, pseudoexperiments indicated that a dataset larger than $3\,{\rm fb}^{-1}$ was required in order to guarantee the correct coverage of the uncertainties on the observables other than S_4, S_5 and $A_{\rm FB}$.

3.6 Systematic uncertainties

Effects that can alter the mass or angular distribution of either the signal or background candidates are sources of systematic uncertainty. Their size is estimated using pseudoexperiments in which one or more parameters are varied and the angular observables are determined using the nominal and the systematically varied model. For each observable, in each q^2 region, the systematic uncertainty is then taken as the average of the difference between the two models. The pseudoexperiments are generated with signal yields many times larger than that of the data, to avoid statistical fluctuations. They are discussed below and summarized in Table 3.6.1.

Signal angular acceptance

The main systematic effects associated with the signal modelling arise from the estimate of the angular acceptance. Four effects are considered:

- The limited size of the simulation sample used to evaluate the acceptance. Pseudo-experiments are generated by coherently fluctuating the acceptance parameters according to the covariance matrix for the angular moments of the acceptance function.

- The parametrisation used to describe the acceptance. An alternative set of polynomials is used, simultaneously increasing the polynomial order by two for the q^2 and for each of the angular variables distributions.

- Residual data-simulation differences. The B^0 momentum spectrum, detector occupancy and PID performance of the simulation are corrected to match the data, and there is very good agreement between the properties of simulated and genuine $B^0 \to J/\psi K^{*0}$ decays. However, small residual differences remain in the momentum and transverse momentum spectra of the reconstructed pion. A new acceptance correction is derived after re-weighting the simulated phase-space sample to account for these differences. A more conservative variation is also considered, in which an acceptance correction is derived without applying any of the data-simulation corrections. The larger of the variations observed is added as a systematic uncertainty.

- The evaluation of the acceptance at a fixed point in q^2, for the narrow q^2 bins. Pseudo-experiments are generated to assess the bias introduced by this choice, by instead using the q^2 value at the left- or right-hand bin boundary.

Background angular modelling

A second-order polynomials is used to model the background angular distribution. A more complex model cannot be fit due to the limited number of background candidates. To test the approach used, the BDT requirement is relaxed increasing the sample size and the background candidates are fit with a fourth-order polynomial in each of the three angles. This shape is used to generate pseudo-experiments.

Additionally, for the amplitude analysis, the q^2 dependence of the background model is changed from a linear function to a third-order polynomial.

Impact of Peaking Backgrounds

As detailed in Section 2, the most significant backgrounds arise from the decays: $\Lambda_b^0 \to pK^-\mu^+\mu^-$; $B_s^0 \to \phi\mu^+\mu^-$, where a kaon or proton is misidentified as a pion; $B^0 \to K^{*0}\mu^+\mu^-$, where both the kaon and pion are misidentified. Pseudo-experiments are generated including these backgrounds and using their angular distributions as determined from simulated events. The angular observables are then determined as if these background were absent. Additional pseudo-experiments are generated using angular distributions of $B_s^0 \to \phi\mu^+\mu^-$ and $\Lambda_b^0 \to pK^-\mu^+\mu^-$ decays taken from data. These decays are selected by removing the PID information from the BDT and inverting the background vetoes.

Signal mass modelling

To evaluate the modelling of $m(K^+\pi^-\mu^+\mu^-)$, a fit is performed to $B^0 \to J/\psi K^{*0}$ data using as alternative model the sum of two Gaussian distributions without the power-law tails.

To assess the modelling of $m(K^+\pi^-)$, instead, pseudo-experiments are produced by varying the S- and P-wave line-shape parameters. For the S-wave, the LASS line-shape is also replaced by the sum of resonant $K_0^*(800)^0$ and $K_0^*(1430)^0$ contributions.

In the case of the amplitude analysis, the fit to the q^2-dependent decay amplitudes has an additional uncertainty due to the choice of the q^2 parametrisation of the S-wave amplitudes, which by default are taken to be constant in q^2. Motivated by Ref. [61], a systematic variation is considered by assuming that the S-wave amplitudes have the same q^2 dependence as the longitudinal P-wave amplitudes.

Detection and production asymmetries

The measured CP asymmetries can be biased due to detection and production asymmetries. The B^0 production asymmetry is measured to be less than 1% [62,63] and is further suppressed due to B^0–$\bar{B}^0$ mixing. The kaon detection asymmetry was measured in Ref. [64]. In contrast to the other sources of systematic uncertainty, the shift due to the detection and production asymmetries is calculated directly without generating pseudo-experiments. The systematic uncertainty on the angular observables A_i due to production and detection asymmetries is found to be less than 0.01. The effect of these asymmetries on the CP-averaged observables is negligible.

Observables definition

In the q^2 bin $0.10 < q^2 < 0.98$ GeV$^2/c^4$, the muon mass squared is comparable to q^2 and the relations between $S_{1(s,c)}$, $S_{2(s,c)}$ and F_L are only approximate. The assumption that these relations hold has no impact on the measured values of S_3–S_9 or A_3–A_9, but results in a biased estimate of F_L and hence of the P_i' observables. In pseudo-experiments based on the SM, this bias is typically at the level of 0.02. This can be accounted for in the SM predictions for this q^2 bin and hence is not considered as a source of systematic uncertainty.

Summary of systematics impact

These systematic uncertainties are negligible compared to the statistical uncertainties. In addition, all the dominant sources of systematic uncertainty can all be reduced with larger datasets.

For F_L and $A_{\rm FB}$, the largest source of systematic uncertainty comes from the data-simulation comparison of the pion momenta. It constitutes up to 30% of the statistical uncertainty on F_L and 20% of the statistical uncertainty on $A_{\rm FB}$. For S_5 and A_5, the largest source of systematic uncertainty comes from the choice of polynomial order for the angular acceptance. For the remaining CP-averaged and CP-asymmetric observables, the uncertainties arising from the data-simulation comparison and the acceptance are small. However, there are three other non-negligible sources of systematic uncertainty. Throughout the full q^2 range,

peaking backgrounds introduce a systematic uncertainty up to 0.01. For the likelihood fit of the angular observables in the first two q^2 bins (where the acceptance changes most rapidly), the uncertainty arising from using the bin centre, as opposed to a bin edge, is at the level of 0.01 or less. Finally, at high q^2, the statistical precision on the acceptance correction leads to a systematic uncertainty up to 0.01.

For the P_i' observables, the situation is more complex and the systematic uncertainty is shared more evenly between the different sources (see Table 3.6.1).

Propagating the above sources of systematic uncertainty to the zero-crossing points yields uncertainties at the level of 0.07 GeV$^2/c^4$ for S_4, 0.02 GeV$^2/c^4$ for S_5, and 0.03 GeV$^2/c^4$ for $A_{\rm FB}$.

Source	F_L	S_3–S_9	A_3–A_9	P_1–P_8'	q_0^2 GeV$^2/c^4$
Acceptance stat. uncertainty	< 0.01	< 0.01	< 0.01	< 0.01	0.01
Acceptance polynomial order	< 0.01	< 0.02	< 0.02	< 0.04	0.01–0.03
Data-simulation differences	0.01–0.02	< 0.01	< 0.01	< 0.01	< 0.02
Acceptance variation with q^2	< 0.01	< 0.01	< 0.01	< 0.01	–
$m(K^+\pi^-)$ model	< 0.01	< 0.01	< 0.01	< 0.03	< 0.01
Background model	< 0.01	< 0.01	< 0.01	< 0.02	0.01–0.05
Peaking backgrounds	< 0.01	< 0.01	< 0.01	< 0.01	0.01–0.04
$m(K^+\pi^-\mu^+\mu^-)$ model	< 0.01	< 0.01	< 0.01	< 0.02	< 0.01
Det. and prod. asymmetries	–	–	< 0.01	< 0.02	–

Table 3.6.1: Summary of the different sources of systematic uncertainty on the angular observables. Upper limits or typical ranges are quoted for the different groups of observables. The column labelled q_0^2 corresponds to the zero-crossing points of S_4, S_5 and $A_{\rm FB}$.

3.7 Results

Results for the likelihood fit and the method of moments

The CP-averaged observables obtained from the likelihood fits are shown together with the SM predictions in Figure 3.7.2. The CP asymmetries are shown in Figure 3.7.3. The SM predictions are based on the prescription of Ref. [65] and provided in the regions $0.1 < q^2 < 6.0$ GeV$^2/c^4$ and $15.0 < q^2 < 19.0$ GeV$^2/c^4$. No predictions are made for the region close to the narrow charmonium resonances, the J/ψ and $\psi(2S)$, where many assumptions used are no longer valid. No predictions are provided in [65] for S_7, S_8, S_9, or the A_i observables, which are expected to be close to zero in the SM.

The results of the fits for the optimised angular observables are shown with their SM predictions in Figure 3.7.4. For the P_i' observables, predictions from Ref. [66] are shown, restricted to the range $q^2 < 8.0$ GeV$^2/c^4$. The variation in the uncertainties on the P_i'

observables arises from their dependence on F_L. When F_L is large, the $(1 - F_L)$ term in the observable definitions gives rise to a larger and potentially asymmetric uncertainty.

The values of F_S obtained from the fits are consistent with an S-wave contribution of approximately 5%, as observed in $B^0 \to J/\psi K^{*0}$ decays [52–54].

The full results of the likelihood fits for the angular observables, including correlations among the observables, are reported in the paper. In general, the correlations are small. Notable exceptions include the correlation between $A_{\rm FB}$ and F_L, which can be as large as 60%, and correlations between different P_i' observables in the range $2.5 < q^2 < 4.0$ GeV$^2/c^4$. The correlation between $A_{\rm FB}$ and F_L arises from the requirement that the differential decay rate remains positive over the entire phase space. The P_i' correlations originate from their shared dependence on F_L.

Considering the observables individually, most results are largely in agreement with the SM predictions, the main exception being the observable S_5 and the related observable P_5'. The discrepancy in P_5' confirms the result from the previous LHCb analysis [67]. In this analysis, the deviation from the SM prediction is observed in the $4.0 < q^2 < 6.0$ GeV$^2/c^4$ and $6.0 < q^2 < 8.0$ GeV$^2/c^4$ bins at the level of 2.8 and 3.0 standard deviations, respectively. Small deviations are also seen in the measured $A_{\rm FB}$ distribution, where the data systematically lie below the SM prediction in the range $1.1 < q^2 < 6.0$ GeV$^2/c^4$. No significant CP asymmetries are observed.

The differences between the central values obtained using the likelihood fit and the method of moments, when using the same binning scheme, are compatible with expectations from pseudoexperiments. Figure 3.7.5 provides on the left a comparison of the results for P_5' with the likelihood approach and the method of moments. The observable S_{6c}, which can only be calculated with the method of moments, is shown on the right plot and is found to be consistent with zero, as expected in the SM.

The level of compatibility of the measurements with the SM is evaluated using the EOS software package [68], which provides the SM predictions. A χ^2 fit is performed using the CP-averaged observables and assuming that NP would only affect the real part of the C_9 Wilson coefficient. The minimization leads to a shift $\Delta Re(C_9) = -1.04 \pm 0.25$ from the SM value of $Re(C_9) = 4.27$, therefore indicating a tension with the SM at the level of 3.4 standard deviations. This tension is and has been widely discussed in the field, as it could be caused by unexpectedly large hadronic effects or by a new vector particle.

Amplitude fit results

The observables S_4, S_5, and $A_{\rm FB}$ as obtained from the fit to the q^2-dependent decay amplitudes are shown on figure 3.7.1. The results are in agreement with those obtained from both the likelihood fit of the angular observables and the moment analysis. For $A_{\rm FB}$, the best fit to the data, represented by the curve in the figure, exhibits two zero-crossing points in the range $1.1 < q^2 < 6.0$ GeV$^2/c^4$, with different slopes. Only the solution consistent with the data for $q^2 > 6.0$ GeV$^2/c^4$ is quoted, i.e. the solution with positive slope. The zero-crossing points

are measured to be:

$$q_0^2(S_5) \in [2.49,\ 3.95]\ \text{GeV}^2/c^4 \text{ at } 68\% \text{ C.L.},$$
$$q_0^2(A_{\text{FB}}) \in [3.40,\ 4.87]\ \text{GeV}^2/c^4 \text{ at } 68\% \text{ C.L.},$$
$$q_0^2(S_4) < 2.65\ \text{GeV}^2/c^4 \quad \text{at } 95\% \text{ C.L.}$$

The correlations between the measured values of the observables are found to be below 10%. The measured zero-crossing points are consistent with SM expectations. For example, SM predictions for $q_0^2(A_{\text{FB}})$ typically lie in the range 3.9–4.4 GeV^2/c^4 [13,69,70], with relative uncertainties below the 10% level.

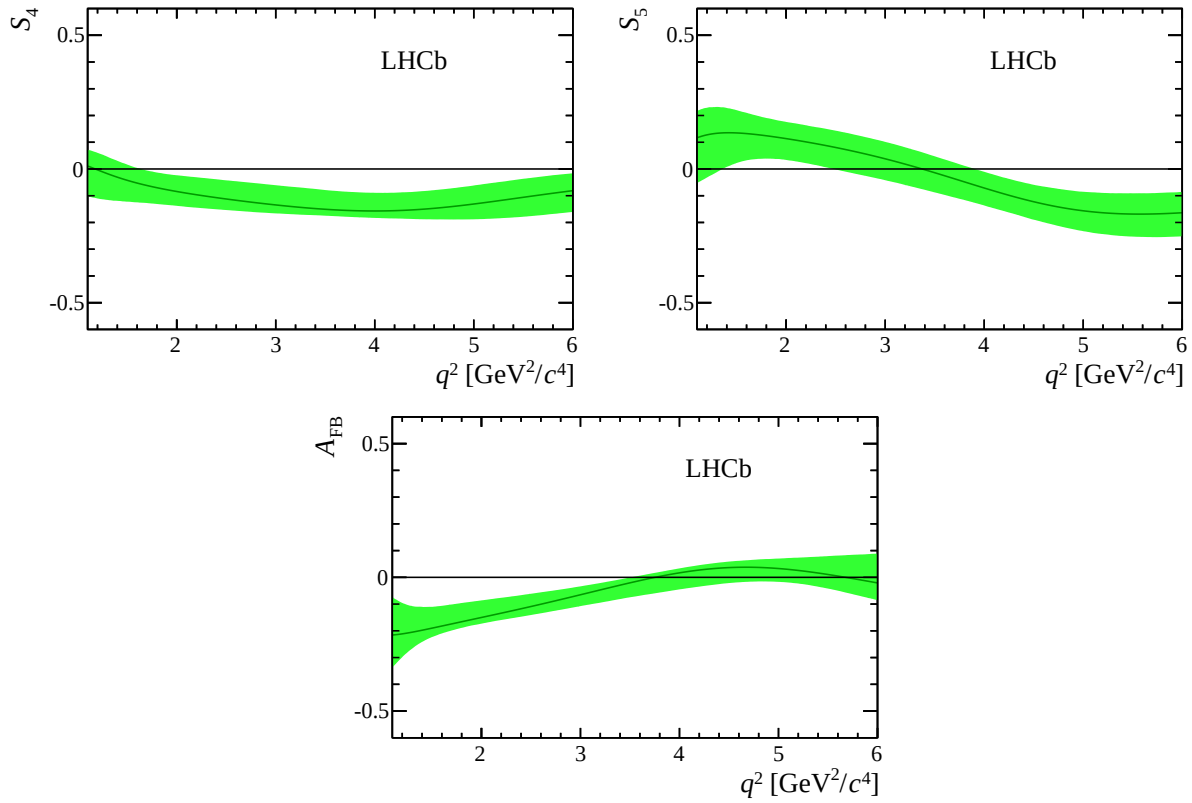

Figure 3.7.1: The observables S_4, S_5 and A_{FB} determined by fitting for the q^2 dependent decay amplitudes. The line indicates the best-fit to the dataset. The band indicates the 68% interval on the bootstraps at each point in q^2. Note that, the correlation between points in the bands means it is not possible to extract the uncertainty on the zero-crossing points from these figures.

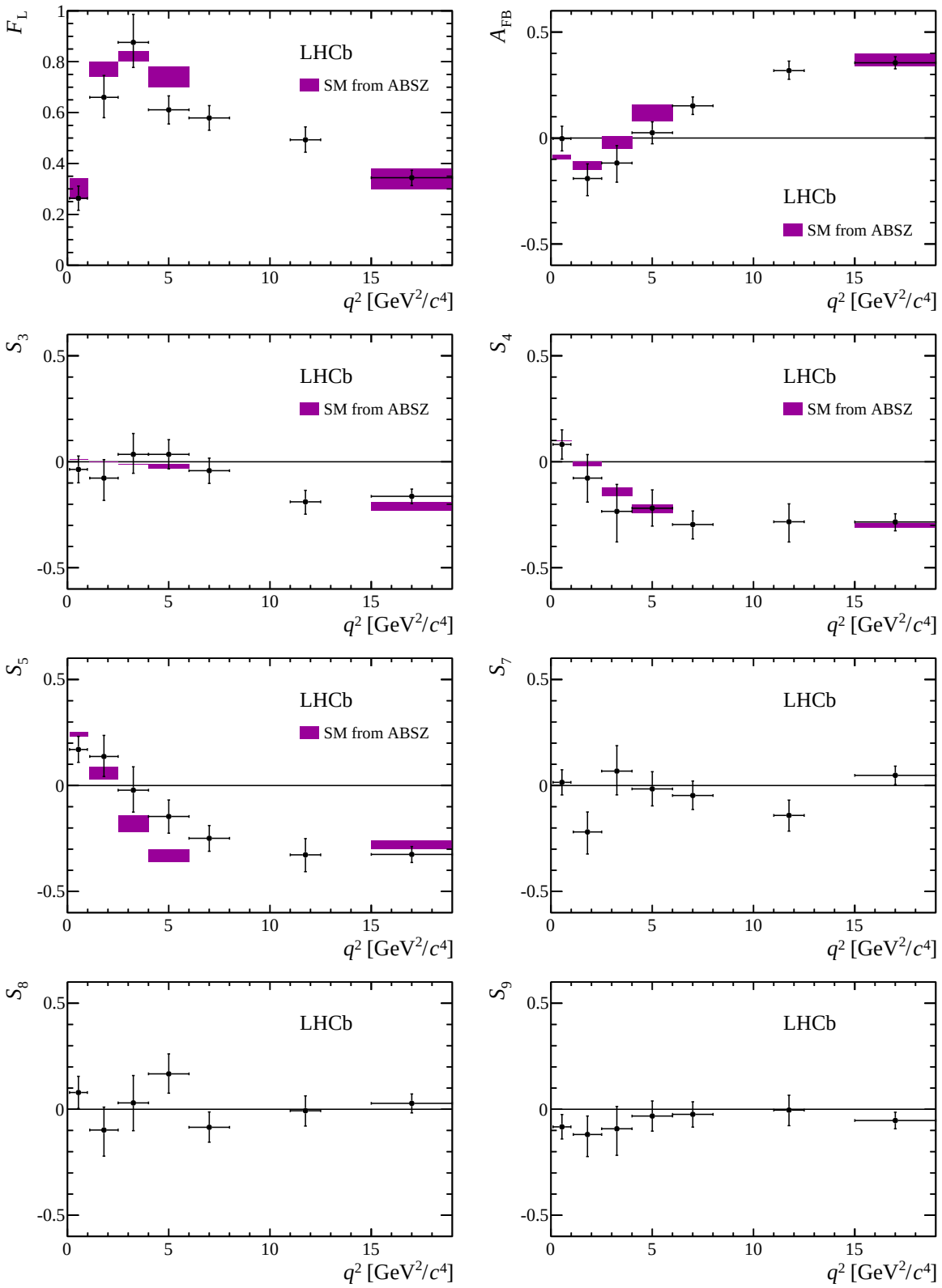

Figure 3.7.2: The *CP*-averaged observables in bins of q^2, determined from a maximum likelihood fit to the data. The shaded boxes show the SM predictions based on the prescription of Ref. [65].

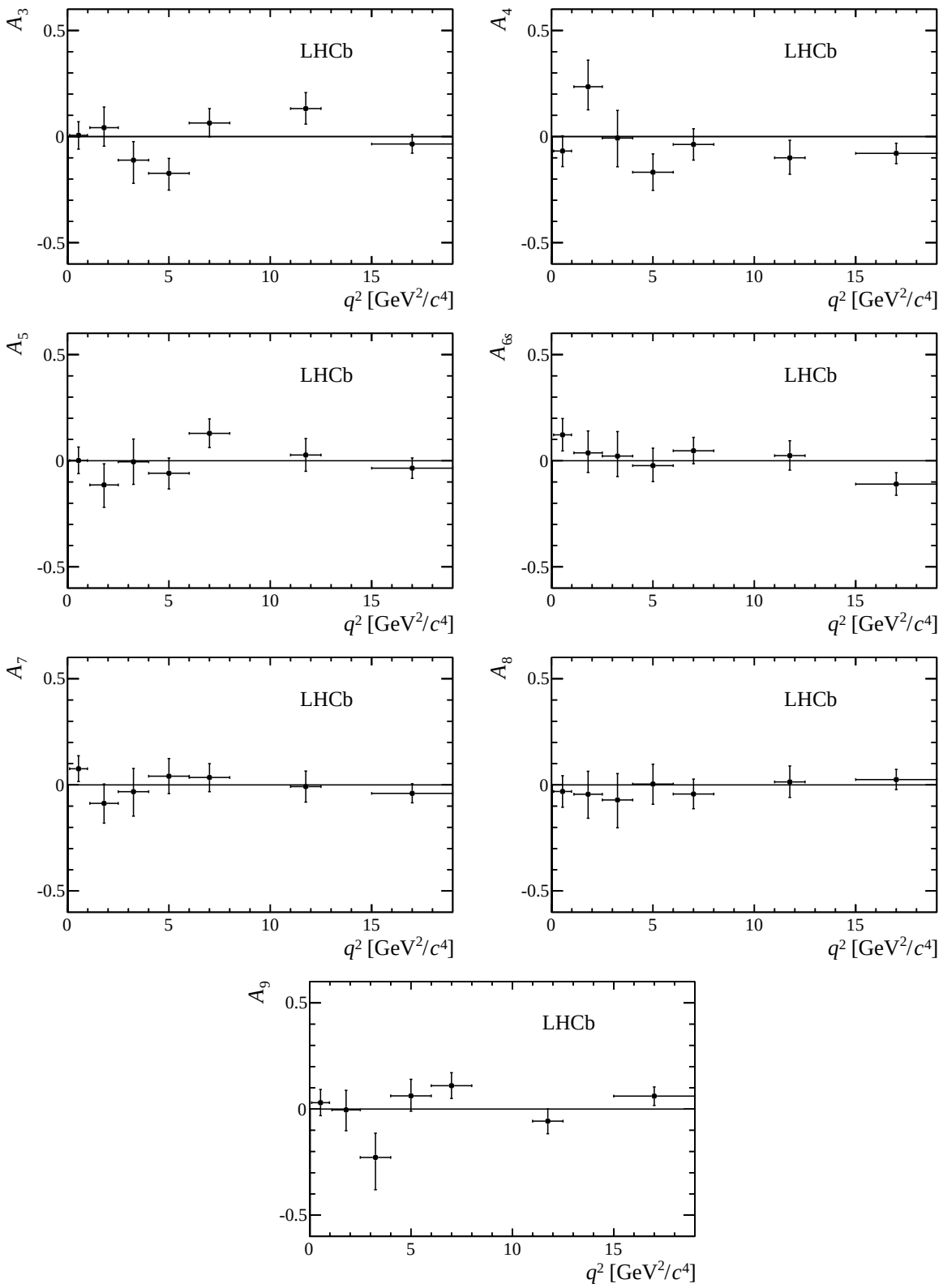

Figure 3.7.3: The *CP*-asymmetric observables in bins of q^2, determined from a maximum likelihood fit to the data.

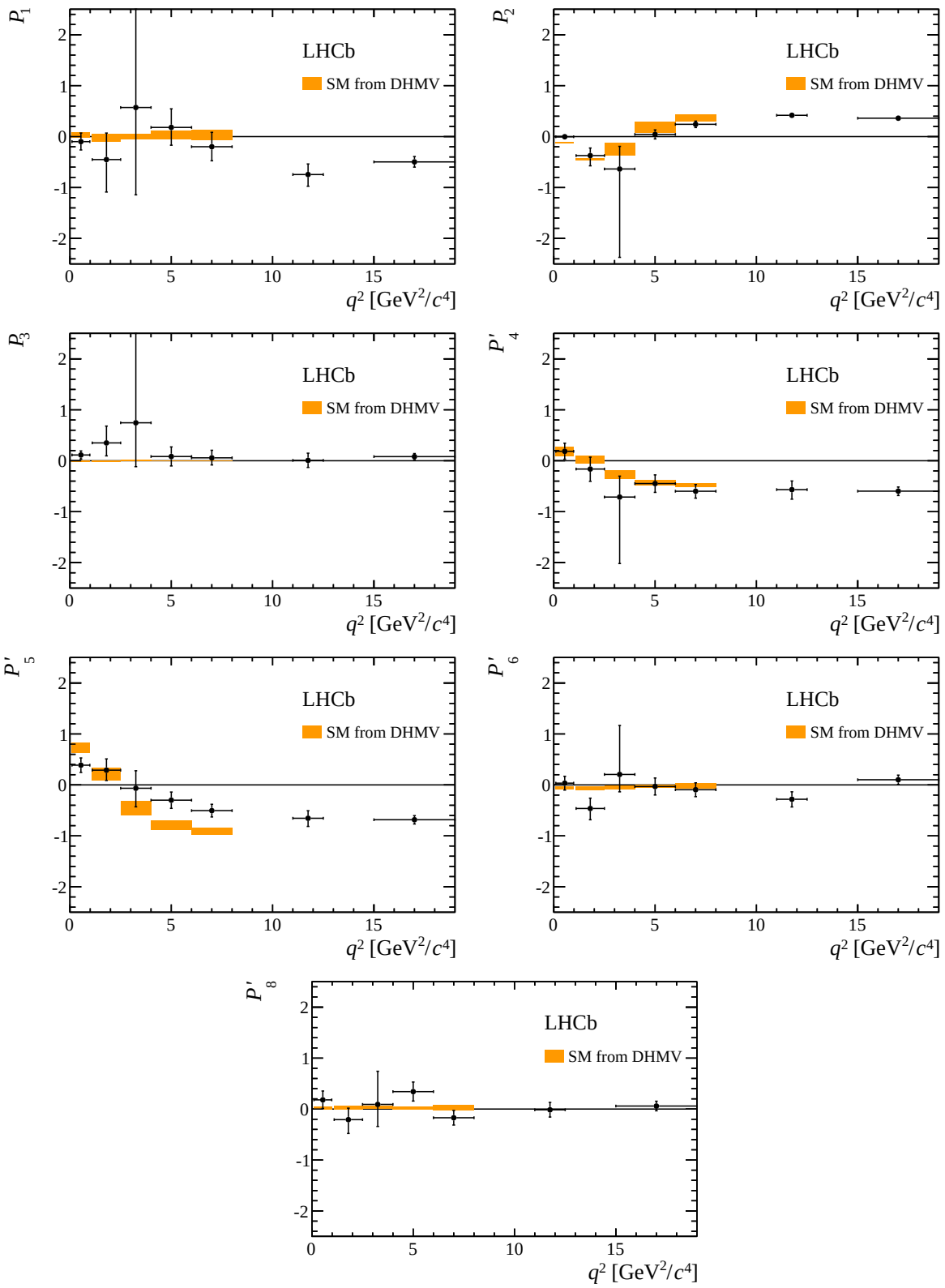

Figure 3.7.4: The optimised angular observables in bins of q^2, determined from a maximum likelihood fit to the data. The shaded boxes show the SM prediction taken from Ref. [66].

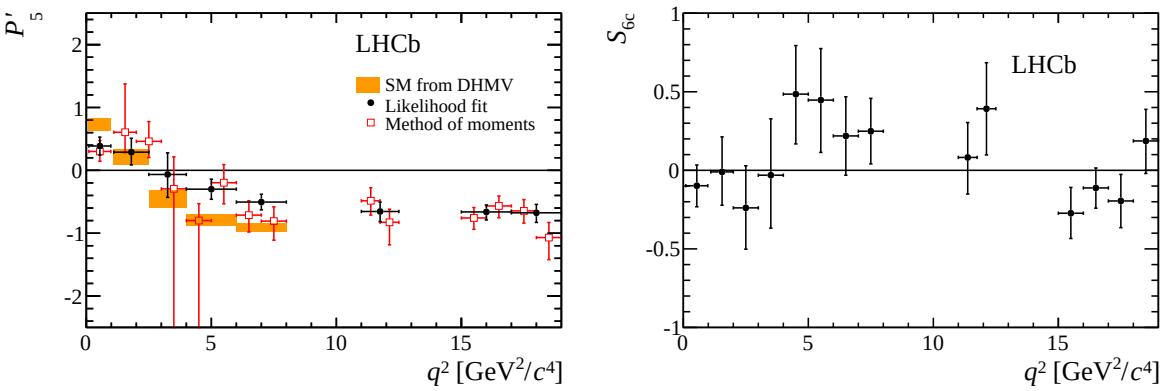

Figure 3.7.5: Left: the optimised angular observable P'_5 in bins of q^2, determined from a maximum likelihood fit to the data and the method of moments. Right: the observable S_{6c} in bins of q^2, as determined from a moment analysis of the data.

Chapter 4

Lepton Universality Test $R_{K^{*0}}$

In 2017, LHCb had already published angular and branching fraction measurements of $b \to s\ell\ell$ decays with muons in the final state, indicating tensions with the SM. There was wide discussion about possible hadronic contributions affecting these measurements and potentially faking new physics effects. The lepton flavor universality test, in this respect, are clean measurements because the hadronic uncertainties cancel in the ratio. A first LHCb measurement of R_K in the q^2 range between 1.0 and 6.0 GeV^2/c^4 in 2014 [71] was compatible with the SM at 2.6 standard deviations. With an increasing datased, $b \to s\ell\ell$ transitions with electrons in the final state where becoming accessible and it was important to have a lepton flavor universality test in a complementary channel. Therefore, we performed the first LHCb measurement of $R_{K^{*0}}$ [2], discussed in this chapter, based on pp collision data collected with the LHCb detector at centre-of-mass energies of 7 and 8 TeV during 2011 and 2012, and corresponding to an integrated luminosity of about $3\,\mathrm{fb}^{-1}$. The measurement used $B^0 \to K^{*0}\ell^+\ell^-$ decays and developed a number of techniques which were used in later analyses. The results showed compatibility with the SM at the level of about 2.5 standard deviations. The most recent analysis of these decays, profiting of a larger datasample, confirmed the compatibility with the SM with the current level of precision of these measurements. The lepton flavor universality tests still stands as one of the most promising and theoretical clean approaches to probe NP via FCNC.

4.1 Analysis strategy

The first LHCb measurement of $R_{K^{*0}}$ is based on pp collision data collected with the LHCb detector at centre-of-mass energies of 7 and 8 TeV during 2011 and 2012, and corresponding to an integrated luminosity of about $3\,\mathrm{fb}^{-1}$, using $B^0 \to K^{*0}\ell^+\ell^-$ decays with ℓ representing a muon or an electron. The K^{*0} represents a $K^*(892)^0$ meson, reconstructed in the $K^+\pi^-$ final state by selecting candidates within $100\,\mathrm{MeV}/c^2$ of the known mass [72]. No attempt is made to separate the K^{*0} meson from S-wave or other broad contributions present in the selected $K^+\pi^-$ region, since the S-wave fraction contribution to the $B^0 \to K^{*0}\mu^+\mu^-$ mode has been measured to be small [73], as already discussed in the previous chapter. The analysis is performed in two regions of q^2 that are sensitive to different NP contributions: a central-q^2

bin, between 1.1 and $6.0\,\mathrm{GeV}^2/c^4$, dominated by the penguin diagram with emission of a Z boson; and a low-q^2 bin, between 0.045 and $1.1\,\mathrm{GeV}^2/c^4$, where the contribution of the penguin diagram with emission of a virtual photon is also present. The lower boundary of the low-q^2 region corresponds roughly to the dimuon kinematic threshold. Instead, the boundary at $1.1\,\mathrm{GeV}^2/c^4$ is chosen such that $\phi(1020) \to \ell^+\ell^-$ decays, which could potentially dilute NP effects, are included in the low-q^2 interval. Finally, the upper boundary of the central-q^2 bin at $6.0\,\mathrm{GeV}^2/c^4$ is chosen to reduce contamination from the radiative tail of the J/ψ resonance.

The measurement is performed as a double ratio of the branching fractions of the $B^0 \to K^{*0}\ell^+\ell^-$ and $B^0 \to K^{*0}J/\psi(\to \ell^+\ell^-)$ decays

$$R_{K^{*0}} = \frac{\mathcal{B}(B^0 \to K^{*0}\mu^+\mu^-)}{\mathcal{B}(B^0 \to K^{*0}J/\psi(\to \mu^+\mu^-))} \Big/ \frac{\mathcal{B}(B^0 \to K^{*0}e^+e^-)}{\mathcal{B}(B^0 \to K^{*0}J/\psi(\to e^+e^-))} \,,$$

where the two channels are also referred to as the "nonresonant" and the "resonant" modes, respectively. In general, the branching fraction of a decay is measured as follows:

$$\mathcal{B} = \frac{Y}{\mathcal{L}\sigma\varepsilon}$$

where Y indicates the measured yields, $\mathcal{L}$ the integrated luminosity of the data sample, σ the production cross section and ε the reconstruction efficiency. Given that $\mathcal{L}$ and σ are the same for all $\mathcal{B}$ in the ratios, they cancel between numerators and denominators and the only experimental quantities relevant for the measurement are the yields and the reconstruction efficiencies of the four decays. The advantage of using a double ratio is that, due to the similarity between the experimental efficiencies of the nonresonant and resonant decay modes, many sources of systematic uncertainty are substantially reduced. This helps to mitigate the significant differences in reconstruction between decays with muons or electrons in the final state, mostly due to bremsstrahlung emission and the trigger response. The decay $J/\psi \to \ell^+\ell^-$ is measured to be consistent with LU [72], therefore any observed deviation from the lepton flavor universality would come from the rare modes. To avoid experimental biases, the analysis is performed using a blind approach.

Final state radiation (FSR), i.e. emission of photons from at least one of the leptons, could bias the measurement in case the radiative photon would not be reconstructed as part of the lepton cluster. This would provoke a wrong evaluation of the q^2 value and a possible migration of events among the bins. To avoid such cases, the measurement is corrected for final-state radiation (FSR).

The resolution on the reconstructed invariant mass of the B^0 and the background composition depends on the kinematics of the decay, as well as on the trigger category. For this reason, simultaneous fits to the four-body invariant mass of the $B^0 \to K^{*0}J/\psi(\to e^+e^-)$ and $B^0 \to K^{*0}e^+e^-$ channels are performed separately in the three trigger categories: LOE, LOH, LOI, defined in 2.4.

The $K^+\pi^-e^+e^-$ signal PDF is observed to depend on the number of calorimeter clusters that are added to the dielectron candidate in order to compensate for bremsstrahlung. Following the strategy of Ref. [71], three bremsstrahlung categories are considered, depending on whether zero, one or more clusters are recovered.

4.2 Corrections to the simulation

In order to optimise the selection criteria and accurately evaluate the efficiencies, a set of corrections, listed below, is determined from unbiased control samples selected from the data. The procedure is applied to the simulated samples of the nonresonant and resonant modes.

- Particle identification (PID) performance [30]. The PID efficiencies are measured using a tag-and-probe method on high-purity data samples of $D^{*+} \to D^0(\to K^-\pi^+)\pi^+$ decays for pions and kaons and $B^+ \to K^+ J/\psi(\to \ell\ell)$ decays for electrons and muons. Corrections are determined as a function of the track momentum and pseudorapidity.

- Charged-track multiplicity in the event and B^0 kinematics. Resonant $B^0 \to K^{*0} J/\psi(\to \mu^+\mu^-)$ decays are used, since the muon triggers are observed to be well modelled in simulation.

- Hardware and software trigger response. A tag-and-probe technique using $B^0 \to K^{*0} J/\psi(\to \mu^+\mu^-)$ and $B^0 \to K^{*0} J/\psi(\to e^+e^-)$ decays is used. The tag sample is defined by events where the hardware trigger is fired by activity in the event not associated with any of the signal decay particles. Alternatively, when probing the leptonic (hadronic) hardware triggers, the tag is required to have triggered the hadronic (leptonic) hardware trigger. The corrections for the leptonic hardware triggers are parameterised as a function of the cluster $E_{\rm T}$ or track $p_{\rm T}$. The hadron hardware trigger efficiency is known to be sensitive to tracks overlapping in the HCAL, however, a good description can be obtained when the efficiency is measured as a function of the $p_{\rm T}$ of the $K^+\pi^-$ pair instead of the kaon or the pion independently. Corrections are determined separately in the different calorimeter regions [74], in order to take into account potential differences due to different occupancies. When the hardware trigger is fired by activity in the event not associated with any of the signal decay particles, the correction is determined as a function of the B^0 $p_{\rm T}$ and the charged-track multiplicity in the event in order to take into account correlations in the production between the two b hadrons in the event. For the software trigger, the corrections are determined as a function of the minimum $p_{\rm T}$ of the B^0 decay products.

- Reconstruction performance. This is based on $B^0 \to K^{*0} J/\psi(\to \ell^+\ell^-)$ candidates, to which the full selection is applied as well as additional requirements to further reduce the background contamination. The corrections are determined by matching the distribution of the B^0 kinematics and vertex fit quality in simulation to the data, separately for muon and electron samples.

The correction factors are determined sequentially as histograms, with the previous corrections applied before deriving the subsequent one. To avoid biases in the procedure due to common candidates being used for both the determination of the corrections and the measurement, a k-folding [46] approach with $k = 10$ is adopted. To dilute the dependence on the choice of the binning schemes, all corrections are linearly interpolated between adjacent bins. After all the corrections are applied to the simulation, a very good agreement with the data is obtained.

4.3 Efficiency ratios in $R_{K^{*0}}$

The efficiency for selecting each decay mode is defined as the product of the efficiencies of the geometrical acceptance of the detector, the complete reconstruction of all tracks, the trigger requirements and the full set of kinematic, PID and background rejection requirements. All efficiencies are determined using simulation that is tuned to data, as described in section 4.2, and account for bin migration in q^2 due to resolution, FSR and bremsstrahlung in the detector. The net bin migration amounts to about 1% and 5% in the low- and central-q^2 regions, respectively.

The efficiency ratios between the nonresonant and the resonant modes, $\varepsilon_{\ell^+\ell^-}/\varepsilon_{J/\psi(\ell^+\ell^-)}$, which directly enter in the $R_{K^{*0}}$ measurement, are reported in table 4.3.1. Besides a dependence on the kinematics, the difference between the ratios in the two q^2 regions is almost entirely due to the different requirement on the neural-network classifier. Using simulation, it is checked that the relative fraction of the electron trigger categories depend on q^2 as expected: the fraction of L0E decreases when decreasing in q^2, while L0H increases; on the other hand, the fraction of L0I only mildly depends on q^2.

Table 4.3.1: Efficiency ratios between the nonresonant and resonant modes, $\varepsilon_{\ell^+\ell^-}/\varepsilon_{J/\psi(\ell^+\ell^-)}$, for the muon and electron (in the three trigger categories) channels. The uncertainties are statistical only.

	$\varepsilon_{\ell^+\ell^-}/\varepsilon_{J/\psi(\ell^+\ell^-)}$	
	low-q^2	central-q^2
$\mu^+\mu^-$	0.679 ± 0.009	0.584 ± 0.006
e^+e^- (L0E)	0.539 ± 0.013	0.522 ± 0.010
e^+e^- (L0H)	2.252 ± 0.098	1.627 ± 0.066
e^+e^- (L0I)	0.789 ± 0.029	0.595 ± 0.020

4.4 Fits to the invariant mass distributions

$R_{K^{*0}}$ is determined by a simultaneous unbinned extended maximum likelihood fit to the four-body invariant mass $m(K^+\pi^-\ell^+\ell^-)$ of the selected candidates for the nonresonant and resonant modes and for each lepton type in each q^2 interval, with common parameters shared. The reconstructed invariant mass is calculated using a kinematic fit with a constraint on the vertex that requires the B^0 candidate to originate from the PV.

Muonic channels

For the muonic channels the invariant mass window for the fit is 5150–5850 MeV/c^2. The low edge is chosen to reject the partially reconstructed background that populates the low mass region.

For the signal, the probability density function is defined by a Hypatia function [75], where the parameters are fixed from simulation. However, in order to account for possible residual discrepancies with data, the mean and width are allowed to vary freely in the fit, independently for the resonant and nonresonant modes and in each q^2 region.

The combinatorial background is parameterised using an exponential function, with a different slope in the resonant and nonresonant modes, and in each q^2 region, free to vary in the fit.

For the resonant mode, two additional sources of background are included: $\overline{\Lambda}_b^0 \to K^+\overline{p}J/\psi(\to \mu^+\mu^-)$ decays, where the $\overline{p}$ candidate is misidentified as a π^- meson, and $\overline{B}_s^0 \to K^{*0}J/\psi(\to \mu^+\mu^-)$ decays. The former are described using a kernel estimation technique [76] applied to simulated events for which the $K^+\pi^-$ invariant mass distribution has been matched to data from Ref. [77]. The latter are modelled using the same PDF as for the signal, but with the mean value shifted by the known difference between the B^0 and the B_s^0 masses. The equivalent backgrounds to the nonresonant mode are found to be negligible.

Electronic channels

For the electronic channels, due to the limited resolution on the $K^+\pi^-e^+e^-$ invariant mass, a wider window of 4500–6200 MeV/c^2 is used. The signal PDF is described by the sum of a Crystal Ball function [78] (CB) and a wide Gaussian function. The CB function accounts for FSR and bremsstrahlung that is not fully recovered, and corresponds to over 90% of the total signal PDF. Cases where bremsstrahlung clusters were incorrectly associated are accounted for by the Gaussian function. The shape parameters and the fraction of candidates in each bremsstrahlung category are taken from simulation, the latter having been checked to be well represented by using data control channels. In order to account for possible data-simulation discrepancies, the mean (width) of the PDF for each trigger category is allowed to shift (scale). These shift (scale) factors are common between the nonresonant and resonant PDFs. An additional scale factor is applied to the parameter describing the tail of the CB functions.

The combinatorial background is described by an exponential function with different slope parameters, free to vary in the fit, for the resonant and nonresonant modes, and in each trigger category and q^2 region.

The shape of the partially reconstructed hadronic background, $B \to X(\to YK^{*0})e^+e^-$ (where the decay product Y is not reconstructed), is obtained from simulation using a sample that includes decays of higher kaon resonances, X, such as $K_1^+(1270)$ and $K_2^{*+}(1430)$. The mass distribution is modelled using a kernel estimation technique separately in each trigger category and q^2 region. The fraction of this background is free to vary in both q^2 intervals. Due to the requirement of a J/ψ mass constraint when calculating the four-body invariant mass, there is no partially reconstructed background left to contaminate $B^0 \to K^{*0}J/\psi(\to e^+e^-)$ candidates.

The long radiative tail of the dielectron invariant mass implies that $B^0 \to K^{*0}J/\psi(\to e^+e^-)$ decays can contaminate the central-q^2 region and therefore an additional background component has to be considered (see figure 2.6.1). However, this contribution does not peak at the nominal B^0 mass. The distribution is modelled using simulated events, while the

Table 4.5.1: Systematic uncertainties on the $R_{K^{*0}}$ ratio for the three trigger categories separately (in percent). The total uncertainty is the sum in quadrature of all the contributions.

	$\Delta R_{K^{*0}}/R_{K^{*0}}$ [%]					
	low-q^2			central-q^2		
Trigger category	L0E	L0H	L0I	L0E	L0H	L0I
Corrections to simulation	2.5	4.8	3.9	2.2	4.2	3.4
Trigger	0.1	1.2	0.1	0.2	0.8	0.2
PID	0.2	0.4	0.3	0.2	1.0	0.5
Kinematic selection	2.1	2.1	2.1	2.1	2.1	2.1
Residual background	–	–	–	5.0	5.0	5.0
Mass fits	1.4	2.1	2.5	2.0	0.9	1.0
Bin migration	1.0	1.0	1.0	1.6	1.6	1.6
$r_{J/\psi}$ ratio	1.6	1.4	1.7	0.7	2.1	0.7
Total	4.0	6.1	5.5	6.4	7.5	6.7

normalisation is constrained using a mixture of data and simulation.

The contributions to the resonant modes from $\overline{\Lambda}_b^0 \to K^+\overline{p}J/\psi(\to e^+e^-)$ and $\overline{B}_s^0 \to K^{*0}J/\psi(\to e^+e^-)$ decays are treated following the same procedure as for the muon channel. The normalisations are fixed to the yields returned by the muon fit after correcting for efficiency differences between the two final states.

4.5 Systematic uncertainties

Since $R_{K^{*0}}$ is measured as a double ratio, many potential sources of systematic uncertainty cancel between the rare and resonant modes. The remaining systematics uncertainties are related to residual effect in the efficiencies ratios determination due to the slightly different phase space of the rare and resonant mode, to the fit parameterizations and to effects of event migration due to electron bremssthrahlung. Their effects on $R_{K^{*0}}$ are summarised in table 4.5.1 and are described below. All the uncertainties are treated as uncorrelated among the trigger categories, except for those related to particle identification, to the kinematic selection criteria, to the residual background, to the fit to the invariant mass and to bin migration.

Corrections to simulation

The uncertainty induced by the limited size of the simulated sample used to compute the efficiencies is taken into account. An additional systematic uncertainty is determined using

binned corrections instead of interpolated ones. Finally, since the data samples used to determine the corrections have a limited size, particularly for the electron hardware trigger, a systematic uncertainty is assessed with a bootstrapping technique [79].

Trigger efficiency

For the hardware triggers, the corrections to the simulation are determined using different control samples and the change in the result is assigned as a systematic uncertainty. For the software trigger, the corrections to the simulation do not show dependences on the kinematic of the decays, and therefore only the statistical uncertainty on the overall correction is considered as a systematic uncertainty.

Particle identification

The particle identification response is calibrated using data control samples. A systematic uncertainty due to the procedure and kinematic differences between the control samples and the signal modes is included. The effects due to the identification of leptons and hadrons are also considered. Discrepancies in the description of the latter are small and further cancel in the double ratio.

Kinematic selection

A systematic uncertainty due to the choice of the mass fit range and to the two-dimensional requirement on χ^2_{VD} and m_{corr} (see section 2.5) is determined by comparing the efficiencies in simulation and background-subtracted samples of $B^0 \to K^{*0} J/\psi(\to \mu^+\mu^-)$ or $B^0 \to K^{*0} J/\psi(\to e^+e^-)$ decays.

Residual background

Background due to $B^0 \to K^{*0} J/\psi(\to e^+e^-)$ decays, where one of the hadrons is misidentified as an electron and vice versa, is studied using simulation and is estimated to be small. However, a few candidates with one electron of the dilepton pair having a low probability to be genuine are observed in background subtracted data. Therefore, a systematic uncertainty is assigned based on the distribution of the PID information of these candidates.

Mass fit

The systematic uncertainty due to the parameterisation of the signal invariant mass distributions is found to be negligible for the muon channel. For the electron channel, the signal PDF is changed from the sum of a CB and a Gaussian function to the sum of two CB functions, where the mean parameter is shared and, additionally, the mass shift and the width scale factors are constrained using the $B^0 \to K^{*0}\gamma(\to e^+e^-)$ decay mode instead of $B^0 \to K^{*0} J/\psi(\to e^+e^-)$. The relative fractions of the three bremsstrahlung categories are measured in data using $B^0 \to K^{*0} J/\psi(\to e^+e^-)$ and the observed differences with respect to simulation are used in the mass fit. For the backgrounds, a component that describes

candidates where the hadron identities are swapped is added both to the muon and electron $B^0 \to K^{*0} J/\psi(\to \ell^+\ell^-)$ modes, and constrained to the expected values observed in simulation. The kernel of the nonparametric models is also varied, as well as the mixture of the $K_1^+(1270)$ and $K_2^{*+}(1430)$ components that is constrained using data [80]. The contributions to the systematic uncertainty from these sources are evaluated using pseudoexperiments that are generated with modified parameters and fitted with the PDFs used to fit the data.

Bin migration

For the electron channel, the degraded q^2 resolution due to bremsstrahlung emission causes a nonnegligible fraction of signal candidates to migrate in and out of the given q^2 bin. The effect is included in the efficiency determination, but introduces a small dependence on the shape of the differential branching fraction that no longer perfectly cancels in the ratio to the muon channel. Pseudoexperiments are generated, where the parameters modelling the $d\Gamma(B^0 \to K^{*0} e^+e^-)/dq^2$ distribution are varied within their uncertainties [81]. The maximum spread of the variation in $R_{K^{*0}}$ is taken as a systematic uncertainty. Furthermore, the q^2 resolution is smeared for differences between data and simulation that are observed in the resonant mode.

$r_{J/\psi}$ ratio

The ratio of the efficiency-corrected yield of the resonant modes (see section 4.6) is expected to be unity to a very high precision. Deviations from unity are therefore considered to be a sign of residual imperfections in the evaluation of the efficiencies. The $r_{J/\psi}$ ratio is studied as a function of various event and kinematic properties of the decay products, and the observed residual deviations from unity are used to assign a systematic uncertainty on $R_{K^{*0}}$.

4.6 Cross-checks

A large number of cross-checks were performed before unblinding the result.

- The control of the absolute scale of the efficiencies is tested by measuring the ratio of the branching fractions of the muon and electron resonant channels

$$r_{J/\psi} = \frac{\mathcal{B}(B^0 \to K^{*0} J/\psi(\to \mu^+\mu^-))}{\mathcal{B}(B^0 \to K^{*0} J/\psi(\to e^+e^-))} ,$$

  which is expected to be equal to unity. This quantity represents an extremely stringent cross-check, as it does not benefit from the large cancellation of the experimental systematic effects provided by the double ratio. The $r_{J/\psi}$ ratio is measured to be $1.043 \pm 0.006 \pm 0.045$, where the first uncertainty is statistical and the second systematic. The same sources of systematic uncertainties as in the $R_{K^{*0}}$ measurement are considered (see section 4.5). The result, which is in good agreement with unity, is observed to be compatible with being independent of the decay kinematics, such as p_{T} and η of the B^0 candidate and final-state particles, and the charged-track multiplicity in the event.

- The extent of the cancellation of residual systematics in $R_{K^{*0}}$ is verified by measuring a double ratio, $R_{\psi(2S)}$, where $B^0 \to K^{*0}\psi(2S)(\to \ell^+\ell^-)$ decays are used in place of $B^0 \to K^{*0}\ell^+\ell^-$. The $R_{\psi(2S)}$ ratio, measured with a statistical precision of about 2%, is found to be compatible with unity within one standard deviation.

- The branching fraction of the decay $B^0 \to K^{*0}\mu^+\mu^-$ is measured and found to be in good agreement with Ref. [73]. Furthermore, the branching fraction of the $B^0 \to K^{*0}\gamma$ decay, where decays with a photon conversion are used, is determined with a statistical precision of about 7% and is observed to be in agreement with the expectation within two standard deviations. The $B^0 \to K^{*0}\gamma(\to e^+e^-)$ selection and determination of the signal yield closely follows that of the $B^0 \to K^{*0}e^+e^-$ decay.

- If no correction is made to the simulation, the ratio of the efficiencies changes by less than 5%.

- The relative population of the three bremsstrahlung categories is compared between data and simulation using both $B^0 \to K^{*0}J/\psi(\to e^+e^-)$ and $B^0 \to K^{*0}\gamma(\to e^+e^-)$ candidates to test possible q^2 dependence of the modelling. Good agreement is observed.

- The *sPlot* technique [82], where $m(K^+\pi^-\ell^+\ell^-)$ is used as the discriminating variable, is adopted to subtract statistically the background from the $B^0 \to K^{*0}\ell^+\ell^-$ selected data, and test the agreement between muons and electrons, data and simulation, checking several variables: the q^2 distributions show good agreement in both q^2 regions; a clear K^{*0} peak is visible in the $K^+\pi^-$ invariant mass distributions, and the muon and electron channels show good agreement; while the distribution of the opening angle between the two leptons in the central-q^2 region are very similar between the muon and electron channels, this is not the case at low-q^2 due to the difference in lepton masses; the distribution of the distance between the $K^+\pi^-$ and $\ell^+\ell^-$ vertices shows that the pairs of hadrons and leptons consistently originate from the same decay vertex.

4.7 Results

The results of the fits to the muon channels are shown in figure 4.7.1, while figure 4.7.2 displays the fit results for the electron channels, with the three trigger categories combined for illustration. The distribution of the normalised fit residuals of the $B^0 \to K^{*0}J/\psi(\to \mu^+\mu^-)$ mode shows an imperfect description of the combinatorial background at high mass values, although the effect on the signal yield is negligible. The resulting yields are listed in table 4.7.1.

The determination of $R_{K^{*0}}$ exploits the log-likelihoods resulting from the fits to the invariant mass distributions of the nonresonant and resonant channels in each trigger category and q^2 region. Each log-likelihood is used to construct the PDF of the true number of decays, which is used as a prior to obtain the PDF of $R_{K^{*0}}$. The true number of decays is assumed to have a uniform prior. The three electron trigger categories are combined by summing the corresponding log-likelihoods. Uncorrelated systematic uncertainties are accounted for by convolving the yield PDFs with a Gaussian distribution of appropriate width. Correlated

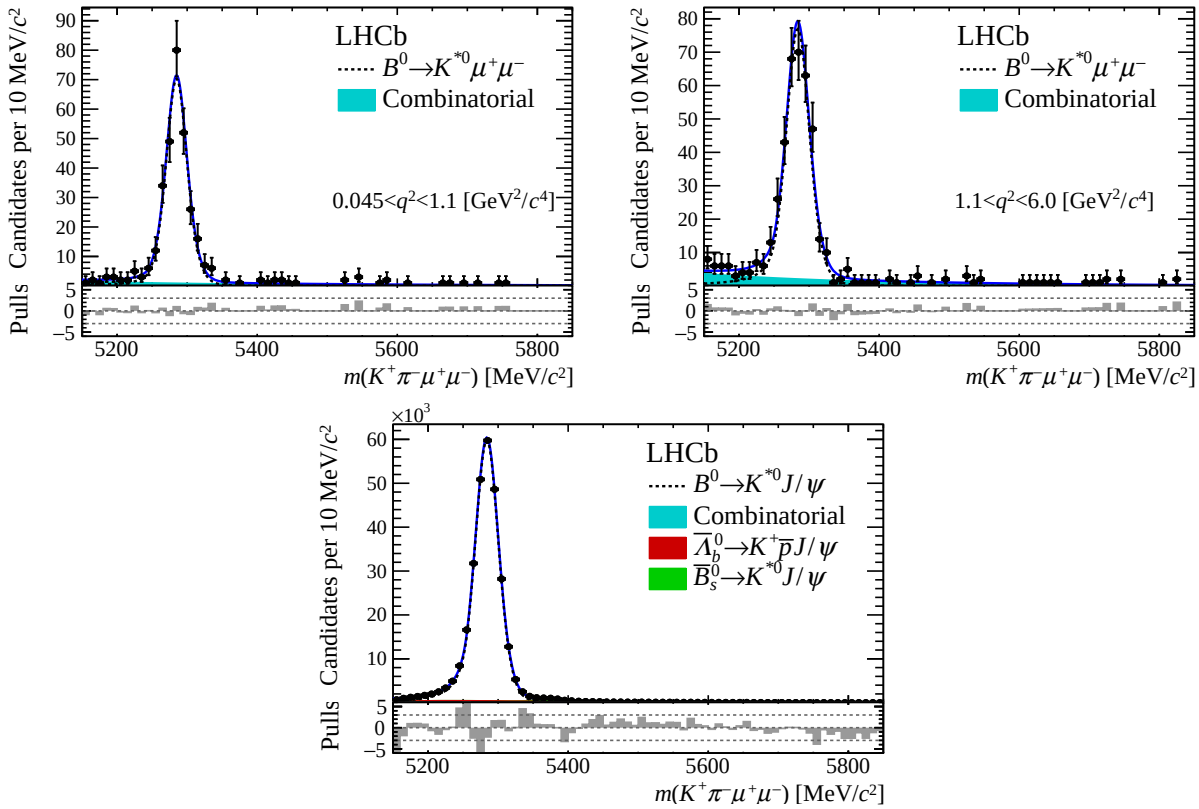

Figure 4.7.1: Fit to the $m(K^+\pi^-\mu^+\mu^-)$ invariant mass of (top) $B^0 \to K^{*0}\mu^+\mu^-$ in the low- and central-q^2 bins and (bottom) $B^0 \to K^{*0}J/\psi(\to \mu^+\mu^-)$ candidates. The dashed line is the signal PDF, the shaded shapes are the background PDFs and the solid line is the total PDF. The fit residuals normalised to the data uncertainty are shown at the bottom of each distribution.

Table 4.7.1: Yields obtained from the mass fits to the muon and electron (in the three trigger categories) channels. The uncertainties are statistical only.

	$B^0 \to K^{*0}\ell^+\ell^-$		$B^0 \to K^{*0}J/\psi(\to \ell^+\ell^-)$
	low-q^2	central-q^2	
$\mu^+\mu^-$	$285\ ^{+\ 18}_{-\ 18}$	$353\ ^{+\ 21}_{-\ 21}$	$274416\ ^{+\ 602}_{-\ 654}$
e^+e^- (L0E)	$55\ ^{+\ 9}_{-\ 8}$	$67\ ^{+\ 10}_{-\ 10}$	$43468\ ^{+\ 222}_{-\ 221}$
e^+e^- (L0H)	$13\ ^{+\ 5}_{-\ 5}$	$19\ ^{+\ 6}_{-\ 5}$	$3388\ ^{+\ 62}_{-\ 61}$
e^+e^- (L0I)	$21\ ^{+\ 5}_{-\ 4}$	$25\ ^{+\ 7}_{-\ 6}$	$11505\ ^{+\ 115}_{-\ 114}$

systematic uncertainties are treated by convolving the $R_{K^{*0}}$ PDF with a Gaussian distribution. The one, two and three standard deviation intervals are determined as the ranges that include 68.3%, 95.4% and 99.7% of the PDF. In each q^2 region, the measured values of $R_{K^{*0}}$ are

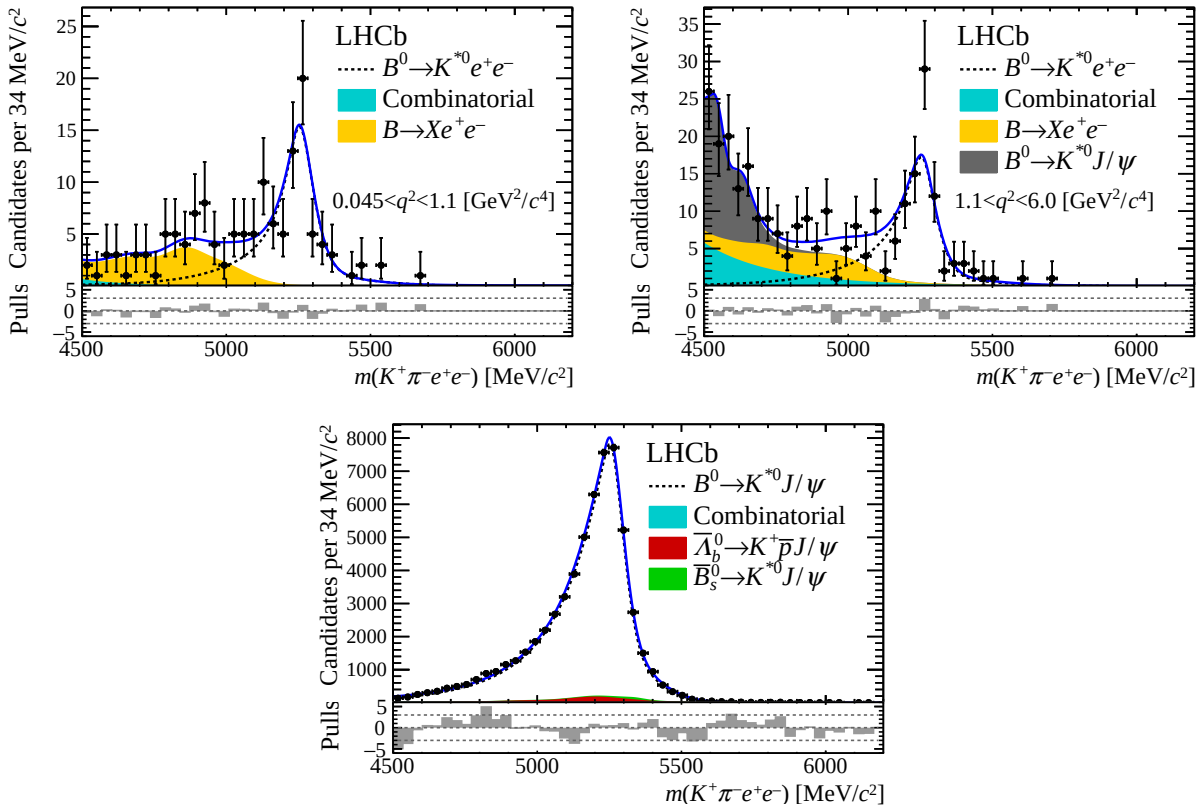

Figure 4.7.2: Fit to the $m(K^+\pi^-e^+e^-)$ invariant mass of (top) $B^0 \to K^{*0}e^+e^-$ in the low- and central-q^2 bins and (bottom) $B^0 \to K^{*0}J/\psi(\to e^+e^-)$ candidates. The dashed line is the signal PDF, the shaded shapes are the background PDFs and the solid line is the total PDF. The fit residuals normalised to the data uncertainty are shown at the bottom of each distribution.

found to be in good agreement among the three electron trigger categories (see figure 4.7.3). The results are given in table 4.7.2 and presented in figure 4.7.4, where they are compared both to the SM predictions and to previous measurements from the B factories [83, 84].

The combined $R_{K^{*0}}$ PDF is used to determine the compatibility with the SM expectations. The p-value, calculated by integrating the PDF above the expected value, is translated into a number of standard deviations. The compatibility with the SM expectations [81, 85–93] is determined to be 2.1–2.3 and 2.4–2.5 standard deviations, for the low-q^2 and the central-q^2 regions, respectively, depending on the theory prediction used.

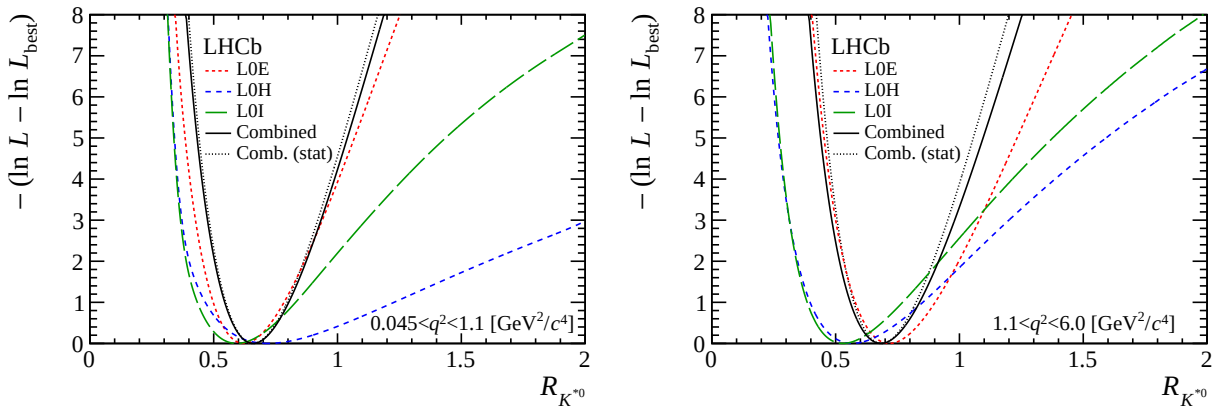

Figure 4.7.3: Distributions of the $R_{K^{*0}}$ delta log-likelihood for the three trigger categories separately and combined.

Table 4.7.2: Measured $R_{K^{*0}}$ ratios in the two q^2 regions. The first uncertainties are statistical and the second are systematic. About 50% of the systematic uncertainty is correlated between the two q^2 bins. The 95.4% and 99.7% confidence level (CL) intervals include both the statistical and systematic uncertainties.

	low-q^2	central-q^2
$R_{K^{*0}}$	$0.66\ ^{+\ 0.11}_{-\ 0.07} \pm 0.03$	$0.69\ ^{+\ 0.11}_{-\ 0.07} \pm 0.05$
95.4% CL	$[0.52, 0.89]$	$[0.53, 0.94]$
99.7% CL	$[0.45, 1.04]$	$[0.46, 1.10]$

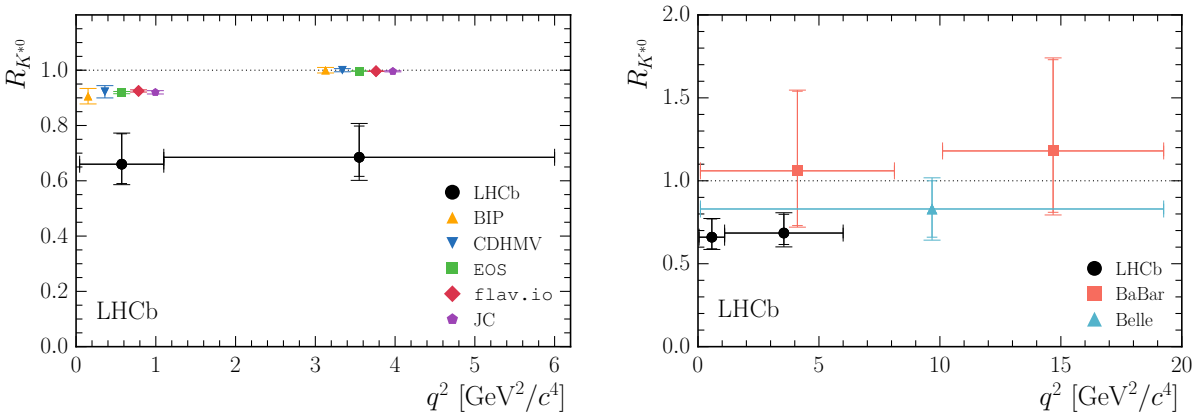

Figure 4.7.4: (left) Comparison of the LHCb $R_{K^{*0}}$ measurements with the SM theoretical predictions: BIP [85] CDHMV [86–88], `EOS` [89,90], `flav.io` [81,91,92] and JC [93]. The predictions are displaced horizontally for presentation. (right) Comparison of the LHCb $R_{K^{*0}}$ measurements with previous experimental results from the B factories [83, 84]. In the case of the B factories the specific vetoes for charmonium resonances are not represented.

Chapter 5

Searches for lepton-flavor-violating B decays

The puzzling absence of a mixing matrix for the charged leptons can be challenged by searches of charged lepton flavor violating decays. This chapter presents three searches for lepton-flavor-violating B decays $B^+ \to K^+\mu^\pm e^\mp$ [3], $B^0 \to K^{*0}\tau^\pm\mu^\mp$ [4] and $B^0 \to K^{*0}\tau^\pm e^\mp$ [5] conducted in LHCb, currently providing the most stringent limits on these decays. Considering the high efficiency of the LHCb muon hardware trigger, it has been natural to start searching for lepton flavor violating decays with at least a muon in the final state, and therefore a clear trigger signature, like in $B^+ \to K^+\mu^\pm e^\mp$ and $B^0 \to K^{*0}\tau^\pm\mu^\mp$. The search for $B^0 \to K^{*0}\tau^\pm e^\mp$ decays, with no muon in the final state, was only performed recently. It was the first analysis in LHCb of a decay with a final state containing both an electron and a τ lepton, demonstrating the feasibility of such searches despite the combination of energy loss due to the neutrino from the τ and bremsstrahlung from the electron. It allowed to complete the coverage of all the possible lepton family combinations for the lepton flavor violating searches in LHCb. We will highlight the challenges, the common aspects and the main differences of these searches.

5.1 Analyses strategies

The $B^+ \to K^+\mu^\pm e^\mp$ search has been performed on $3\,\text{fb}^{-1}$, corresponding to Run1 data, while the $B^0 \to K^{*0}\tau^\pm\mu^\mp$ analysis makes use of the full run 1 and run 2 data set, corresponding to $9\,\text{fb}^{-1}$. The $B^0 \to K^{*0}\tau^\pm e^\mp$ search, instead, has used only run 2 data. The choice of the dataset size was not only driven by the timeline of the analyses. The amount of background for the $B^0 \to K^{*0}\tau^\pm\mu^\mp$ search is much larger than for the $B^+ \to K^+\mu^\pm e^\mp$ search. Therefore, there was the need of a larger data sample to ensure understanding the nature of the background and to make a refined selection. For $B^0 \to K^{*0}\tau^\pm e^\mp$, the stripping selection was only made available for the Run 2 data taking.

Overall, the strategies of the analyses are very similar. In each channel, the two final states with different lepton charges combination (i.e. $\ell^+\ell'^-$ and $\ell^-\ell'^+$) are studied independently for two reasons. The first one is theoretical: physics beyond the standard model could affect differently the two final states. The second is experimental: physics backgrounds affecting

each of the two charge combinations are not necessarely the same. The event selection, discussed in chapter 2, proceeds through multiple steps, each dedicated to rejecting a specific type of background. For LFV searches, it is very important to avoid any background that could fake a signal. Therefore, the selection is harsh and the total efficiency low. Information on the evolution of the efficiency as function of the relevant kinematic degrees of freedom is an important information for recasting the results in different new physics models. All the analyses provides information for this purpose, though with different degrees of details.

Given the large uncertainties on the integrated luminosity and on the b-hadron production cross section, in LHCb it is more appropriate to measure ratio of branching fractions, where these quantities cancels out. The decay used as denominator is called normalization channel:

$$\mathcal{B}(b \to s\ell\ell') = N(b \to s\ell\ell') \times \alpha, \tag{5.1.1}$$

with:

$$\alpha \equiv \frac{\mathcal{B}(norm)}{N(norm)} \cdot \frac{\varepsilon(norm)}{\varepsilon(b \to s\ell\ell')}. \tag{5.1.2}$$

where $\mathcal{B}$, N and ε indicate the branching fraction, the yields and the efficiency, respectively, of the signal channel, generically indicated as $b \to s\ell\ell'$, or the normalization channel, generically indicated as $norm$. The factor α is called single event sensitivity. The key aspect of the analysis is to determine the efficiencies and the yields, while $\mathcal{B}(norm)$ is an external input.

The normalization channel is usually chosen for its abundance and the precise knowledge of its absolute branching fraction from previous measurements. In addition, it should be easily reconstructible, so that a pure sample of events can be selected. Finally, if the normalization channels has similarities with the topology and kinematics of the signal channel, a number of systematic uncertainties will also cancel out in the ratio, especially if the selection of the two channels are kept as similar as possible. For $B^+ \to K^+\mu^\pm e^\mp$, the normalization channel is $B^+ \to J/\psi(\to \mu^+\mu^-)K^+$. This decays has a large, well know branching ratio, and the only difference in the final state is the presence of a muon instead of an electron. Since there are three tracks in both final states, the systematic uncertainty on the track reconstruction efficiency cancels out to a large extent, except for differences in electron versus muon reconstruction. For $B^0 \to K^{*0}\tau^\pm\mu^\mp$ and $B^0 \to K^{*0}\tau^\pm e^\mp$, the normalization channel is $B^0 \to D^-(\to K^+\pi^-\pi^-)D_s^+(\to K^+K^-\pi^+)$, containing six tracks in the final state as the signal, three of which forming a secondary displaced vertex from a charm meson, analogously to the τ. It is also a sufficiently abundant decay, with a known branching fraction of $(3.6 \pm 0.4) \times 10^{-5}$ and good reconstruction efficiency. Since it is possible to select clean samples of these normalization channels, they are also used for cross-checks, calibration of the simulations and determination of related systematic uncertainties. The $B^+ \to K^+\mu^\pm e^\mp$ analysis makes also use of $B^+ \to J/\psi(\to ee)K^+$ decays asan additional control channel.

The selection, systematics and most of the cross-checks are finalized without looking into the signal region, according to the "blind analysis" approach. A fit is performed on the mass of signal B candidates, evaluated with different methods depending on the analysis. The signal yields are expressed as function of the signal $\mathcal{B}$, so that $\mathcal{B}$ is directly determined by the fit. In all cases, no signal events have been observed, therefore upper limits are set using the CLs method.

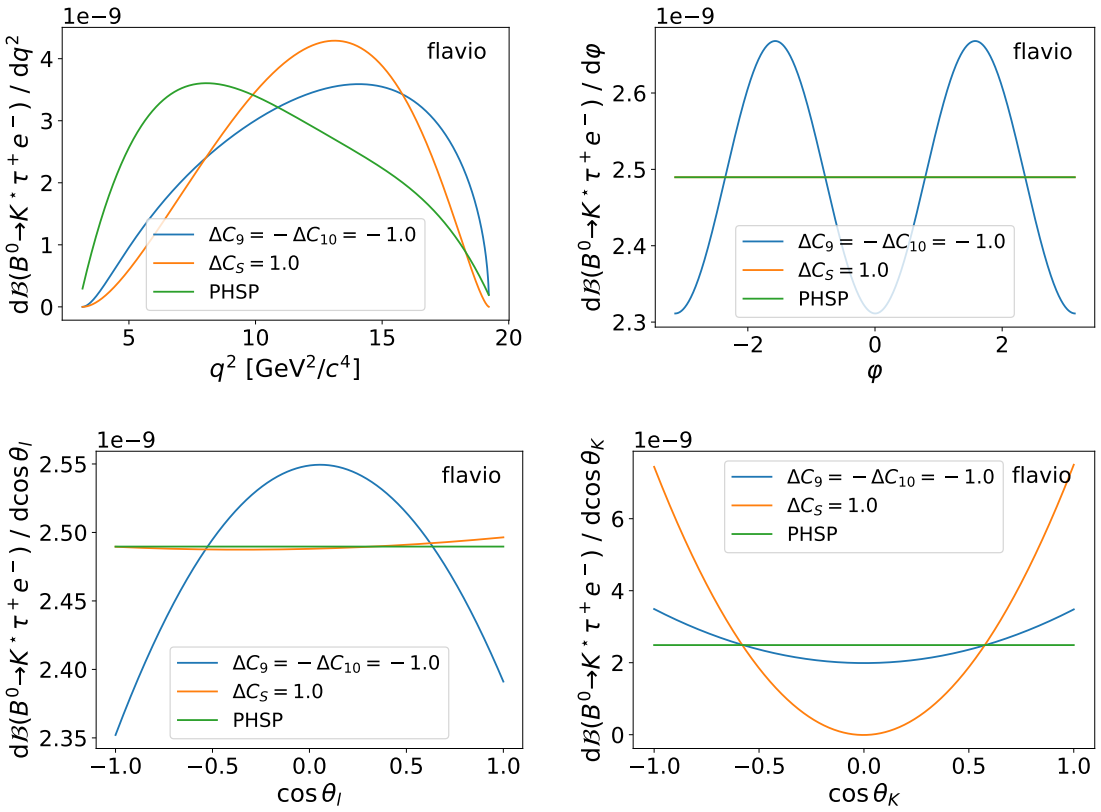

Figure 5.2.1: q^2 and angular distributions for a phase space simulation (PHSP) and two alternative new physics scenarios for $B^0 \to K^{*0}\tau^{\pm}e^{\mp}$ decays.

5.2 Role and determination of the selection efficiency

The selection efficiency enters directly in the measurement or in the upper limit on a branching fraction. In these searches, it is mostly determined using simulations, apart from some particle identification and trigger efficiencies determined using data control samples. Since the kinematics underlying the possible physics beyond the standard model is unknown, the events are simulated assuming a uniform phase space model for the particles in the final state. However, the q^2 and angular distributions of events could be different in different new physics models. This is illustrated by the example in figure 5.2.1 for $B^0 \to K^{*0}\tau^{\pm}e^{\mp}$ decays. The efficiency, and consequently the upper limit, could also be different in the different new physics scenarios with different kinematics. For this reasons, it is important to provide the normalized efficiency distributions in bins of the relevant kinematic variables. They contain the information for re-casting the limit according to different new physics hypothesis.

For $B^+ \to K^+\mu^{\pm}e^{\mp}$, the relevant variables are, at first order, the invariant masses of two of the particles in the final state: $m^2_{K\mu}$ and m^2_{Ke} and the distributions are shown in figure 5.2.2. Analogous variables are used for $B^0 \to K^{*0}\tau^{\pm}\mu^{\mp}$, i.e. $m^2_{K^{*0}\mu}$ and $m^2_{\tau\mu}$, see figure 5.2.3. In addition, since the K^{*0} and the τ further decay, the impact of their polarizations on the

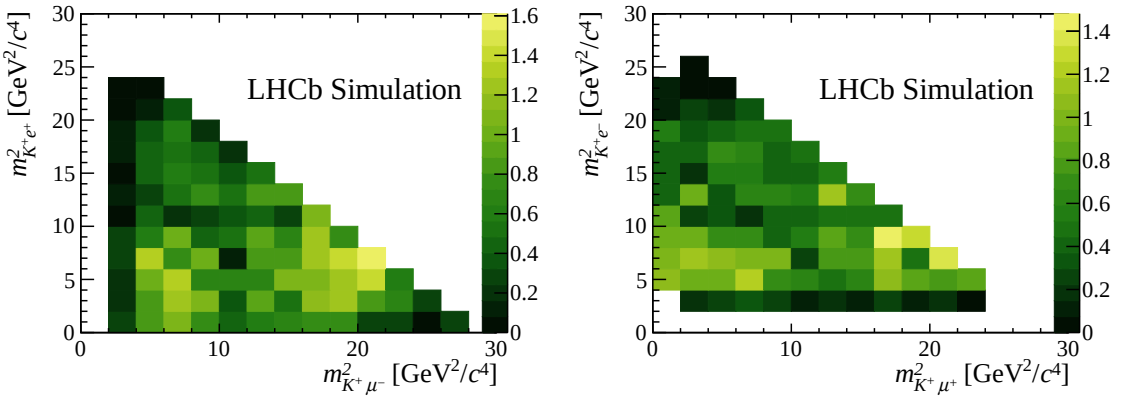

Figure 5.2.2: Normalized efficiency distributions for the $B^+ \to K^+\mu^\pm e^\mp$ search.

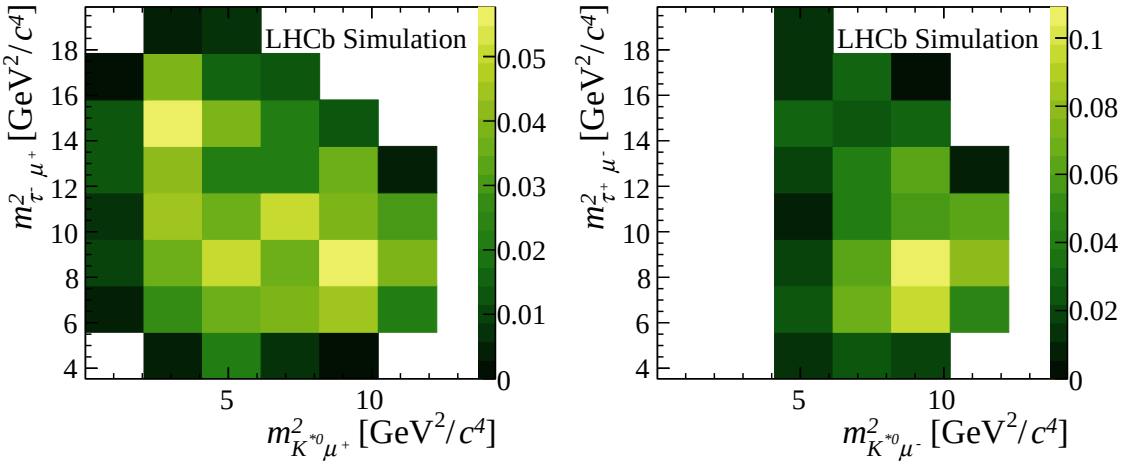

Figure 5.2.3: Normalized efficiency distributions for the $B^0 \to K^{*0}\tau^\pm\mu^\mp$ search.

efficiency has been evaluated and found to be negligible. The $B^0 \to K^{*0}\tau^\pm e^\mp$ analysis has a more complete approach: the efficiencies are provided as function of q^2 and of the angular distributions of the particles in the final state 5.2.4. Using this information, simulations are reweighted and the upper limits are additionally calculated in two benchmark new physics scenarios.

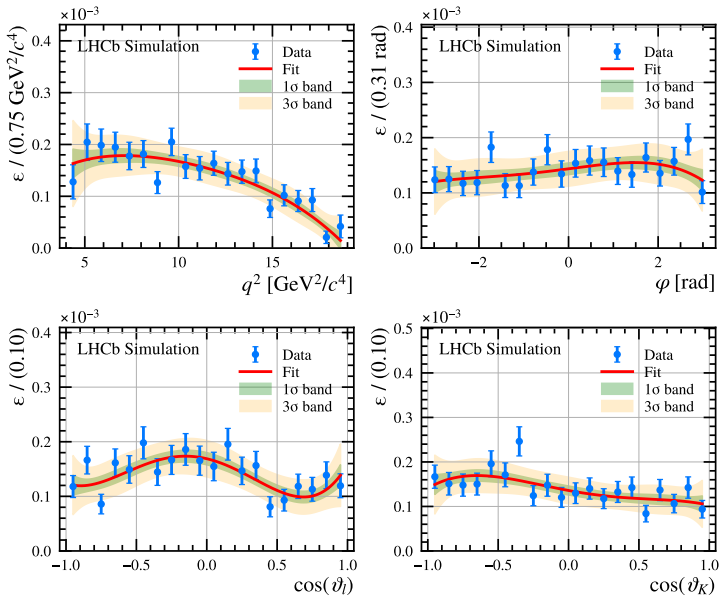

Figure 5.2.4: Normalized efficiency distributions for one of the $B^0 \to K^{*0}\tau^{\pm}e^{\mp}$ decays.

5.3 Signal candidate mass reconstruction and parameterisation

The distribution of the B candidates mass plays a crucial role, since it is the one used to perform the final fit and determine if signal events are observed. Because, depending on the analysis, there are different unreconstructed particles in the final state (neutrinos, π^0s and bremsstrahlung), different techniques are used to determine the mass.

In the case of $B^+ \to K^+\mu^{\pm}e^{\mp}$, the missing energy comes from bremsstrahlung. As discussed in 2, there is an impact on the mass resolution depending on whether bremsstrahlung has been included in the momentum calculation of the electrons or not. Therefore, the invariant mass distribution of signal is modelled differently accounting for this. The signal distributions are parameterised using shapes taken from simulation, but the parameters are corrected by factors evaluating the difference between data and simulation in the two control channels $B^+ \to XJ/\psi(\to \mu^+\mu^-)$ and $B^+ \to K^+J/\psi(\to e^+e^-)$.

In $B^0 \to K^{*0}\tau^{\pm}\mu^{\mp}$ and $B^0 \to K^{*0}\tau^{\pm}e^{\mp}$ searches, the neutrino from the τ decay is not reconstructed, because it does not interact with the detector. In addition, the π^0 meson from the $\tau^- \to \pi^-\pi^+\pi^-\pi^0\nu_\tau$ decay is ignored during the reconstruction. Hence, the invariant masses of the six tracks in the final state, $m(K^{*0}\tau\mu)$ and $m(K^{*0}\tau e)$, peak at a value lower than the true B^0 meson mass and exhibits degraded resolution. These variables are obviously poorly suited to separate signal from background. Alternative approaches have been investigated to recover at least part of the energy loss.

The $B^0 \to K^{*0}\tau^{\pm}\mu^{\mp}$ analysis uses the corrected mass $m_{\rm corr} = \sqrt{p_\perp^2 + m^2_{K^*\tau\mu}} + p_\perp$, where $p_\perp$ is the component of the missing momentum perpendicular to the direction of flight of the B

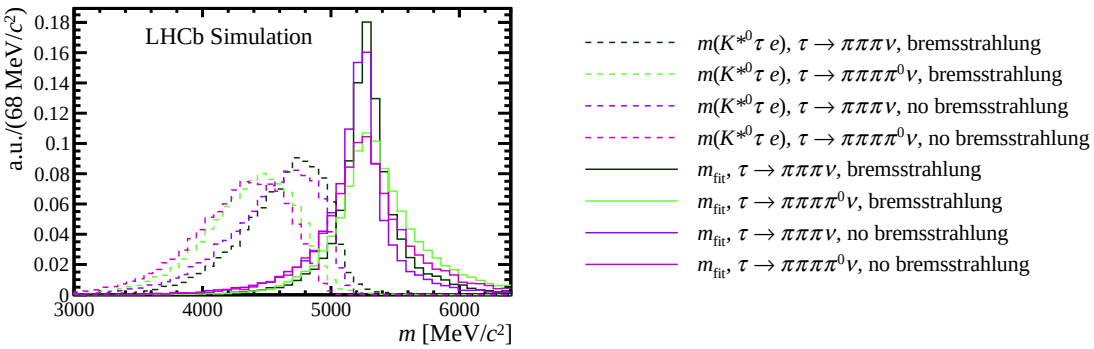

Figure 5.3.1: Comparison in simulated signal candidates between the mass $m(K^{*0}\tau e)$, corresponding to the invariant mass of the tracks in the final state (dashed lines), and the mass $m_{\rm fit}$ accounting for the missing momentum carried from the neutrino via a decay chain fit with kinematic constraints (full lines).

meson [94] determined using its production and decay vertexes. The corrected mass exploits the fact that $p_\perp$ should be equal in module and opposite in sign to the momentum component of the visible particles which is perpendicular to the direction of flight of the B meson. The corrected mass signal shape is then parametrised using two components, one corresponding to the dominant contribution $\tau^- \to \pi^-\pi^+\pi^-\nu_\tau$ and the other to the sub-dominant contribution $\tau^- \to \pi^-\pi^+\pi^-\pi^0\nu_\tau$. The latter has a larger width due to the missing π^0. In both cases the distributions are taken from dedicated simulations.

In $B^0 \to K^{*0}\tau^\pm e^\mp$, an additional step forward was done. The B^0 mass is calculated from a kinematic fit in which the entire decay chain is reconstructed imposing the following constraints [95]: the three charged pions from the tau decay must form a vertex; the missing momentum in the decay chain is attributed to a massless neutrino originating from the τ-decay vertex; the mass of the τ candidate is constrained to the known τ mass; the τ candidate must originate from the B^0 decay vertex, which is reconstructed using the charged kaon and pion from the K^{*0} decay, along with the electron. The resulting mass, denoted $m_{\rm fit}$, has a largely improved resolution, as shown in Fig. 5.3.1 for simulated events. The fact that the bremsstrahlung further worsens the mass resolution is taken into account by modelling the signal shape differently for candidates where bremsstrahlung has been added. The $B^0 \to K^{*0}\tau^\pm e^\mp$ analysis has both separated signal shapes for the dominant contribution $\tau^- \to \pi^-\pi^+\pi^-\nu_\tau$ and the sub-dominant contribution $\tau^- \to \pi^-\pi^+\pi^-\pi^0\nu_\tau$ and for bremsstrahlung categories. The distributions and the fraction of bremsstrahlung events are also in this case taken from simulations.

5.4 Background parameterizations in the fit

In the $B^+ \to K^+\mu^\pm e^\mp$ analysis, very few background candidates are left after the selection. The remaining background can be assumed of combinatorial nature and parametrized with an exponential function, whose parameter is left floating in the fit. A cross-check is performed

using a polynomial shape, and the difference between the two approaches determines the systematic error on the background shape.

In the $B^0 \to K^{*0}\tau^{\pm}\mu^{\mp}$ and $B^0 \to K^{*0}\tau^{\pm}e^{\mp}$ analyses, instead, the background after selection is reduced but still abundant, and its parameterization is more of a concern. Signal and background shapes are wide and largely superpose in the mass spectrum. The composition of the residual background is a cocktail of partially reconstructed and combinatorial decays, that is difficult to reproduce in simulation. In addition, the fit in the sideband region is not stable enough to determine the background shape. For this reason, the shape is evaluated from background enriched control samples, which are obtained reverting the combinatorial multivariate selection. In the final fit, the parameters are Gaussian constrained to the value found in the fit of these control samples, considering also uncertainties deriving by selecting control sample with a different multivariate selection than the default one. The determination of the background shape is a dominant systematic uncertainty in this analysis.

The use of same-sign leptons data as proxy for the combinatorial background, a common approach in many analyses, has also been explored in these searches. This approach usually reproduces the same shapes as the opposite-sign leptons data in the high sideband, which is dominated by combinatorial background, and indeed it gives compatible results. However, same-sign leptons data cannot be used to parameterise the physics backgrounds which dominates the low mass sideband, which is the largest in these searches. In fact, the physics composition of the background is different in same-sign and opposite-sign leptons data, because the charge structure of the decays is not the same.

5.5 Systematic uncertainties

Relevant systematic uncertainties in the searches for lepton flavor violating decays broadly belong to three categories: uncertainties related to the external input; uncertainties on the determination of the efficiencies; fit parametrisations uncertainties. This is similar to the case of the $R_{K^{*0}}$ analysis. However, the differences between the signal and normalization mode are larger in the lepton flavor violating searches, in particular in the case of decays with a τ. Additionally, these analyses relies more on simulation for the determination of the efficiency, since there are no signal candidates observed nor control samples with exactly the same final state.

For $B^+ \to K^+\mu^{\pm}e^{\mp}$, the summary of systematic uncertainties is reported in Tab. 5.5.1 as variation on the single event sensitivity α. The dominant source is the PID resampling, which has an impact on the determination of the selection efficiency. For $B^0 \to K^{*0}\tau^{\pm}\mu^{\mp}$ and $B^0 \to K^{*0}\tau^{\pm}e^{\mp}$, instead, the effect of the systematic uncertainties is summarised in Tables 5.5.2 and 5.5.3, where the increase of the observed upper limit when applying each of the systematic uncertainties on top of the others is shown. For $B^0 \to K^{*0}\tau^{\pm}e^{\mp}$ there is an additional uncertainty related to the procedure used for reconstructing the mass of the candidates. The dominant systematic effect for both channels is related to the background parametrisation and, in particular, from the uncertainty on the arbitrary choice of the control region. The systematic effects are larger for the $B^0 \to K^{*0}\tau^{\pm}\mu^{\mp}$ mode than the $B^0 \to K^{*0}\tau^{\pm}e^{\mp}$, because the amount of background and the signal mass resolution are larger

in the first case. In the following, the systematic uncertainties are further discussed for each channel.

5.5.1 Systematic uncertainties for $B^+ \to K^+\mu^\pm e^\mp$

External input

The uncertainty on the $B^+ \to K^+ J/\psi(\to \mu^+\mu^-)$ branching fraction is combined with the uncertainty due to the limited size of the simulation sample and is propagated to the normalisation constant, corresponding to a systematic uncertainty of 3.5%.

Efficiencies

The efficiencies related uncertainties include:

- residual differences in the kinematic of B-meson production
- Residual difference between correcting the muon and electron candidates. A small difference in the correction procedure is observed depending on the choice of control channel, namely $B^+ \to K^+ J/\psi(\to \mu^+\mu^-)$ or $B^+ \to K^+ J/\psi(\to e^+e^-)$. This difference, referred to as electron-muon difference, is taken as systematic uncertainty.
- PID resampling. This includes two components. The first stems from applying the *sPlot* [82] method to the calibration data, and adds an uncertainty of 0.1% for kaons and muons, and 3% for electrons, the latter being a conservative estimate originating from a comparison of the *sPlot* method with a cut-and-count method. The second component addresses the choice of binning in the sampling procedure. It is evaluated by recalculating the normalisation factor α using a finer and a coarser binning, and taking the largest deviation with respect to the baseline result.
- trigger efficiencies, estimated with data-driven techniques using samples selected by alternative trigger selections.

Background fit model

The systematic uncertainty from the fitting model is determined to be 2.1% using a bootstrapping approach. The systematic uncertainty on the background model is calculated by repeating the fit using an alternative model, where the exponential function is obtained from a sample enriched in background events. The difference between the alternative and nominal background parametrization is taken as a systematic uncertainty.

5.5.2 Systematic uncertainties for $B^0 \to K^{*0}\tau^\pm\mu^\mp$ and $B^0 \to K^{*0}\tau^\pm e^\mp$

External inputs

The conversion of the signal yields into branching fractions involves external inputs from known intermediate branching fractions. The corresponding systematic uncertainty is assigned

by imposing constraints using Gaussian priors with width corresponding to the intermediate branching fractions uncertainties.

Efficiencies

The measurement involves ratios of signal and normalisation efficiencies, for which systematic uncertainties cancel to a large extent. However, residual differences between signal and normalization channels implies that some effects do not compensate. They are assessed as follows.

- **Size of simulation samples.** The uncertainty related to the limited size of the simulation samples used to determine the efficiencies is taken into account and included as part of the statistical uncertainty.

- **Tracking.** The ratio of the tracking efficiency between the signal and normalisation channels is determined from simulation. However, the sixth hadron in the normalisation channel interacts differently with the material with respect to the muon or the electron in the signal channel. Therefore, in the tracking efficiency ratios, a 1.4% uncertainty is assigned to the hadron [96]. For the electron, an additional 0.6% uncertainty is considered, evaluated with data control samples [97].

- **Particle identification.** The systematic uncertainty on the determination of the PID selection efficiency accounts for: the limited size of simulation and calibration samples; the choice of the p, η and number of tracks interval sizes; and the use of the *sPlot* technique [82] to extract the signal yield in the control samples.

- **Multivariate classifiers.** Although the simulation of the variables used in the multivariate classifiers is validated with the normalisation channel, small residual discrepancies could affect the evaluation of the classifier efficiencies. To account for this, the $B^0 \to D^- D_s^+$ candidates with a mass within $50\,\mathrm{MeV}/c^2$ of the known mass [98] of the B^0 meson are selected from both data and simulation, providing a high purity sample on which the classifiers used to select the $B^0 \to K^{*0}\tau\mu$ (or the $B^0 \to K^{*0}\tau^{\pm}e^{\mp}$) signal are applied. The variables of the classifiers relative to the τ lepton are applied to the D^- meson and analogously those of the K^{*0} are applied to the D_s^+ meson. For each classifier, the requirement giving an efficiency on the $B^0 \to D^- D_s^+$ simulation sample equivalent to that obtained by the requirement on the simulated $B^0 \to K^{*0}\tau\mu$ (or $B^0 \to K^{*0}\tau^{\mp}e^{\pm}$) sample is determined. The relative systematic uncertainty is defined as the difference between $B^0 \to D^- D_s^+$ simulation and data efficiencies when applying this requirement, divided by the $B^0 \to D^- D_s^+$ simulation efficiency.

- **Trigger.** $B^0 \to K^{*0}\tau^{\pm}\mu^{\mp}$ is selected using an hardware muon trigger which, over the entire data taking period, has seen changes, in particular concerning the requirement on the transverse momentum of the muon. The hardware muon trigger efficiency evaluated from simulation is therefore multiplied by a correction factor obtained from the ratio between the efficiency from data and simulation for the $B^{\pm} \to J/\psi K^{\pm}$ control sample.

These corrections are functions of the muon transverse momentum. The difference between the efficiency resulting from this weighting procedure and the efficiency from simulation is taken as a systematic uncertainty. The overall effect is less than 1%.

The hardware hadron trigger, used in the selection of the normalisation channel, is less well reproduced in simulation. A data-driven efficiency estimation is provided by the number of events triggered simultaneously by any muon in the event and one of the hadrons in the $B^0 \to D^- D_s^+$ decay, divided by the number of events triggered by any muon in the event. The absolute difference with the efficiency estimated on the $B^0 \to D^- D_s^+$ simulation is assumed as a systematic uncertainty.

In the case of $B^0 \to K^{*0}\tau^\pm e^\mp$, the calibration procedure of the hardware trigger efficiency, performed separately for each trigger category, has associated systematic effects. The first uncertainty is related to the limited size of the data and simulation samples used. In addition, the impact of different binning schemes is checked for the relevant variables used by the calibration. This turns out to be the dominant systematic effect for the hardware trigger efficiencies. For the TIS category, the $p_{\rm T}$ distribution of the B meson, taken by default from simulation, is also corrected using the $B^0 \to D^- D_s^+$ data sample to assess the impact on the determination of the TIS efficiency. The largest difference in the efficiency obtained using data samples alternative to that used in the baseline is also accounted for as an uncertainty.

Conversely, for the software trigger, no significant discrepancy is observed between the efficiencies determined from simulation and from the high purity $B^0 \to D^- D_s^+$ sample.

Normalization channel fit model

The systematic uncertainty associated with the fit model used for measuring the normalisation channel yields is assessed using pseudoexperiments, generated from a kernel-density estimation of the $B^0 \to D^- D_s^+$ mass distribution and an exponential function for the background. The pseudoexperiments are subsequently fitted using the baseline model for the normalisation channel. The relative systematic uncertainty, evaluated as the ratio between the mean fitted and generated yields, is 1.8% for Run 1 and 1.7% for Run 2 for the $B^0 \to K^{*0}\tau^\pm\mu^\mp$ channel, while is 0.2% for the $B^0 \to K^{*0}\tau^\pm e^\mp$ channel.

Background fit model

The parameters of the DSCB function describing the background are constrained using Gaussian priors derived from a fit to a background control region, obtained by reverting the combinatorial multivariate selection. Alternative control regions are defined by choosing different requirements on the combinatorial multivariate discriminant. For the $B^0 \to K^{*0}\tau^\pm e^\mp$, Fisher discriminant and the K^{*0} mass window are also used for alternative control regions definitions. The peak position and width of the DSCB are Gaussian-constrained accounting for their variation in these alternative control regions.

In addition, a systematic uncertainty is assigned to the choice of the DSCB functional form. This is assessed by generating samples via a kernel-density estimation of background control

Table 5.5.1: Summary of systematic uncertainties for the $B^+ \to K^+\mu^\pm e^\mp$ search. Uncertainties are expressed as impact on the single event sensitivity.

Effect	$B^+ \to K^+\mu^+e^-$	$B^+ \to K^+\mu^-e^+$
Data-simulation corrections	1.0%	1.0%
Electron-muon differences	1.4%	1.4%
Fitting model	2.1%	2.1%
PID resampling	4.5%	5.5%
Trigger	1.0%	1.0%
Normalisation factor	3.5%	3.5%
Total	6.4%	7.1%
Background	0.60	0.43

samples and fitting them with the nominal DSCB function. This systematic is added to each of the signal branching fractions, constraining its value with a Gaussian function with a mean of zero and a width set to the average value of the bias measured on the pseudoexperiments, which is at the level of 6×10^{-7} for $B^0 \to K^{*0}\tau^\pm\mu^\mp$ and 10^{-7} for $B^0 \to K^{*0}\tau^\pm e^\mp$.

Mass reconstruction for $B^0 \to K^{*0}\tau^\pm e^\mp$

The systematic uncertainty on the signal model includes a contribution associated with the reliability of the mass reconstruction technique. It is assessed by reconstructing $B^0 \to D^- D_s^+$ candidates with only five tracks, thus emulating the missing energy carried by the neutrino from the τ decay in the signal channel. The $m_{\rm fit}$ distribution is then fit in the region $5150 < m_{\rm fit} < 5420$ MeV/c^2, both for selected simulated and data candidates, parameterising the signal with a DSCB function with symmetric widths and the background with an exponential function. Discrepancies between data and simulation on the peak position and the widths of the DSCB are summed in quadrature, with the statistical uncertainties coming from the determination of their values from simulation. The results are used as Gaussian constraints in the fit to the data. Additionally, the signal-model systematic uncertainty has a component related to the fraction of bremsstrahlung candidates taken from the simulation. The statistical uncertainty of the simulation sample is combined with the largest discrepancy between the fraction of bremsstrahlung candidates in data and simulation evaluated in $B^0 \to K^{*0}J/\psi(\to e^+e^-)$ decays.

Table 5.5.2: Relative increase (in %) of the observed upper limit on $B^0 \to K^{*0}\tau^{\pm}\mu^{\mp}$ when applying each of the systematic uncertainties. The total is relative to the case when no systematic is included.

Systematic effect	**Upper limit increase [%]**	
	$B^0 \to K^{*0}\tau^-\mu^+$	$B^0 \to K^{*0}\tau^+\mu^-$
Input branching fractions	4	3
Efficiencies	2	1
Normalisation yields	1	1
Background control region choice	18	26
Background analytical shape	1	1
Total	26	32

Table 5.5.3: Relative increase (in %) of the observed upper limit on $B^0 \to K^{*0}\tau^{\mp}e^{\pm}$ when applying each of the systematic uncertainties. The total is relative to the case when no systematic is included.

Systematic effect	**Upper limit increase [%]**	
	$B^0 \to K^{*0}\tau^+e^-$	$B^0 \to K^{*0}\tau^-e^+$
Input branching fractions	2.3	2.5
Normalisation yields	<0.1	<0.1
Efficiencies	1.2	1.0
Background model	4.7	5.2
Signal model	1.2	0.5
Total	9.7	9.5

5.6 Results of the searches

In the three analysis, the fit of the candidates' mass reveals no signal. The distributions are compatible with the background only hypothesis. They are shown on figures 5.6.1 for $B^+ \to K^+\mu^\pm e^\mp$, 5.6.2 for $B^0 \to K^{*0}\tau^\pm\mu^\mp$ and 5.6.3 for $B^0 \to K^{*0}\tau^\pm e^\mp$.

Since no signals are observed, upper limits on the branching fractions of these decays are established using the CL_s method [99,100]. Likelihood functions are computed from the fits to the invariant-mass distributions, with the nuisance parameters gaussian constrained to their nominal value, accounting in this way for both the statistical and systematic uncertainties. Pseudoexperiments, in which the nuisance parameters are input at their best fit value and the background yield is varied according to its systematic uncertainty, are used for the evaluation of the test statistic. The resulting upper limits are shown in Fig. 5.6.4, Fig. 5.6.5 and Fig. 5.6.6 for $B^+ \to K^+\mu^\pm e^\mp$, $B^0 \to K^{*0}\tau^\pm\mu^\mp$ and $B^0 \to K^{*0}\tau^\pm e^\mp$, respectively. The numerical results are summarized in Table 5.6.1. All these limits are currently only statistically limited and some systematics are expected to be reduced with more data.

As previously indicated, the upper limits on $B^0 \to K^{*0}\tau^\pm\mu^\mp$ and $B^0 \to K^{*0}\tau^\pm e^\mp$ branching fractions assume a uniform distribution of the signal events within the phase space accessible to the final state particles (K^{*0}, tau and muon or electron). They are currently the most stringent upper limits on $b \to s\tau\mu$ and $b \to s\tau e$ transitions.

Upper limits on $B^0 \to K^{*0}\tau^\pm e^\mp$ decays have been computed also in alternative scenarios, accounting for the variation of the reconstruction and selection efficiency with decay kinematics. Two scenarios of physics beyond the SM were considered: a left-handed model with $C_9^{\tau e} = -C_{10}^{\tau e} \neq 0$ and a scalar model with $C_S^{\tau e} \neq 0$, where $C_i^{\tau e}$ are the lepton-flavour-violating Wilson coefficients [101]. For these scenarios, the comparison with phase-space kinematics is shown in figure 5.2.1. The resulting limits are also presented in Table 5.6.1.

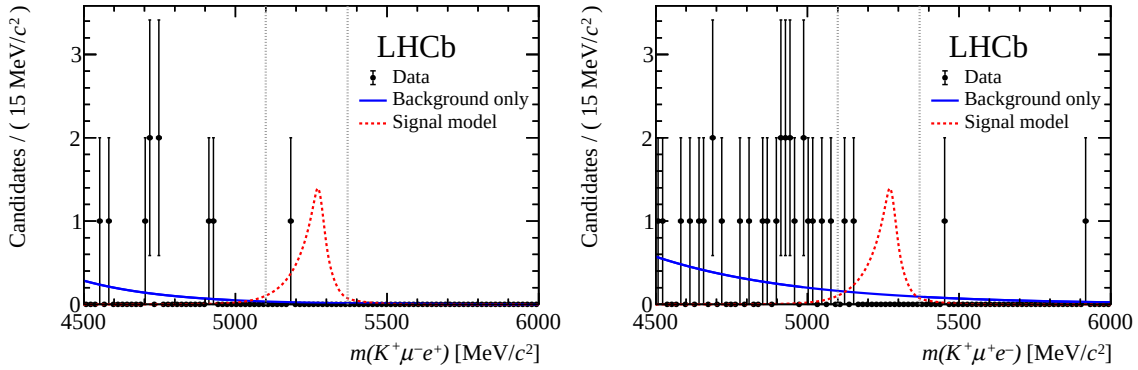

Figure 5.6.1: Invariant-mass distributions of the (left) $B^+ \to K^+\mu^-e^+$ and (right) $B^+ \to K^+\mu^+e^-$ candidates obtained on the combined data sets recorded in 2011 and 2012 with background only fit functions (blue continuous line) and the signal model normalised to 10 candidates (red dashed line) superimposed. The signal window is indicated with grey dotted lines. Difference between the two distributions arises from the effect of the $m(K^+\ell^-)$ requirement.

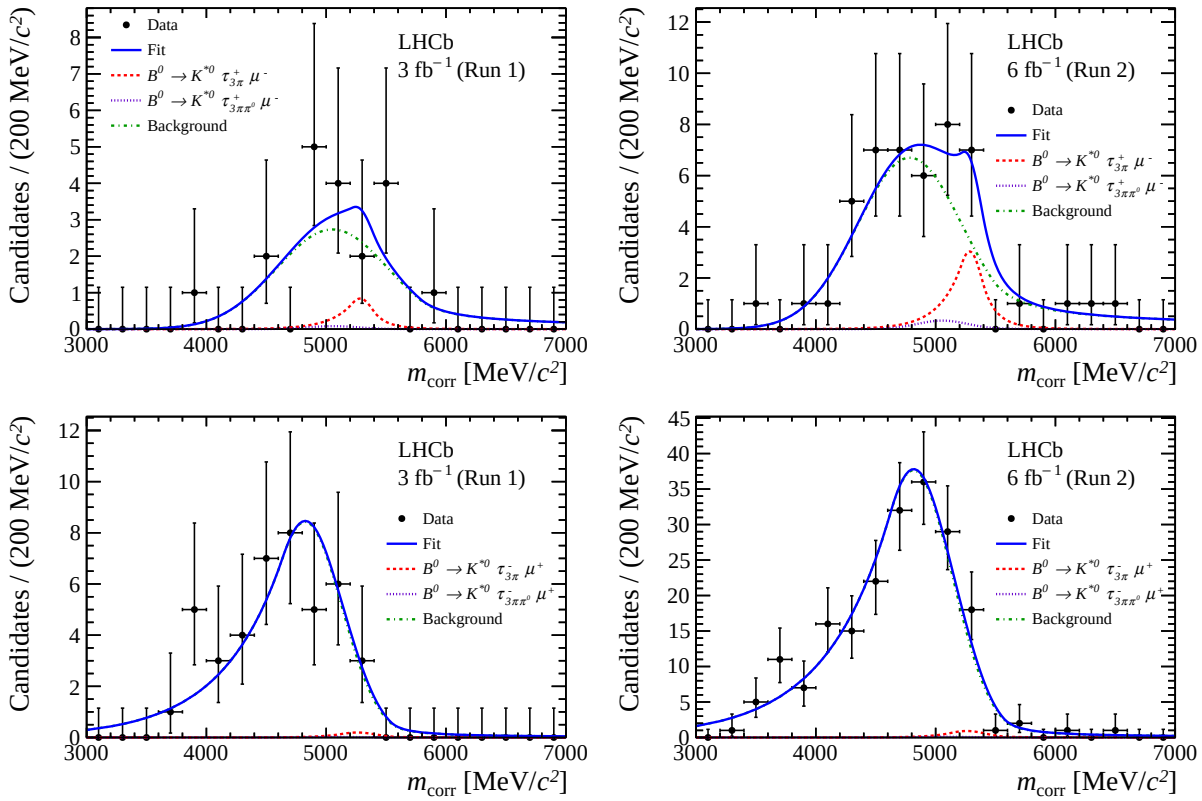

Figure 5.6.2: Distribution of the corrected mass $m_{\rm corr}$ of selected $B^0 \to K^{*0}\tau^+\mu^-$ candidates (top plots) selected $B^0 \to K^{*0}\tau^-\mu^+$ candidates (bottom plots). On the left the distributions for Run 1 and on the right for Run 2 data. The simultaneous fit is overlaid (blue solid line). The red dashed line is the dominant signal component with the τ decaying into three charged pions and a neutrino; the violet dotted line is the subdominant signal component with the τ decaying into three charged pions, a neutral pion and a neutrino, extremely small and consequently barely visible. The green dash-dotted line is the background.

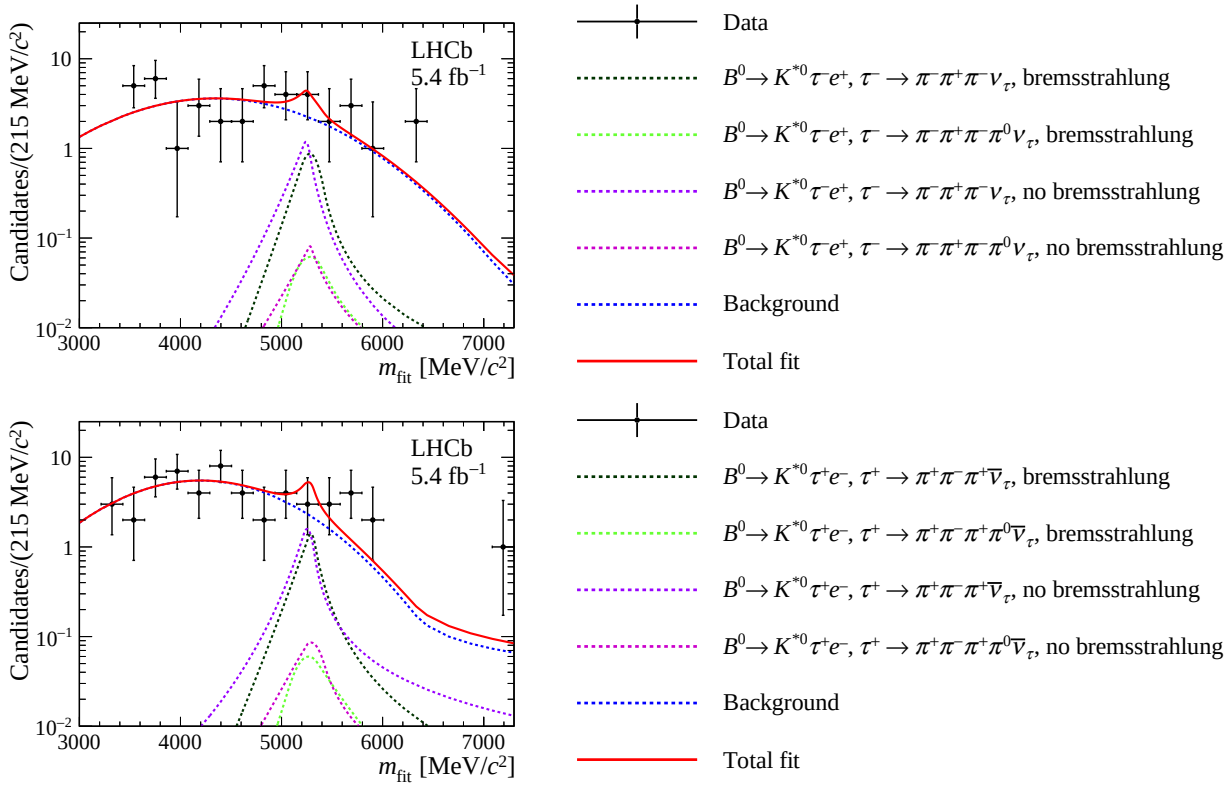

Figure 5.6.3: Distribution of the mass $m_{\rm fit}$ of (top) $B^0 \to K^{*0}\tau^+\mu^-$ and (bottom) $B^0 \to K^{*0}\tau^-\mu^+$ selected candidates, with the simultaneous fit result. Legends with the various components of the fit are shown next to the plots.

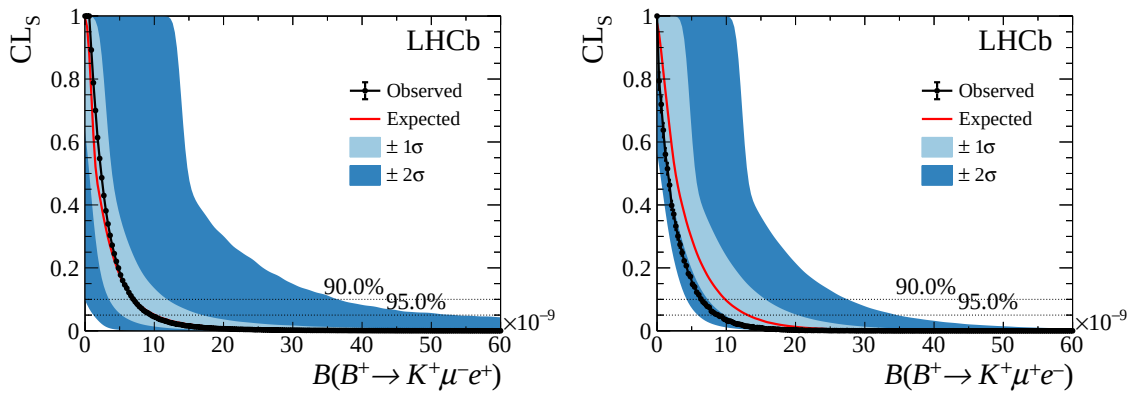

Figure 5.6.4: Expected and observed upper limits on the branching fractions of (left) $B^+ \to K^+\mu^-e^+$ and (right) $B^+ \to K^+\mu^+e^-$ decays. Horizontal lines indicates the 90% and 95% CL.

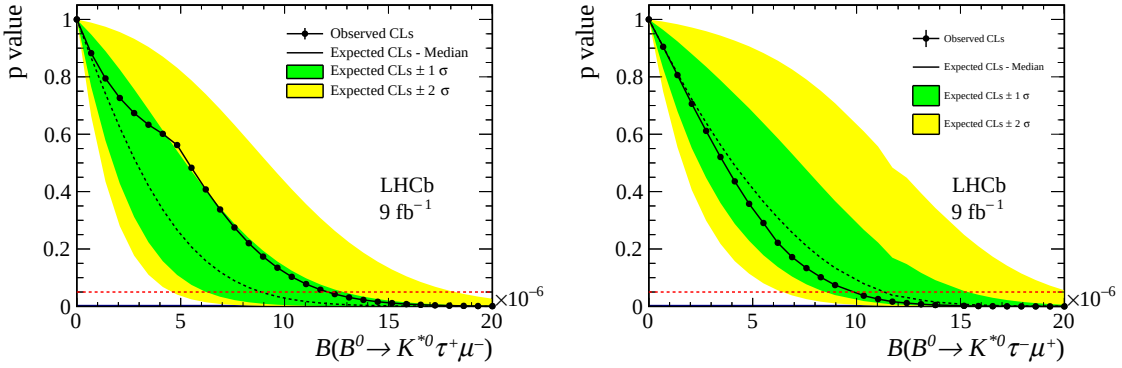

Figure 5.6.5: Expected and observed p-values as a function of the (left) $B^0 \to K^{*0}\tau^+\mu^-$ and (right) $B^0 \to K^{*0}\tau^-\mu^+$ branching fraction. The red line indicates the 95% CL.

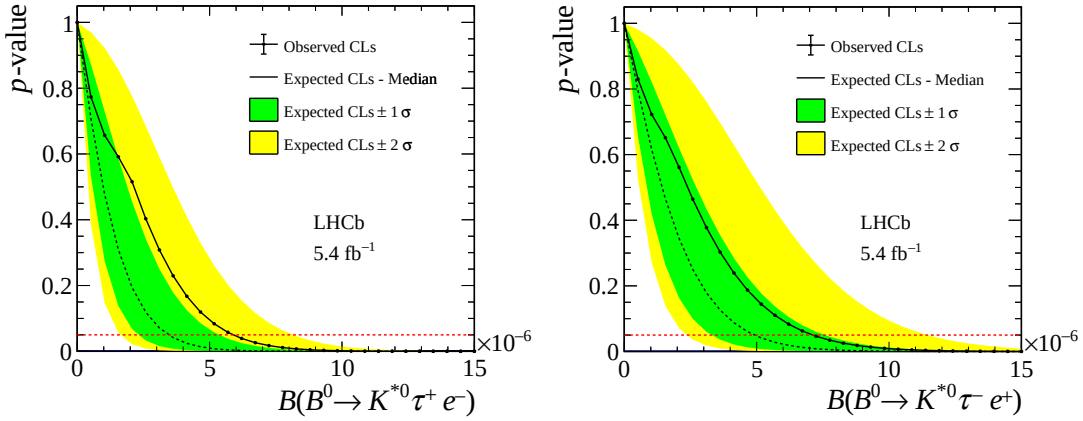

Figure 5.6.6: Expected and observed p-values as a function of the (left) $B^0 \to K^{*0}\tau^+e^-$ and (right) $B^0 \to K^{*0}\tau^-e^+$ branching fraction. The red line indicates the 95% CL.

Table 5.6.1: Upper limits on the branching fraction of the decays for the assumed phase-space model and two beyond the SM scenarios, at 90% (95%) confidence level.

Branching fraction	Model	Upper limit at 90 (95)% CL
$\mathcal{B}(B^+ \to K^+\mu^-e^+)$	Phase space (PHSP)	7.0 (9.5) $\times 10^{-9}$
$\mathcal{B}(B^+ \to K^+\mu^+e^-)$	Phase space (PHSP)	6.4 (8.8) $\times 10^{-9}$
$\mathcal{B}(B^0 \to K^{*0}\tau^+\mu^-)$	Phase space (PHSP)	1.0 (1.2) $\times 10^{-5}$
$\mathcal{B}(B^0 \to K^{*0}\tau^-\mu^+)$	Phase space (PHSP)	8.2 (9.8) $\times 10^{-6}$
$\mathcal{B}(B^0 \to K^{*0}\tau^+e^-)$	Phase space (PHSP)	5.9 (7.1) $\times 10^{-6}$
	Left-handed ($C_9^{\tau e} = -C_{10}^{\tau e} \neq 0$)	6.3 (7.7) $\times 10^{-6}$
	Scalar ($C_S^{\tau e} \neq 0$)	6.6 (8.0) $\times 10^{-6}$
$\mathcal{B}(B^0 \to K^{*0}\tau^-e^+)$	Phase space (PHSP)	4.9 (5.9) $\times 10^{-6}$
	Left-handed ($C_9^{\tau e} = -C_{10}^{\tau e} \neq 0$)	5.4 (6.4) $\times 10^{-6}$
	Scalar ($C_S^{\tau e} \neq 0$)	5.7 (6.8) $\times 10^{-6}$

Chapter 6

Recent progress and perspectives

The analyses presented in this document are part of a more general effort aiming at discovering physics beyond the Standard Model through the study of FCNC transitions, the tests of lepton flavor universality and the search for charged lepton flavor violating decays. Since their publication, the angular analysis of $B^0 \to K^{*0}\mu^+\mu^-$ decays and the $R_{K^{*0}}$ measurements have been updated by LHCb using larger data samples and improved techniques. Complementary measurements have been performed, including by other experiments. This chapter will provide an overview of these results and synthetise the current interpretation of $b \to s\ell\ell$ transitions. It will also present an overview of the charged lepton flavor violation searches. Finally, it will discuss future prospects and a research project for the future.

6.1 Advances in angular analysis

Measurement in Belle

In 2016, the Belle collaboration has published a measurement of the angular observables of $B \to K^*\ell^+\ell^-$ decays, where ℓ is either e or μ, therefore including a test of lepton flavor universality [102]. The measurement uses the decays:

$$B^0 \to K^{*0}\mu^+\mu^-, \quad B^+ \to K^{*+}\mu^+\mu^-, \quad B^0 \to K^{*0}e^+e^-, \quad B^+ \to K^{*+}e^+e^-$$

where $K^{*+} \to K^+\pi^0$ or $K^0_S\pi^+$. The analysis is performed on a data sample corresponding to an integrated luminosity of 711 fb^{-1} containing 772×10^6 $B\bar{B}$ pairs, collected at the $\Upsilon(4S)$ resonance with the Belle detector at the asymmetric-energy e^+e^- collider KEKB.

Because of the limited statistics available, the analysis is performed in only four independent bins of q^2 and an additional bin in the range $q^2 \in [1.0, 6.0]$ GeV$^2/c^4$, using a data-transformation technique to simplify the differential decay rate without losing experimental sensitivity. The transformation is applied to specific regions in the three-dimensional angular space, exploiting the symmetries of the cosine and sine functions to cancel terms in the angular distribution. This is similar to the approach of the early angular measurement in LHCb. After transformation, the remaining observables are the K^* longitudinal polarization F_L, the transverse polarization asymmetry $A_T^{(2)} = 2S_3/(1 - F_L)$, and P'_4 or P'_5. All

measurements are found compatible with the SM predictions, with the strongest tension of 2.6σ for P_5' in the muon modes in the region $q^2 \in [4.0, 8.0]$ GeV$^2/c^4$, similar to the region where LHCb reported the P_5' discrepancy.

Performing these measurements in an experiment like Belle, with a totally different apparatus, operating at a different accelerator, implies different systematic uncertainties with respect to measurements at the LHC experiments. It is therefore a very important cross-check of the current results, even if with lower sensitivity, that will certainly be improved by the larger data sample of Belle II. Another relevant aspect of this publication is that the measurements are compared and found compatible between electrons and muons. In fact, the $Q_{4,5}$ observables, defined as the difference of the P' variables between electrons and muons, are presented in this article for the first time (see Figure 6.4.2) and show no significant deviation from zero. Despite the large uncertainties, the measurement indicates that a lepton flavor universality test of the angular distributions is a promising path to follow for the future.

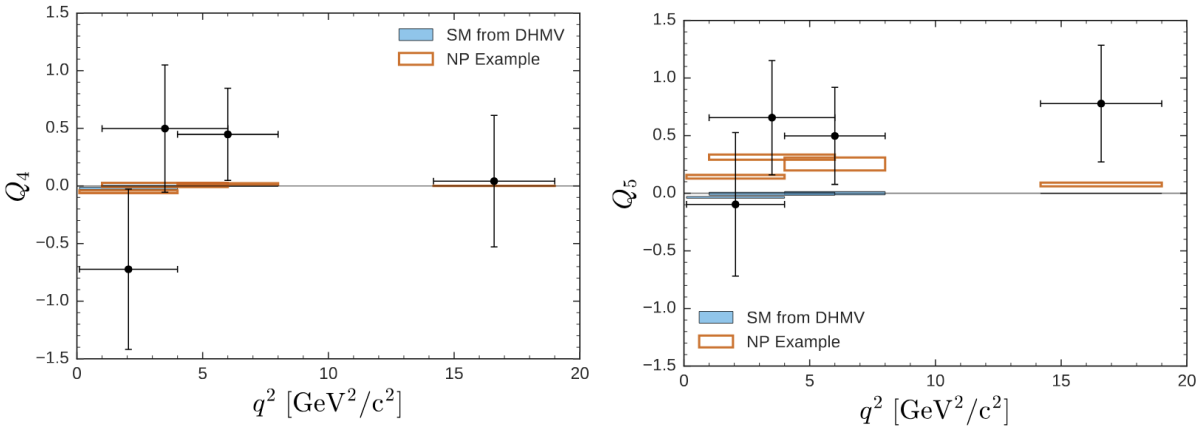

Figure 6.1.1: First experimental measurement of Q_4 and Q_5, performed by the Belle collaboration.

Measurements in ATLAS and CMS

The tensions with the SM arising from the LHCb measurement has motivated a renewed effort in the analysis of B decays also in the general purpose experiments at the LHC. Despite not being dedicated to flavor physics, ATLAS and CMS have developped low momentum triggers to accumulate samples of B decays and can be competitive in particular in decays involving muons in the final state, where the trigger signature is easier.

The ATLAS collaboration [103] published in 2018 an angular analysis of the decay $B^0 \to K^*\mu^+\mu^-$. The study uses 20.3 fb^{-1} of integrated luminosity collected during 2012 at a centre-of-mass energy of $\sqrt{s} = 8$ TeV. Also in this case, trigonometric transformations are used to simplify the equations of the angular distributions, such that three parameters can be extracted in one fit: the K^* longitudinal polarisation fraction F_L, S_3, and one of the other S parameters, in six bins of q^2. The larger deviations from the SM expectations is found in

the P_4' and P_5' measurements in $q^2 \in [4.0, 6.0]$ GeV$^2/c^4$ and P_8' in $q^2 \in [2.0, 4.0]$ GeV$^2/c^4$2, but in general all measurements are found to be within three standard deviations of the range covered by the different SM predictions.

The CMS collaboration published in 2024 its first measurement of the full set of CP-averaged optimized observables using a sample of proton-proton collisions at $\sqrt{s} = 13$ TeV, collected in 2016-2018, corresponding to an integrated luminosity of 140 fb^{-1} [104]. The analysis is performed in six bins of q^2, over the range $q^2 \in [1.1, 16.0]$ GeV$^2/c^4$, providing the most precise experimental measurements of the angular observables after LHCb. As shown in figure 6.1.2, the results are compatible within LHCb, CMS, ATLAS and Belle collaborations.

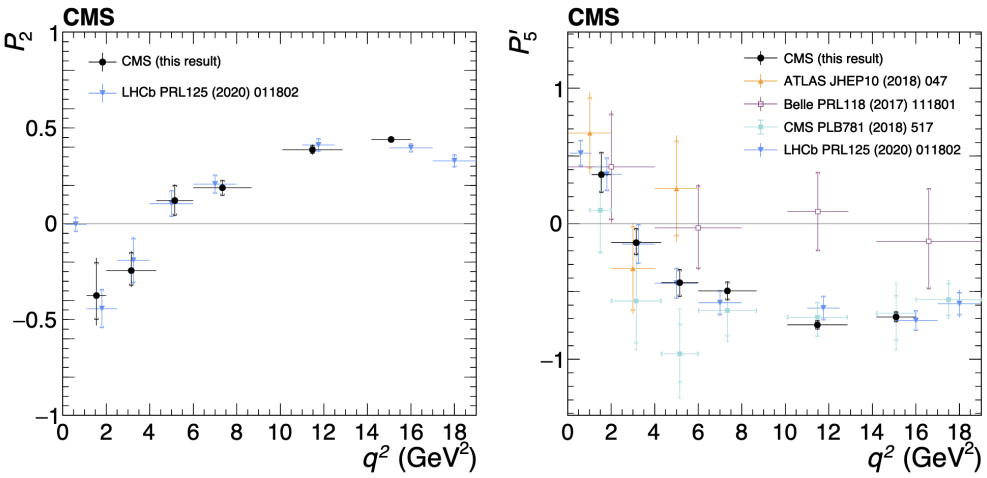

Figure 6.1.2: Comparison of all experimental measurements on $B^0 \to K^{*0}\mu^+\mu^-$ angular analysis up to 2020.

The LHCb update in 2025

The LHCb collaboration has recently published the most precise measurements of the full set of CP-averaged and CP-asymmetric angular observables in $B^0 \to K^{*0}\mu^+\mu^-$ decays, as well as of its branching fraction relative to the $B^0 \to J/\psi K^{*0}$ decay, in bins of q^2 [105]. The new analysis, which overrules previous LHCb measurements, relies on a data set corresponding to an integrated luminosity of 8.4 fb^{-1}, collected by the experiment between 2011 and 2018.

There are two major novelties in this analysis. First, it takes into account the effect of the non-negligible mass of the muons in the angular distributions. The lowest bin in q^2 has been extended down to 0.06 GeV$^2/c^4$. The effect of the muon mass is found to be significant up to $q^2 \simeq 6$ GeV$^2/c^4$, with the most pronounced effect at the lowest q^2 values. Second, it measures the complete set of interference terms of the P- and S-wave configurations.

The extracted CP-asymmetry observables show no significant deviations from zero, agreeing with the SM expectation, while the measurements of the CP-averaged observables and the branching fraction continue to exhibit the pattern of tensions with the Standard Model

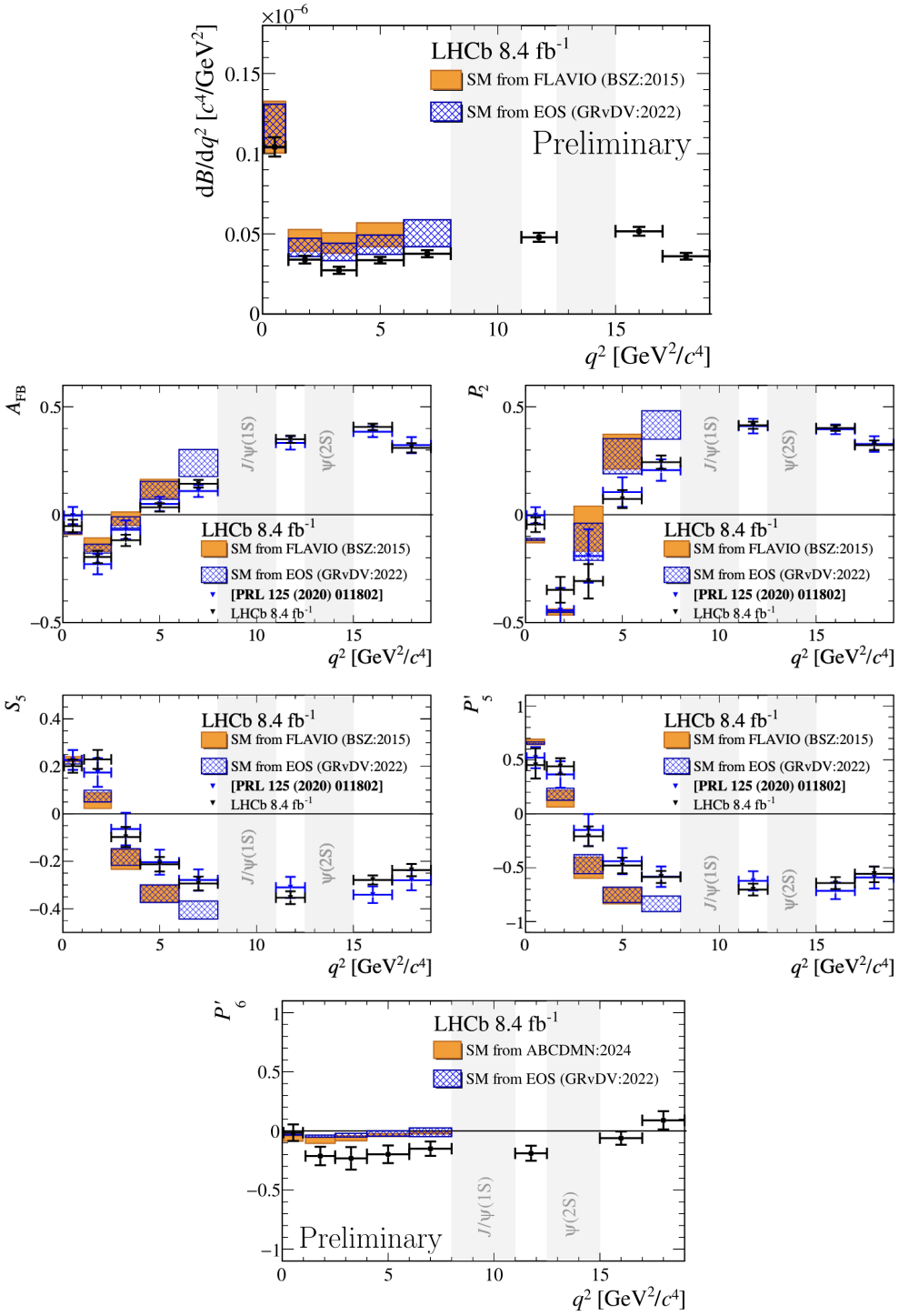

Figure 6.1.3: Selected results of the 2025 LHCb angular analysis of $B^0 \to K^{*0}\mu^+\mu^-$ decays.

predictions that have been seen in previous analyses. A selection of the results is shown in

Fig. 6.1.3, where the SM predictions are taken from references [106] (BSZ) and [10] (GRvDV), which only slightly changes the conclusions on the compatibility with the SM. Taking the BSZ prediction as reference, the local discrepancy in the $P_5^{'}$ observable for $q^2 \in [4.0, 6.0]$ GeV$^2/c^4$ and $q^2 \in [6.0, 8.0]$ GeV$^2/c^4$ increases with respect to the previous analysis to 2.7 and 3.1σ respectively. Additionally, $P_5^{'}$ is in tension with the SM prediction for $q^2 \in [1.1, 2.5]$ GeV$^2/c^4$ at the level of 2.8σ. For A_{FB}, the discrepancy also increases, at the level of 2.5 and 1.9σ for $q^2 \in [2.5, 4.0]$ GeV$^2/c^4$ and $q^2 \in [4.0, 6.0]$ GeV$^2/c^4$, respectively. Finally, the differential branching fraction is 2.0σ below the SM predictions for $q^2 \in [1.1, 6.0]$ GeV$^2/c^4$.

The Flavio [107] and EOS [108] software packages are used to fit the observables, varying the parameter $Re(C_9)$. The default values of the SM nuisance parameters are used, including form-factor parameters and subleading corrections to account for long-distance QCD interference effects with the charmonium decay modes [**?**, 106]. The discrepancy with respect to the SM value of $Re(C_9)$ increases to 3.6 σ (3.8 σ) with Flavio (EOS) with respect to the previous measurement. Including the differential branching fraction, the discrepancy goes up to 4.0 σ (4.1 σ). The best fit to the angular distribution is obtained with a shift in the SM value of $Re(C_9)$ by -0.94+0.21-0.17 (-0.92+0.23-0.23) with Flavio(EOS).

Complementary measurements of $b \to s\mu\mu$ decays in LHCb

There are complementary measurements of branching fractions and angular distributions of $b \to s\mu\mu$ decays that have been performed at LHCb. Some examples are provided below.

- The most precise measurements of the differential branching fractions of $B^+ \to K^+\mu^+\mu^-$, $B^0 \to K^0_S\mu^+\mu^-$, and $B^+ \to K^{*+}\mu^+\mu^-$ decays, as well as the isospin asymmetries of $B \to K\mu^+\mu^-$ and $B \to K^*\mu^+\mu^-$ decays, have been performed using a data set corresponding to 3 fb^{-1} of integrated luminosity [109]. The results on the isospin asymmetries are consistent with SM expectations, but the branching fraction measurements are consistently lower than the SM predictions, as also observed in $B^0 \to K^{*0}\mu^+\mu^-$.

- The complete pp data set collected with the LHCb experiment from 2011 to 2018 has then been used to measure for the first time the full set of angular observables for the decay $B^+ \to K^{*+}\mu^+\mu^-$ [110], confirming the global tension with respect to the SM predictions previously reported in the $B^0 \to K^{*0}\mu^+\mu^-$ decay.

- The most precise measurement of the branching fraction of the rare $B^0_s \to \phi\mu^+\mu^-$ decay using 9 fb^{-1}, shown in figure 6.4.2, is also found to lie below SM expectations for $q^2 \in [1.1, 6.0]$ GeV$^2/c^4$ [111]. The corresponding angular analysis of these decays provide results compatible with SM predictions [112].

In the end, there are no conclusive deviations from the SM predictions. However, these analyses complete the information on the FCNC studying different physics systems, sharing the same quark level transition but affected by different hadronic uncertainties. If the tensions in the $B^0 \to K^{*0}\mu^+\mu^-$ analysis is genuinely due to physics beyond the SM, it should also be observed in these decays when the analyses will be updated on larger datasets.

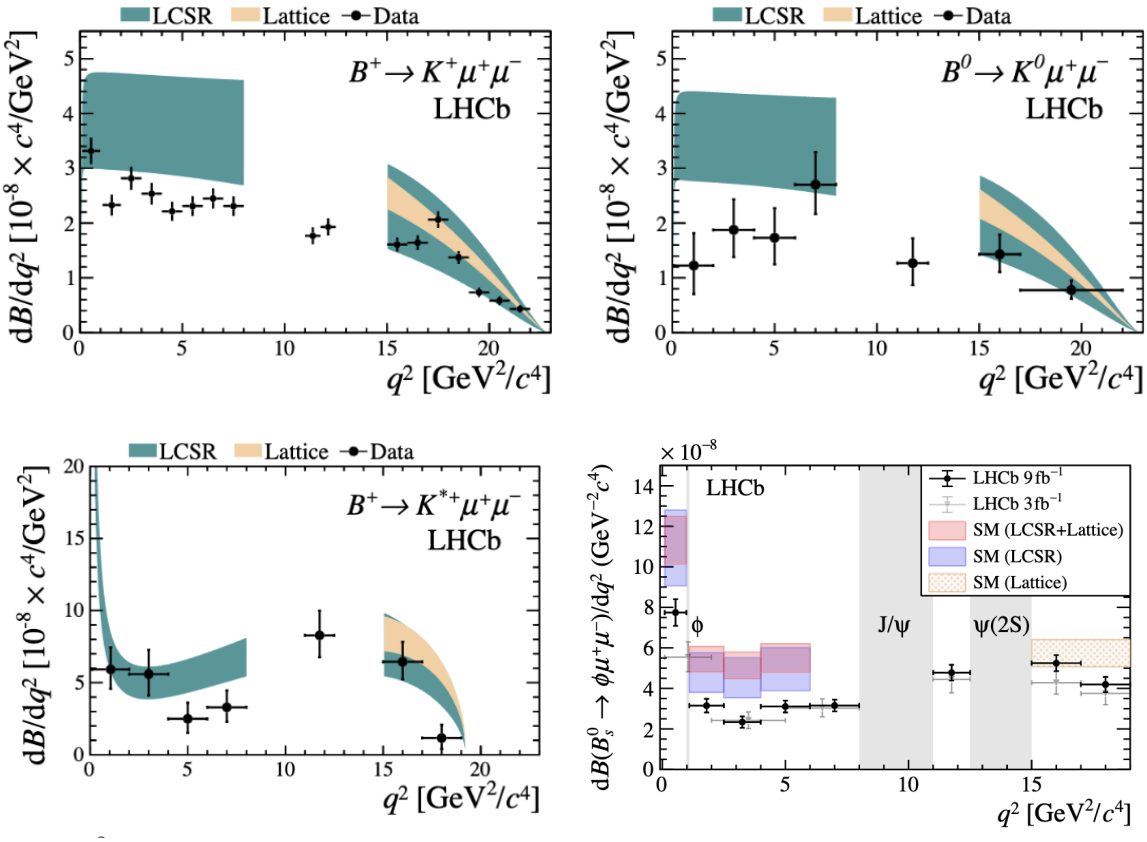

Figure 6.1.4: Differential branching fraction results for $B^+ \to K^+\mu^+\mu^-$, $B^0 \to K^0\mu^+\mu^-$, $B^+ \to K^{*+}\mu^+\mu^-$, and $B_s^0 \to \phi\mu^+\mu^-$ decays.

6.2 Status of $b \to s\ell\ell$ lepton flavor universality tests

The many lepton flavor universality (LFU) tests performed so far in $b \to s\ell\ell$ decays are summarized in table 6.2.1. In particular, the LHCb $R_{K^{*0}}$ measurement presented in this document has been updated in the context of a simultaneous analysis of the $B^+ \to K^+\ell^+\ell^-$ and $B^0 \to K^{*0}\ell^+\ell^-$ decays [113, 114], using 9 fb^{-1} collected between 2011 and 2018. The muon-mode signal decays for the B^+ and B^0 are experimentally independent, while this is not the case for the electron-mode signal decays due to their poorer mass resolution: partially reconstructed $B^0 \to K^{*0}e^+e^-$ decays represent a significant background to the $B^+ \to K^+e^+e^-$ decay. The simultaneous measurement allows this background to be determined directly from the observed yields of the signal $B^0 \to K^{*0}e^+e^-$ decay. The new analysis features improvements in the multivariate selections and stricter particle identification requirements, in particular aimed at reducing the expected rates for pions and kaons to be misidentified as electrons. Residual backgrounds due to misidentified hadronic decays are studied using data and included in the fit model. The trigger strategy is also optimized to improve the signal purity and to minimize the differences in trigger efficiency between electrons and muons.

Corrections to simulation, which account for imperfect modeling of the LHCb detector, are derived from the $B^0 \to K^{*0} J/\psi$ mode and applied to the charged rare mode, and analougously for the $B^+ \to K^+ J/\psi$ mode and the neutral rare mode. The two sets of corrections are shown to be interchangeable. All this leads to a higher signal purity, a better statistical sensitivity per unit luminosity and a more accurate estimate of systematic uncertainties than the previous analyses, giving more confidence in the results, shown in figure 6.2.1. The measurement of R_K at low q^2 is the first ever at LHCb, while the other results supersede the previous LHCb measurements. All of them are found to be compatible with the predictions of the Standard Model.

Other complementary lepton flavor universality tests have been performed in LHCb. One uses for the first time rare b-baryon decays, namely $\Lambda_b^0 \to pK^-\ell^+\ell^-$ with $\ell = e, \mu$ [115]. The interest of using baryons comes from the fact that the experimental uncertainties are different from lepton-universality tests performed with B mesons. For example, the backgrounds affecting the extraction of the signal yields and the control modes used to calibrate the simulation and measure the double ratio are different. The measurement is performed in the range $q^2 \in [0.1, 6]$ GeV$^2/c^4$ requiring $m(pK^-) < 2600$ MeV$/c^2$. Given the low abundance of the electron mode, to facilitate the error statistical treatment the quantity measured R_{pK}^{-1} is the ratio of the electron mode over the muon mode, rather than the opposite as in $R_{K^{*0}}$. The result is found to be $R_{pK}^{-1} = 1.17^{+0.18}_{-0.16} \pm 0.07$, compatible with unity within one standard deviation. The paper provides also the first measurement of the branching fraction of the rare muonic and electronic decay modes.

Additional LFU tests have used: $B^0 \to K_S^0 \ell^+\ell^-$ and $B^+ \to K^{*+}\ell^+\ell^-$ decays [116], obtaining results consistent with the SM at 1.5 and 1.4 standard deviations; $B^+ \to K^+\pi^+\pi^-\ell^+\ell^-$ decays [117], estabilishing a compatibility at the 1.7σ level; and $B_s^0 \to \phi\ell^+\ell^-$ decays [117], providing the first test of lepton flavour universality in the high-q^2 region in LHCb.

An additional LHCb measurement has been recently published for R_K in the high-q^2 region [118], performed using 9 fb^{-1} of data. The high q^2 measurement is of interest because

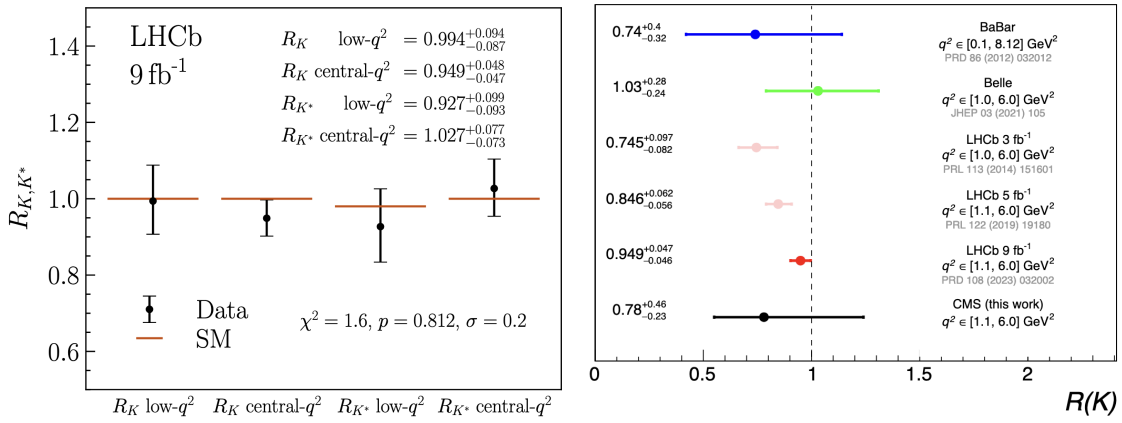

Figure 6.2.1: Left: results of the LHCb simultaneous LFU test on $B^+ \to K^+\ell^+\ell^-$ and $B^0 \to K^{*0}\ell^+\ell^-$ decays. Right: result of the CMS R_K measurement, compared with previous measurements.

Table 6.2.1: Summary of LFU measurements in b-hadron decays.

Decays	LFU test	q^2 range (GeV^2/c^4)	Experiment
$B^0 \to K^{*0}\ell^+\ell^-$	$R_{K^*} = 0.927^{+0.093+0.036}_{-0.087-0.035}$	$[0.1, 1.1]$	LHCb [113, 114]
	$R_{K^*} = 1.027^{+0.072+0.027}_{-0.068-0.026}$	$[1.1, 6.0]$	LHCb [113, 114]
$B^+ \to K^+\ell^+\ell^-$	$R_K = 0.994^{+0.090+0.029}_{-0.082-0.027}$	$[0.1, 1.1]$	LHCb [113, 114]
	$R_K = 0.949^{+0.042+0.022}_{-0.041-0.022}$	$[1.1, 6.0]$	LHCb [113, 114]
	$R_K = 1.08^{+0.11\ +0.04}_{-0.09\ -0.04}$	$q^2 > 14.3$	LHCb [118]
	$R_K = 0.78^{+0.47}_{-0.23}$	$[1.1, 6.0]$	CMS [119]
$B_s^0 \to \phi\ell^+\ell^-$	$R_\phi^{-1} = 1.57^{+0.28}_{-0.25} \pm 0.05$	$[0.1, 1.1]$	LHCb [120]
	$R_\phi^{-1} = 0.91^{+0.20}_{-0.19} \pm 0.05$	$[1.1, 6.0]$	LHCb [120]
	$R_\phi^{-1} = 0.85^{+0.24}_{-0.23} \pm 0.10$	$[15.0, 19.0]$	LHCb [120]
$B^+ \to K^+\pi^+\pi^-\ell^+\ell^-$	$R^{-1}_{K\pi\pi} = 1.31^{+0.18+0.12}_{-0.17-0.09}$	$[1.1, 7.0]$	LHCb [117]
$B^0 \to K_S^0\,\ell^+\ell^-$	$R_{K_S^0} = 0.66^{+0.20\ +0.02}_{-0.14\ -0.04}$	$[1.1, 6.0]$	LHCb [116]
$B^+ \to K^{*+}\ell^+\ell^-$	$R_{K^{*+}} = 0.70^{+0.18\ +0.03}_{-0.13\ -0.04}$	$[0.045, 6.0]$	LHCb [116]
$\Lambda_b^0 \to pK^-\ell^+\ell^-$	$R_{pK} = 0.86^{+0.14}_{-0.11} \pm 0.05$	$[0.1, 6.0]$	LHCb [115]

it has a dependence on both background and efficiency mismodelling which is complementary to measurements below the $\psi(2S)$. The result, compatible with the SM, is:

$$R_K(q^2 > 14.3\ \mathrm{GeV}^2/c^4) = 1.08^{+0.11}_{-0.09}\,(\mathrm{stat.})^{+0.04}_{-0.04}\,(\mathrm{syst.}).$$

A part from the Belle measurement cited previously, which is still affected by large statistical uncertainties, another relevant measurement has been provide by the CMS collaboration in 2024 [119]. This is the first test of lepton flavor universality by CMS, done using $B^\pm \to K^\pm\mu^+\mu^-$ and $B^\pm \to K^\pm e^+e^-$ decays, and also provide a measurement of differential and integrated branching fractions of the nonresonant $B^\pm \to K^\pm\mu^+\mu^-$ decay. The relevance of this result relies on the fact that the analysis has been made possible by a dedicated dataset of proton-proton collisions at $\sqrt{s} = 13$ TeV recorded in 2018, using a special high-rate data stream designed for collecting about 10 billion unbiased b-hadron decays. This work, therefore, demonstrated the flexibility of the CMS trigger and data acquisition system and paved the way to other studies of a large unbiased sample of b-hadron decays, including in final states with electrons. The ratio R_K has been measured for $q^2 \in [1.1, 6.0]$ GeV^2/c^4 and found to be $R(K) = 0.78^{+0.47}_{-0.23}$, in agreement with the SM expectation and other experiments as shown in figure 6.2.1.

6.3 Interpretation of $b \to s\ell\ell$ measurements.

As discussed above, while the tensions between theoretical predictions and experimental results in $b \to s\ell\ell$ lepton-flavor-universality tests have not been confirmed by recent measurements, deviations in the branching fraction and angular observables of $B^0 \to K^{*0}\mu^+\mu^-$ decays remain persistent. These anomalies have been observed by multiple experiments and across different hadronic systems.

The consistency tests of the experimental measurements with the SM actually show an increased level of discrepancy, driven by the improved precision of the latest LHCb angular analyses. The results of a recent global fit [121] are shown in Fig. 6.3.1. On the left, the most precise angular measurements from LHCb and CMS are combined, illustrating the level of deviation from SM predictions. On the right, all available constraints from other $b \to s\ell\ell$ and $b \to s\gamma$ observables are included. The resulting tension in the Wilson coefficient C_9 can exceed the 5σ level.

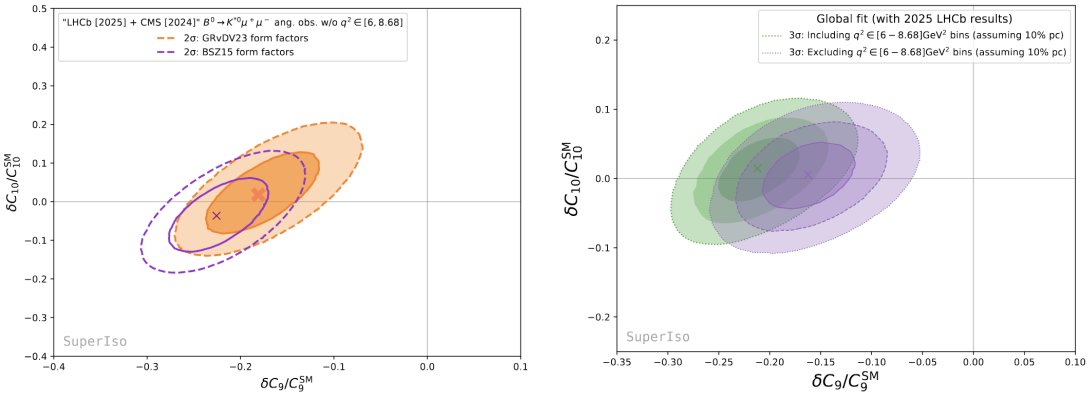

Figure 6.3.1: Result of SuperIso fit using: $B^0 \to K^{*0}\mu^+\mu^-$ angular measurements with two different form factors models (left); all experimental $b \to s\ell\ell$ and $b \to s\gamma$ observables.

This evidence is not sufficient to claim a discovery of new physics, as the origin of the observed tension remains unclear. As discussed previously, measurements of branching fractions and angular observables are affected by theoretical uncertainties, which can be broadly divided into two categories:

- **Local contributions:** these are related to the hadronic matrix elements and can be expressed in terms of form factors. They are calculated using QCD light-cone sum rules (LCSR) at low q^2, typically with uncertainties of 10–20%, and using lattice QCD (LQCD) at high q^2, and more recently also at low q^2, with a few-percent precision that is expected to improve further. Different form-factor determinations can significantly affect the magnitude of the observed discrepancy, as illustrated on the left of Fig. 6.3.1.

- **Non-local contributions:** these arise from the insertion of four-quark operators into the decay amplitude, where a photon is emitted and subsequently converts into the lepton pair. The relevant operators are $\mathcal{O}_1 = (\bar{s}_L^\alpha \gamma_\mu c_L^\beta)(\bar{c}_L^\beta \gamma^\mu b_L^\alpha)$ and $\mathcal{O}_2 = (\bar{s}_L \gamma_\mu c_L)(\bar{c}_L \gamma^\mu b_L)$, with α and β denoting color indices. In practice, these operators encode (i) non-perturbative effects from charm resonances, which appear when the lepton-pair invariant mass q^2 coincides with real hadronic intermediate states, and (ii) rescattering effects associated with triangle topologies. Both types of contributions, shown schematically in Fig. 6.3.2, are extremely challenging to calculate from first principles, as they receive non-perturbative corrections from soft-gluon emissions.

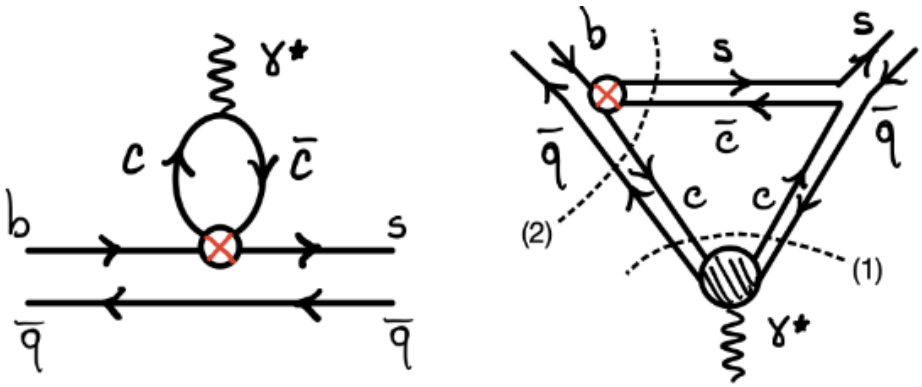

Figure 6.3.2: Charm loops (left) and rescattering topologies (right) contributing to $b \to s\ell\ell$ decays [122].

Although the tension with experimental data can be largely accommodated by a shift in C_9 relative to its SM value, such a shift could also arise from an incomplete or inaccurate description of the non-local matrix elements [122]. A definitive answer is expected to come from the lattice QCD calculation of these non-local contributions, in particular using a promising new approach based on spectral-density reconstruction [123]. However, this will take several years to complete.

In the meantime, LHCb has performed a dedicated unbinned amplitude analysis of the $B^0 \to K^{*0}\mu^+\mu^-$ decays to probe the non-local contributions directly from data [124]. In this analysis, the decay amplitudes are expressed analytically as functions of the Wilson coefficients $C_7^{(\prime)}$, $C_9^{(\prime)}$, $C_{10}^{(\prime)}$, as well as local and non-local hadronic matrix elements, which are determined simultaneously. The coefficients $C_7^{(\prime)}$ are bounded to the precise determinations in radiative B decays. The results of the fit are shown in Fig. 6.3.3. Remarkably, despite the large degrees of freedom introduced by the inclusion of non-local effects, the fit still prefers to accommodate the data through a shift in C_9 rather than through variations in the hadronic parameters. This preferred shift is consistent with results from global analyses of binned observables, although a mild dependence on the choice of local form-factor constraints is observed.

Another relevant consideration is that the effects of the non-local contributions are strongly q^2 dependent. Consequently, if the observed shift in C_9 were solely due to non-local effects, its extracted value should vary significantly when estimated using data from different q^2 bins. Phenomenological analyses have begun to perform this study, as illustrated in Fig. 6.3.4, but at present the experimental precision is insufficient to draw definitive conclusions.

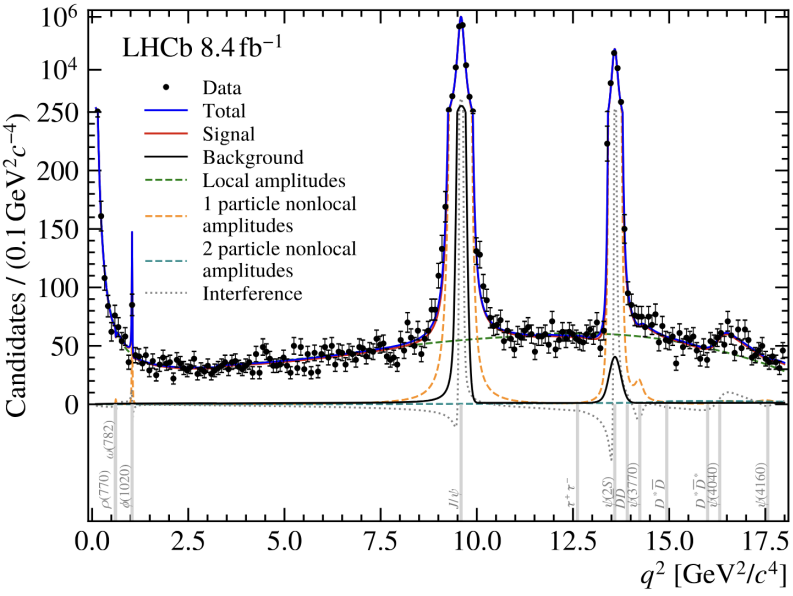

Figure 6.3.3: Unbinned amplitude fit of $B^0 \to K^{*0}\mu^+\mu^-$ decays [124].

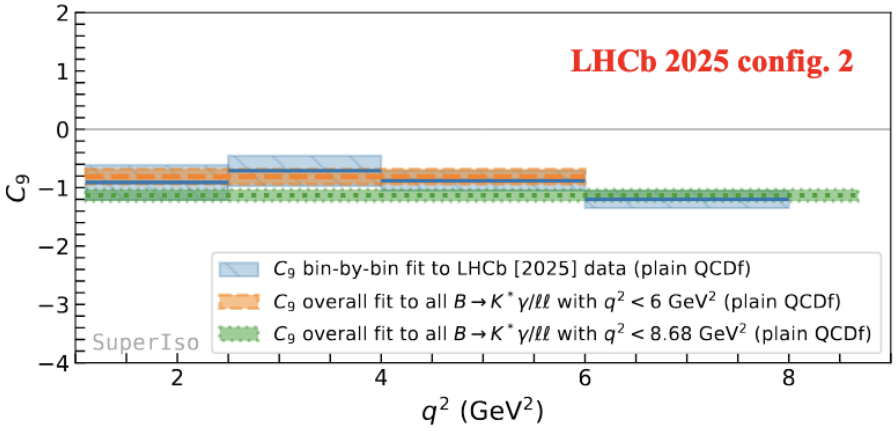

Figure 6.3.4: Test of q^2 dependence of the $\Delta(C_9)$ with SuperIso fit.

6.4 Prospects for $b \to s\ell\ell$ measurements.

Since 2022, the LHC has been delivering collisions at 13.6 TeV, the highest energy ever reached in a laboratory. After 2026, a new three-year shutdown is foreseen in order to proceed with a major upgrade, preparing for a further increase of the instantaneous luminosity. The LHCb detector, for its part, has undergone a complete overhaul and can now be considered as an entirely new experimental apparatus. It is equipped with a fully renewed tracking system, and benefits from improvements across all its sub-detectors, now equipped with fast

electronics operating at 40 MHz, synchronous with the collision frequency. The trigger system, entirely software-based, allows event reconstruction and selection at this same frequency, with a precision comparable to offline analyses, thanks to the new real-time calibration and alignment system. With these developments, LHCb can operate at higher instantaneous luminosity and therefore collect an unprecedented volume of data. By the end of 2025, it is expected that LHCb will have accumulated in this new phase a dataset equivalent to twice that collected during previous running periods. This substantial gain will considerably broaden the physics program, open the way to new searches, and achieve an unprecedented level of precision in several key measurements.

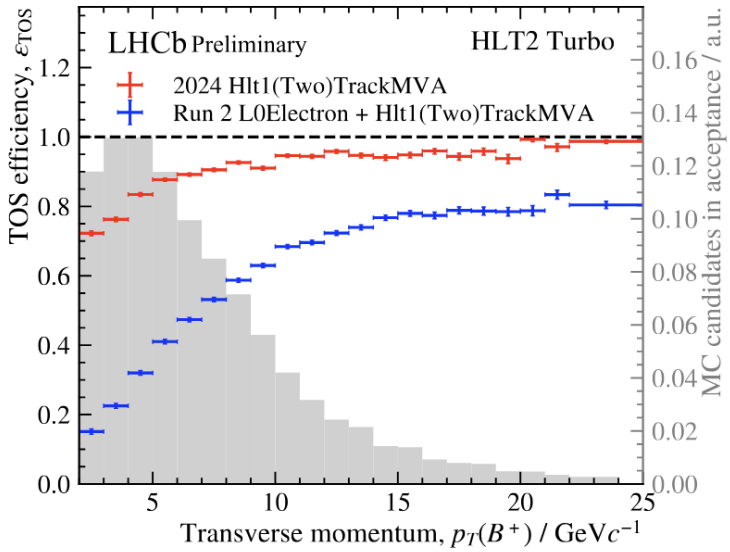

Figure 6.4.1: Comparison between the trigger efficiency in LHCb durin 2015-2018 (blu) and in the current LHCb upgrade (red), evaluated on 2024 data.

The analysis of data collected by LHCb since 2024 provides an excellent opportunity to deepen and expand angular analyses, tests of lepton-flavor universality, and searches for lepton-flavor-violating decays. Thanks to the recent upgrades of the experiment, improved signal reconstruction efficiencies are expected, particularly for final states containing electrons or τ leptons, which are crucial for many of these studies. This is illustrated for example in figure 6.4.1, showing a comparison of the trigger efficiency before and after the LHCb upgrade, as evaluated from data. The $B^0 \to K^{*0}\mu^+\mu^-$ measurements and also other decay channels may be measured in finer q^2 bins and with significantly improved precision. With more data, the $b \to d\ell\ell$ transitions are also becoming accessible, opening additional opportunities to test flavor physics and probe potential new physics effects. Prospects for the $P_5^{(\prime)}$ and LFU tests are shown, for example, in figure 6.4.2.

For the angular analysis of $B^0 \to K^{*0}\mu^+\mu^-$ decays, an increase in experimental precision would tend to disfavor new physics contributions if a q^2 dependence is observed. However, as discussed above, improvements in precision alone will not be conclusive without corresponding

advances in the theoretical predictions of non-local contributions from lattice QCD.

Additional results are also anticipated from CMS, which has demonstrated the effectiveness of its dedicated b-hadron trigger, as well as from ATLAS and, in particular, the Belle II experiment. Belle II has access to complementary flavor-changing neutral current channels, most notably $B^+ \to K^+\nu\bar{\nu}$ [125], for which it has recently reported evidence indicating a branching fraction currently larger than the SM prediction. Belle II is expected to collect up to 50 ab^{-1}, providing significant contributions to these studies. Together, CMS, ATLAS, and Belle II will provide valuable complementarity. In the longer term, the LHCb Upgrade II and a dedicated flavor program at a future circular collider, which would enable the study of $b \to s\tau^+\tau^-$ transitions, will ensure the continuation of this promising exploratory program.

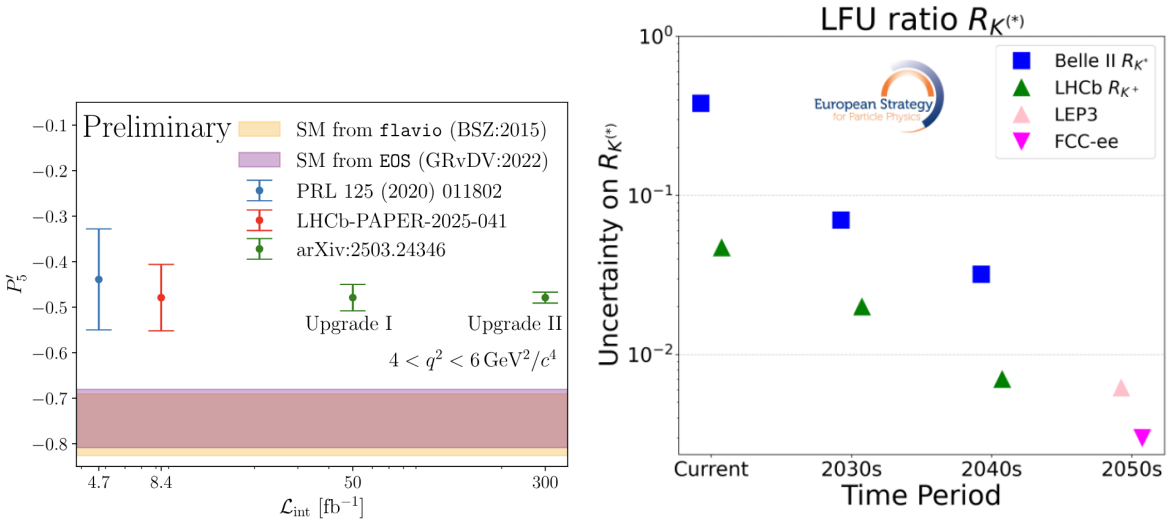

Figure 6.4.2: Left: Prospects for the P_5' LHCb measurement with the current and future upgrade of the detector. Right: prospects for $R_K^{(*)}$.

6.5 The landscape of charged lepton flavor violation

The lepton-flavor-violating searches presented in this document are at the moment providing the most stringent limits on $b \to se\mu$, $b \to s\tau\mu$ and $b \to s\tau e$ transitions. The $B^+ \to K^+\mu^\pm e^\mp$ analysis is currently being update by LHCb with additional data collected since 2015. The $B^0 \to K^{*0}\tau^\mp\mu^\pm$ and $B^0 \to K^{*0}\tau^\mp e^\pm$ are already using the full 9 fb^{-1} collected up to 2018. The next update will use data from the upgraded detector. A part from increased sensitivity coming from the use of a larger data set, additional analysis improvements are expected. In particular, searches with an electron will benefit from the more efficient electron trigger of the LHCb upgrade, shown in figure 6.4.1, which will reduce the previous penalty with respect to muon trigger. The $B^0 \to K^{*0}\tau^\mp\mu^\pm$ analysis should also profit from the fit mass approach developed for the $B^0 \to K^{*0}\tau^\mp e^\pm$ analysis.

Particle mediators responsible for lepton flavor violation in new physics models can have different lepton couplings, and there is not a specific golden channel: all modes covering all possible couplings must be explored. A broad experimental program investigates charged lepton flavor violation (CLFV) in muon, tau, and meson decays, as well as in interactions involving electroweak bosons, not only involving LHCb but many other ongoing or planned experiments.

The MEG experiment at PSI searched for the dipole-type process $\mu^+ \to e^+\gamma$, using a continuous muon beam and a high-resolution liquid-xenon calorimeter. It sets the current most stringent limit on this process. The upgraded MEG II apparatus improves the energy and timing resolutions and increases the muon stopping rate, targeting a sensitivity of about 6×10^{-14} [126]. The Mu3e experiment, also at PSI, searches for the three-body decay $\mu^+ \to e^+e^-e^+$, which probes four-fermion CLFV operators. Its ultra-light silicon tracker and high-intensity muon beam aim for sensitivities down to $\sim 10^{-15}$ in Phase I and $\sim 10^{-16}$ in Phase II [127].

Mu2e at Fermilab and COMET at J-PARC, instead, target coherent muon-to-electron conversion in the field of a nucleus, $\mu^- N \to e^- N$, a process sensitive to a wide variety of new-physics models, including heavy neutrinos, supersymmetry, and leptoquarks. Both employ pulsed proton beams and graded magnetic fields to suppress prompt backgrounds. Mu2e aims for a single-event sensitivity of 3×10^{-17} [128], while COMET Phase II will reach a similar level [129].

The BESIII detector at BEPCII investigates CLFV in charmonium decays such as $J/\psi \to e^\pm\mu^\mp$ and $J/\psi \to e^\pm\tau^\mp$, probing flavor violation simultaneously in the up-type quark and lepton sectors. Recent results constrain the branching ratios to the 10^{-7}–10^{-8} range [130].

Belle II is particular adapted for searches for CLFV in tau decays such as $\tau \to \mu\gamma$, $\tau \to 3\mu$, and $\tau \to e\gamma$, and competes with LHCb in searches in B-meson decays. With an ultimate integrated luminosity goal of 50 ab^{-1}, Belle II expects to improve current limits by one to two orders of magnitude, reaching sensitivities down to $\mathcal{B} \sim 10^{-9}$–10^{-10} [131].

Finally, the ATLAS and CMS detectors search for CLFV in tau, Higgs, and Z-boson decays such as $H \to \mu\tau$, $H \to e\tau$, and $Z \to e\mu$. These channels test flavor violation directly at the electroweak scale.

An overview of the most stringent experimental limits on various LFV channels is provided by the tables in this section, taken from [132]. In particular, Table 6.5.1 lists the current limits for B decays with $e\mu$, $\tau\mu$, and τe final states. The best experimental sensitivities are $\mathcal{O}(10^{-9})$ for $e\mu$ and $\mathcal{O}(10^{-6})$ for $\tau\mu$ and τe. Additional searches in other particle decays are summarized in Tables 6.5.2 and 6.5.3, the latter highlighting μ and τ decays where Belle II can achieve improved sensitivity.

Ongoing and future upgrades, along with the adoption of improved detector technologies and analysis techniques, will further enhance the experimental sensitivity to charged lepton flavor violation. For all such searches, it is important to establish a framework in which, alongside the experimental results, the detection efficiencies as functions of the relevant decay kinematics are provided, as exemplified by the analyses discussed in this paper. This approach ensures that the results can be readily recast in the context of various new physics models, whether currently proposed or developed in the future.

Leptons	Decay	Limit (90% C.L.)	Integrated luminosity	Experiment
$e\mu$	$B^0 \to e^{\mp}\mu^{\pm}$	1.0×10^{-9} [133]	$3fb^{-1}$	LHCb
	$B_s^0 \to e^{\mp}\mu^{\pm}$	5.4×10^{-9} [133]	$3fb^{-1}$	LHCb
	$B^0 \to \pi^0 e^{\mp}\mu^{\pm}$	1.4×10^{-7} [134]	472M BB ($426fb^{-1}$)	BaBar
	$B^+ \to \pi^+ e^{\mp}\mu^{\pm}$	1.7×10^{-7} [134]	472M BB ($426fb^{-1}$)	BaBar
	$B^0 \to K^0 e^{\mp}\mu^{\pm}$	3.8×10^{-8} [135]	772M BB ($771fb^{-1}$)	Belle
	$B^0 \to K^{*0} e^{\mp}\mu^{\pm}$	10.1×10^{-9} [136]	$9fb^{-1}$	LHCb
	$B^0 \to K^{*0} e^{-}\mu^{+}$	5.7×10^{-9} [136]	$9fb^{-1}$	LHCb
	$B^0 \to K^{*0} e^{+}\mu^{-}$	6.8×10^{-9} [136]	$9fb^{-1}$	LHCb
	$B^+ \to K^+ e^+ \mu^-$	7.0×10^{-9} [137]	$3fb^{-1}$	LHCb
	$B^+ \to K^+ e^- \mu^+$	6.4×10^{-9} [137]	$3fb^{-1}$	LHCb
	$B^+ \to K^{*+} e^- \mu^+$	9.9×10^{-7} [138]	472M BB ($426fb^{-1}$)	BaBar
	$B^+ \to K^{*+} e^+ \mu^-$	1.3×10^{-6} [138]	472M BB ($426fb^{-1}$)	BaBar
	$B^+ \to D^- e^+ \mu^+$	1.8×10^{-6} [139]	772M BB ($771fb^{-1}$)	Belle
	$B_s^0 \to \phi e^{\pm}\mu^{\mp}$	1.6×10^{-8} [136]	$9fb^{-1}$	LHCb
$\tau\mu$	$B^0 \to \tau^{\mp}\mu^{\pm}$	1.4×10^{-5} [140]	$3fb^{-1}$	LHCb
	$B_s^0 \to \tau^{\mp}\mu^{\pm}$	4.2×10^{-5} [140]	$3fb^{-1}$	LHCb
	$B^+ \to \pi^+ \tau^+ \mu^-$	4.5×10^{-5} [134]	472M BB ($426fb^{-1}$)	BaBar
	$B^+ \to \pi^+ \tau^- \mu^+$	2.45×10^{-5} [134]	472M BB ($426fb^{-1}$)	BaBar
	$B^0 \to K^{*0} \tau^+ \mu^-$	1.0×10^{-5} [141]	$9fb^{-1}$	LHCb
	$B^0 \to K^{*0} \tau^- \mu^+$	9.8×10^{-6} [141]	$9fb^{-1}$	LHCb
	$B^+ \to K^+ \tau^+ \mu^-$	5.9×10^{-6} [142]	772M BB ($771fb^{-1}$)	Belle
	$B^+ \to K^+ \tau^- \mu^+$	2.45×10^{-5} [142]	772M BB ($771fb^{-1}$)	Belle
	$B_s^0 \to \phi \tau^{\pm}\mu^{\mp}$	1.0×10^{-5} [143]	$9fb^{-1}$	LHCb
τe	$B^0 \to e^{\mp}\tau^{\pm}$	1.6×10^{-5} [144]	772M BB ($771fb^{-1}$)	Belle
	$B_s^0 \to e^{\mp}\tau^{\pm}$	1.4×10^{-3} [145]	772M BB ($771fb^{-1}$)	Belle
	$B^+ \to \pi^+ e^+ \tau^-$	7.4×10^{-5} [146]	472M BB ($426fb^{-1}$)	BaBar
	$B^+ \to \pi^+ e^- \tau^+$	2.0×10^{-5} [146]	472M BB ($426fb^{-1}$)	BaBar
	$B^+ \to K^+ e^+ \tau^-$	1.53×10^{-5} [147]	772M BB ($771fb^{-1}$)	Belle
	$B^+ \to K^+ e^- \tau^+$	1.51×10^{-5} [147]	772M BB ($771fb^{-1}$)	Belle
	$B^0 \to K^{*0} \tau^+ e^-$	5.9×10^{-6} [5]	$6fb^{-1}$	LHCb
	$B^0 \to K^{*0} \tau^- e^+$	4.9×10^{-6} [5]	$6fb^{-1}$	LHCb

Table 6.5.1: Searches for LFV B decays, classified by the presence of $e\mu$, $\tau\mu$ or τe in the final state.

Leptons	Decay	Limit	Experiment
$e\mu$	$\pi^0 \to e\mu$	3.6×10^{-10} [148] (90% C.L.)	KTeV
	$K^+ \to \pi^+\mu^+e^-$	1.3×10^{-11} [149] (90% C.L.)	BNL-E-0865
	$K^+ \to \pi^+\mu^-e^+$	6.6×10^{-11} [150] (90% C.L.)	NA62
	$K_L^0 \to e\mu$	4.7×10^{-12} [151] (90% C.L.)	BNL-E-0871
	$K_L^0 \to \pi^0 e\mu$	7.6×10^{-11} [148] (90% C.L.)	KTeV
	$K_L^0 \to \pi^0\pi^0 e\mu$	1.7×10^{-10} [148] (90% C.L.)	KTeV
	$J/\psi \to e\mu$	1.6×10^{-7} [152] (90% C.L.)	BES-III
	$D^+ \to \pi^+ e^+\mu^-$	2.1×10^{-7} [153] (90% C.L.)	LHCb
	$D^+ \to \pi^+ e^-\mu^+$	2.2×10^{-7} [153] (90% C.L.)	LHCb
	$D_s^+ \to \pi^+ e^+\mu^-$	1.1×10^{-6} [153] (90% C.L.)	LHCb
	$D_s^+ \to \pi^+ e^-\mu^+$	9.4×10^{-7} [153] (90% C.L.)	LHCb
	$D_s^+ \to K^+ e^-\mu^+$	5.6×10^{-7} [153] (90% C.L.)	LHCb
	$D^0 \to e^\pm\mu^\mp$	1.3×10^{-8} [154] (90% C.L.)	LHCb
	$D^0 \to \pi^0 e^\pm\mu^\mp$	8.0×10^{-7} [155] (90% C.L.)	BaBar
	$D^0 \to \eta e^\pm\mu^\mp$	2.25×10^{-6} [155] (90% C.L.)	BaBar
	$D^0 \to \omega e^\pm\mu^\mp$	1.71×10^{-6} [155] (90% C.L.)	BaBar
	$D^0 \to \rho e^\pm\mu^\mp$	5.0×10^{-7} [155] (90% C.L.)	BaBar
	$D^0 \to \phi e^\pm\mu^\mp$	5.1×10^{-7} [155] (90% C.L.)	BaBar
	$D^0 \to \bar{K}^0 e^\pm\mu^\mp$	1.74×10^{-6} [155] (90% C.L.)	BaBar
	$D^0 \to K^{*0} e^\pm\mu^\mp$	1.25×10^{-6} [155] (90% C.L.)	BaBar
	$D^0 \to \pi^+\pi^- e^\pm\mu^\mp$	1.71×10^{-6} [155] (90% C.L.)	BaBar
	$D^0 \to K^+K^- e^\pm\mu^\mp$	1.00×10^{-6} [155] (90% C.L.)	BaBar
	$D^0 \to \pi^+K^- e^\pm\mu^\mp$	1.90×10^{-6} [155] (90% C.L.)	BaBar
	$\Upsilon(1S) \to e^\pm\mu^\mp$	3.9×10^{-7} [156] (90% C.L.)	Belle
	$\Upsilon(1S) \to \gamma e^\pm\mu^\mp$	4.2×10^{-7} [156] (90% C.L.)	Belle
	$\Upsilon(3S) \to e^\pm\mu^\mp$	3.6×10^{-7} [157] (90% C.L.)	BaBar
	$Z \to e\mu$	2.62×10^{-7} [158] (95% C.L.)	ATLAS
	$H \to e\mu$	4.4×10^{-5} [159] (95% C.L.)	CMS
	$t \to e^\pm\mu^\mp u$	7×10^{-8} [160] (95% C.L.)	CMS
	$t \to e^\pm\mu^\mp c$	8.9×10^{-7} [160] (95% C.L.)	CMS
$\tau\mu$	$J/\psi \to \tau\mu$	2.0×10^{-6} [152] (90% C.L.)	BES
	$\Upsilon(1S) \to \tau^\pm\mu^\mp$	2.7×10^{-6} [156] (90% C.L.)	Belle
	$\Upsilon(1S) \to \gamma\tau^\pm\mu^\mp$	6.1×10^{-6} [156] (90% C.L.)	Belle
	$\Upsilon(2S) \to \tau^\pm\mu^\mp$	2.3×10^{-7} [161] (90% C.L.)	Belle
	$\Upsilon(3S) \to \tau^\pm\mu^\mp$	3.1×10^{-6} [162] (90% C.L.)	BaBar
	$Z \to \tau\mu$	6.5×10^{-6} [163] (95% C.L.)	ATLAS
	$H \to \tau\mu$	1.5×10^{-3} [164] (95% C.L.)	CMS
	$t \to \tau^\pm\mu^\mp q$	8.7×10^{-7} [165] (95% C.L.)	ATLAS
τe	$J/\psi \to e\tau$	7.5×10^{-8} [152] (90% C.L.)	BES-III
	$\Upsilon(1S) \to e^\pm\tau^\mp$	2.7×10^{-6} [156] (90% C.L.)	Belle
	$\Upsilon(1S) \to \gamma e^\pm\tau^\mp$	6.5×10^{-6} [156] (90% C.L.)	Belle
	$\Upsilon(2S) \to e^\pm\tau^\mp$	1.12×10^{-6} [161] (90% C.L.)	Belle
	$\Upsilon(3S) \to e^\pm\tau^\mp$	4.2×10^{-6} [162] (90% C.L.)	BaBar
	$Z \to e\tau$	5.0×10^{-6} [163] (95% C.L.)	ATLAS
	$H \to e\tau$	0.20% [166] (95% C.L.)	ATLAS
	$t \to \tau^\pm e^\mp q$	1.9×10^{-5} [167] (95% C.L.)	ATLAS

Table 6.5.2: Searches for LFV hadron decays other than B decays, classified by the presence of $e\mu$, $\tau\mu$ or τe in the final state.

Leptons	Decay	Limit (90% C.L.)	Experiment
μ decays	$\mu^+ \to e^+\gamma$	4.2×10^{-13} [168]	MEG
	$\mu^+ \to e^+e^-e^+$	1.0×10^{-12} [169]	SINDRUM
	$\mu^-N \to e^-N$	$6.1(7.1) \times 10^{-13}$ Ti(Au) [170]([171])	SINDRUM-II
	$\mu^-N \to e^-N'$	5.7×10^{-13} [172]	SINDRUM-II
τ decays	$\tau^\pm \to e^\pm\gamma$	3.3×10^{-8} [173]	BaBar
	$\tau^\pm \to \mu^\pm\gamma$	4.4×10^{-8} [173]	BaBar
	$\tau \to eee$	2.7×10^{-8} [174]	Belle
	$\tau \to \mu\mu\mu$	2.1×10^{-8} [174]	Belle
	$\tau \to \mu ee$	1.8×10^{-8} [174]	Belle
	$\tau \to e\mu\mu$	2.7×10^{-8} [174]	Belle
	$\tau \to e\pi\pi$	2.3×10^{-8} [175]	Belle
	$\tau \to \mu\pi\pi$	3.9×10^{-8} [175]	Belle
	$\tau \to e\pi K$	3.7×10^{-8} [175]	Belle
	$\tau \to \mu\pi K$	4.8×10^{-8} [175]	Belle
	$\tau \to eKK$	3.4×10^{-8} [175]	Belle
	$\tau \to \mu KK$	4.7×10^{-8} [175]	Belle
	$\tau \to eK_s^0K_s^0$	7.1×10^{-8} [176]	Belle
	$\tau^- \to e^-\pi^0$	8.0×10^{-8} [177]	Belle
	$\tau^- \to \mu^-\pi^0$	1.1×10^{-7} [178]	BaBar
	$\tau^- \to e^-K_s^0$	2.6×10^{-8} [176]	Belle
	$\tau^- \to \mu^-K_s^0$	2.3×10^{-8} [176]	Belle
	$\tau^- \to e^-\eta$	9.2×10^{-8} [177]	Belle
	$\tau^- \to \mu^-\eta$	6.5×10^{-8} [177]	Belle
	$\tau^- \to e^-\rho^0$	2.2×10^{-8} [179]	Belle
	$\tau^- \to \mu^-\rho^0$	1.7×10^{-8} [179]	Belle
	$\tau^- \to e^-\omega$	2.4×10^{-8} [179]	Belle
	$\tau^- \to \mu^-\omega$	3.9×10^{-8} [179]	Belle
	$\tau^- \to e^-K^{*0}$	1.9×10^{-8} [179]	Belle
	$\tau^- \to \mu^-K^{*0}$	2.9×10^{-8} [179]	Belle
	$\tau^- \to e^-\bar{K}^{*0}$	1.7×10^{-8} [179]	Belle
	$\tau^- \to \mu^-\bar{K}^{*0}$	4.3×10^{-8} [179]	Belle
	$\tau^- \to e^-\phi$	2.0×10^{-8} [179]	Belle
	$\tau^- \to \mu^-\phi$	2.3×10^{-8} [179]	Belle

Table 6.5.3: Searches for LFV decays of μ and τ leptons.

6.6 A research project for the future

The rich and variegated landscape of $b \to s\ell\ell'$ transitions described in this document is only a part of a much larger domain connecting the quark sector to the leptons. Various possibilities are available for performing studies that could hint to the effects of physics beyond the Standard Model and all of them are worth to be explored.

While angular analysis and lepton flavor universality tests of FCNC $b \to s\ell\ell$ decays are now well established in LHCb, another area not yet explored is currently attracting my interest. In the context of lepton flavor universality measurements $R_{D^{(*)}}$, there is a long standing tension in the flavor changing charged current $b \to s\ell\nu$ transitions. Figure 6.6.1 shows the current status of measurements and SM predictions. The compatibility is only at the level of 3.8 σ. This tension is quite puzzling, as it affects decays which are dominated by tree level transitions, and therefore expected to be less affected by NP. I plan to focus my effort in the coming years in complementary tests of lepton universality in $b \to u\ell\nu$ transitions, never performed so far. The objective is to achieve the first observation of the decays $B_s \to K^- e^+ \nu_e$ and $B_s \to K^- \tau^+ \nu_\tau$, and to measure the ratios of their branching fractions relative to the muon channel: $R_{K\tau\mu} = \mathcal{B}(B_s \to K^- \tau^+ \nu_\tau)/\mathcal{B}(B_s \to K^- \mu^+ \nu_\mu)$ and $R_{Ke\mu} = \mathcal{B}(B_s \to K^- e^+ \nu_e)/\mathcal{B}(B_s \to K^- \mu^+ \nu_\mu)$. LHCb is currently the only experiment in the world capable of collecting the required number of B_s mesons to perform these tests. From an analysis point of view, these decays always exhibit missing energy due to the neutrino emitted in b-quark transitions. In the absence of good resolution on the invariant mass of B_s candidates, it is essential to develop a fitting strategy based on multiple discriminating variables, in order to isolate the signal from the large expected background contributions. It would be interesting to see if these decays with kaons in the final state exhibit a similar deviation as observed in $R_{D^{(*)}}$. The study of the $B_s \to K^- e^+ \nu_e$ and $B_s \to K^- \tau^+ \nu_\tau$ decays will also provide new determinations of the CKM matrix element V_{ub}, which can be compared

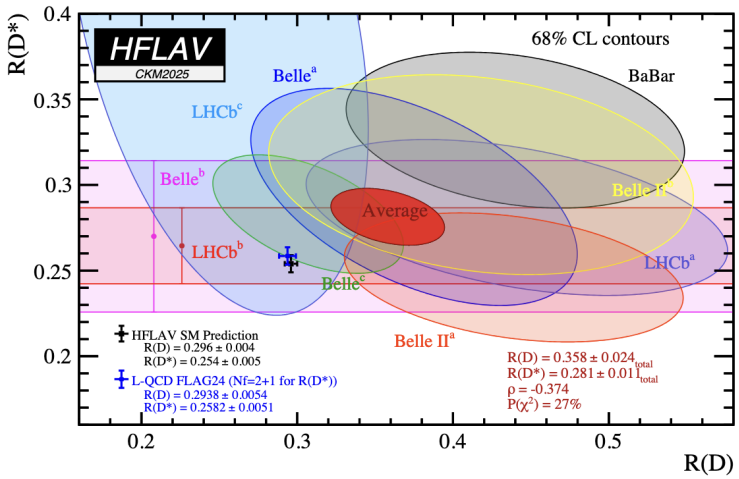

Figure 6.6.1: Status of R_D and R_{D^*} measurements and comparison with the theoretical prediction as of CKM2025. A tension with the SM at the level of 3.8 σ is observed.

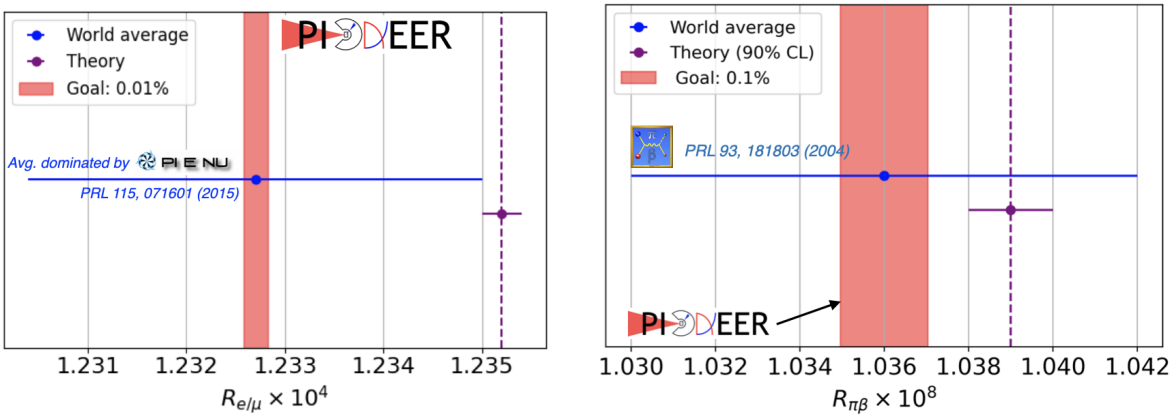

Figure 6.6.2: The PIONEER experiment physics goals. The expected precision is compared to the current measurements and to the SM predictions.

with those obtained in the $B_s \to K^- \mu^+ \nu_\mu$ channel and, combined, will contribute to the unitarity triangle test.

In parallel, I aim to establish a French participation in the PIONEER experiment planned at PSI [180], which focuses on the study of rare pion decays. This project addresses fundamental questions related to lepton universality and the unitarity of the CKM matrix, providing measurements complementary to those obtained by LHCb. As one of the most promising next-generation experiments for new physics discovery, PIONEER will significantly improve charged-pion rare-decay measurements (see figure 6.6.2) and perform pristine tests of lepton flavor universality and CKM unitarity. The PIONEER conceptual design foresees a high-intensity (300 kHz) beam of 65 MeV/c pions brought to rest in an active target (ATAR) surrounded by a high-density calorimeter with large acceptance. A tracker around the ATAR links hits in the target to calorimeter showers. The high data rate necessitates state-of-the-art triggering, fast digitizing electronics, and high-bandwidth data acquisition systems.

By measuring the charged-pion branching ratio to electrons versus muons, defined as $R_{e/\mu} = \frac{\Gamma(\pi^+ \to e^+ \nu)}{\Gamma(\pi^+ \to \mu^+ \nu)}$, at the 0.01% level, PIONEER will improve the current result by a factor of 15, matching the precision of the Standard Model prediction. This unprecedented sensitivity will allow exploration of potential modifications to weak interactions arising from new axial or pseudoscalar currents in ultraviolet-complete models, including extended gauge and Higgs sectors, heavy neutrinos, and dark-sector physics. The experiment will also improve the precision of the pion beta decay branching ratio, $\pi^+ \to \pi^0 e^+ \nu$, by a factor of six and extract the CKM matrix element V_{ud} in a theoretically clean environment, reaching an ultimate precision of 0.05%. This measurement enables a stringent test of the first-row CKM unitarity, which currently shows a 3σ tension, as illustrated in figure 6.6.3.

In the field of lepton-flavor-violation searches, increasingly stringent constraints are beginning to probe various new physics models proposed by the theoretical community. As null tests of the Standard Model that are not systematically limited, these searches merit further exploration, including a broader range of decay channels. I plan to update

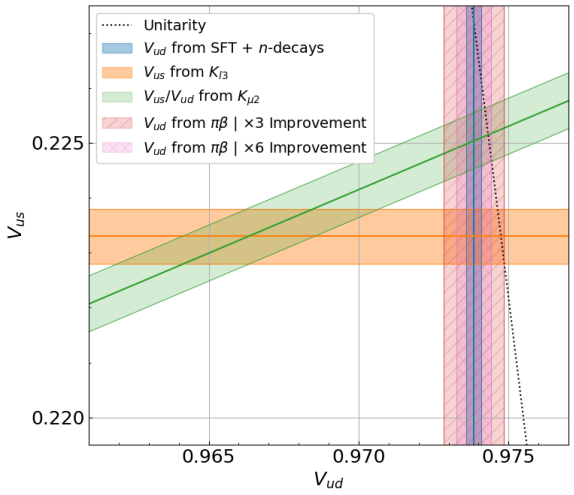

Figure 6.6.3: Illustration of the current tension in the unitarity of the first row of the CKM matrix.

the analyses of $B^0 \to K^{*0}\tau^{\pm}\mu^{\mp}$ and $B^0 \to K^{*0}\tau^{\pm}e^{\mp}$ decays. With the feasibility of these searches already demonstrated by initial publications, it will now be possible to exploit larger datasets, benefit from more efficient triggers, and apply improved event-selection techniques, thereby strengthening the limits on their branching fractions. To further increase sensitivity, a simultaneous analysis could set a limit on the $b \to s\tau\ell$ transitions ($\ell = e, \mu$), with the potential to extend this approach to other $b \to s\tau\ell$ decays.

Nature is telling us that the Standard Model is not the ultimate theory. Yet, it is working hard to hide new physics from our sight. In my opinion, a diversified approach is the key to unveiling the mysteries of nature, and I am proud and excited to keep contributing to this fascinating work of investigation.

Acknowledgements

This document describes the analysis work carried out at LHCb since I joined the collaboration at the end of 2011. As mentioned in the introduction, the work presented here would not have been possible without the students and postdocs I have had the pleasure to supervise: Samuel Coquereau, Andrea Mogini, Giulio Dujany, Steffen George Weber, and Tommaso Fulghesu. Alois Caillet and Andrea Campomagnani are now helping me to pursue my research projects at LHCb, and I would like to thank them as well for their collaboration. I also wish to thank the other LHCb collaborators who contributed to these analyses, with a special mention to Marie-Helene Schune, with whom I worked on the angular analysis and lepton flavor universality tests; her knowledge and dedication have been an invaluable resource.

I also wish to acknowledge the LHCb collaborators working daily on the detector, ensuring the successful data taking and processing. I had the opportunity to appreciate their competence and dedication while serving as operations coordinator of the experiment. Special thanks go to Silvia Gambetta, Elena Dall'Occo, Giovanni Cavallero, and Sascha Stahl for accompanying and supporting me in that role.

The LHCb group at LPNHE has long been a stimulating and enjoyable environment in which to work. The title of this manuscript is inspired by Eli Ben-Haim's HDR, "Beauty and the Dalitz plane", as a way to thank him for his support, guidance, and the friendship built over more than ten years of shared office.

Progress in this field would not be possible without fruitful exchanges with theoretical colleagues. As co-director of the GDR Intensity Frontier, I have had numerous discussions with theorists at many workshops. I wish to thank, in particular, Aoife Bharucha, who shared the co-direction with me for five years.

Finally, I would like to thank Quentin Buat for introducing me to the PIONEER experiment, and Pascal Vincent, who shares with me, with great enthusiasm, the supervision of LHCb students as well as this new project.

Bibliography

[1] LHCb collaboration, R. Aaij *et al.*, *Angular analysis of the $B^0 \to K^{*0}\mu^+\mu^-$ decay using $3\,fb^{-1}$ of integrated luminosity*, JHEP **02** (2016) 104, arXiv:1512.04442.

[2] LHCb collaboration, R. Aaij *et al.*, *Test of lepton universality with $B^0 \to K^{*0}\ell^+\ell^-$ decays*, JHEP **08** (2017) 055, arXiv:1705.05802.

[3] LHCb collaboration, R. Aaij *et al.*, *Search for the lepton-flavour violating decays $B^+ \to K^+\mu^\pm e^\mp$*, Phys. Rev. Lett. **123** (2019) 231802, arXiv:1909.01010.

[4] LHCb collaboration, R. Aaij *et al.*, *Search for the lepton flavour violating decay $B^0 \to K^{*0}\tau^\pm\mu^\mp$* , JHEP **06** (2023) 143, arXiv:2209.09846.

[5] LHCb collaboration, R. Aaij *et al.*, *Search for the lepton-flavour-violating decays $B^0 \to K^{*0}\tau^\pm e^\mp$*, arXiv:2506.15347, Submitted to JHEP.

[6] W. Altmannshofer *et al.*, *Symmetries and asymmetries of $B \to K^*\mu^+\mu^-$ decays in the Standard Model and beyond*, JHEP **01** (2009) 019, arXiv:0811.1214.

[7] P. Ball and R. Zwicky, *New results on $B \to \pi, K, \eta$ decay form factors from light-cone sum rules*, Phys. Rev. D **71** (2005) 014015, arXiv:hep-ph/0406232.

[8] P. Ball and R. Zwicky, *$B_{d,s} \to \rho, \omega, K^*, \phi$ decay form-factors from light-cone sum rules revisited*, Phys. Rev. D **71** (2005) 014029, arXiv:hep-ph/0412079.

[9] R. R. Horgan, Z. Liu, S. Meinel, and M. Wingate, *Lattice QCD calculation of form factors describing the rare decays $B \to K^*\ell^+\ell^-$ and $B_s \to \phi\ell^+\ell^-$*, Phys. Rev. D **89** (2014) 094501, arXiv:1310.3722.

[10] R. R. Horgan, Z. Liu, S. Meinel, and M. Wingate, *Rare b decays using lattice qcd form factors*, PoS LATTICE2014 (2015) 372, arXiv:1501.00367.

[11] M. Beneke, T. Feldmann, and D. Seidel, *Systematic approach to exclusive $B \to V\ell^+\ell^-, V\gamma$ decays*, Nucl. Phys. B **612** (2001) 25, arXiv:hep-ph/0106067.

[12] M. Beneke, T. Feldmann, and D. Seidel, *Exclusive radiative and electroweak $b \to d$ and $b \to s$ penguin decays at NLO*, Eur. Phys. J. C **41** (2005) 173, arXiv:hep-ph/0412400.

[13] M. Beneke and T. Feldmann, *Factorization of heavy-to-light form factors in soft-collinear effective theory*, Nucl. Phys. B **685** (2004) 249, arXiv:hep-ph/0311335.

[14] D. Melikhov and B. Stech, *Weak form factors for heavy meson decays: An Update*, Phys. Rev. D **62** (2000) 014006, arXiv:hep-ph/0001113.

[15] A. Faessler *et al.*, *The Exclusive rare decays $B \to K(K^*)\bar{\ell}\ell$ and $B_c \to D(D^*)\bar{\ell}\ell$ in a relativistic quark model*, Eur. Phys. J. direct **C4** (2002) 18, arXiv:hep-ph/0205287.

[16] C. Bourrely, I. Caprini, and L. Lellouch, *Model-independent description of $B \to \pi\ell\nu$ decays and a determination of $|V_{ub}|$*, Phys. Rev. D **79** (2009) 013008, arXiv:0807.2722.

[17] C. G. Boyd, B. Grinstein, and R. F. Lebed, *Precision corrections to dispersive bounds on form-factors*, Phys. Rev. D **56** (1997) 6895, arXiv:hep-ph/9705252.

[18] F. Krüger and J. Matias, *Probing new physics via the transverse amplitudes of $\overline{B}^0 \to \overline{K}^*(\to K^-\pi^+)\ell^+\ell^-$ at large recoil*, Phys. Rev. **D71** (2005) 094009, arXiv:hep-ph/0502060.

[19] S. Descotes-Genon, J. Matias, M. Ramon, and J. Virto, *Implications from clean observables for the binned analysis of $B \to K^*\mu^+\mu^-$ at large recoil*, JHEP **01** (2013) 048, arXiv:1207.2753.

[20] S. Schael et al. (ALEPH, DELPHI, L3, OPAL, SLD Collaborations), *Precision electroweak measurements on the z resonance*, Phys. Rept. **427** (2006) 257.

[21] G. Hiller and F. Krüger, *More model-independent analysis of $b \to s$ processes*, Phys. Rev. **D69** (2004) 074020, arXiv:hep-ph/0310219.

[22] C. Bobeth, G. Hiller, and G. Piranishvili, *Angular distributions of $\bar{B} \to \bar{K}\bar{\ell}\ell$ decays*, JHEP **12** (2007) 040, arXiv:0709.4174.

[23] C. Bouchard *et al.*, *Standard Model predictions for $B \to K\ell^+\ell^-$ with form factors from lattice QCD*, Phys. Rev. Lett. **111** (2013) 162002, arXiv:1306.0434.

[24] S. L. Glashow, D. Guadagnoli, and K. Lane, *Lepton flavor violation in B decays?*, Phys. Rev. Lett. **114** (2015) 091801, arXiv:1411.0565.

[25] LHCb collaboration, A. A. Alves Jr. *et al.*, *The LHCb detector at the LHC*, JINST **3** (2008) S08005.

[26] LHCb collaboration, R. Aaij *et al.*, *LHCb detector performance*, Int. J. Mod. Phys. **A30** (2015) 1530022, arXiv:1412.6352.

[27] R. Aaij *et al.*, *Performance of the LHCb Vertex Locator*, JINST **9** (2014) P09007, arXiv:1405.7808.

[28] R. Arink *et al.*, *Performance of the LHCb Outer Tracker*, JINST **9** (2014) P01002, arXiv:1311.3893.

[29] P. d'Argent *et al.*, *Improved performance of the LHCb Outer Tracker in LHC Run 2*, JINST **12** (2017) P11016, arXiv:1708.00819.

[30] M. Adinolfi *et al.*, *Performance of the LHCb RICH detector at the LHC*, Eur. Phys. J. **C73** (2013) 2431, arXiv:1211.6759.

[31] A. A. Alves Jr. *et al.*, *Performance of the LHCb muon system*, JINST **8** (2013) P02022, arXiv:1211.1346.

[32] R. Aaij *et al.*, *The LHCb trigger and its performance in 2011*, JINST **8** (2013) P04022, arXiv:1211.3055.

[33] R. Aaij *et al.*, *Performance of the LHCb trigger and full real-time reconstruction in Run 2 of the LHC*, JINST **14** (2019) P04013, arXiv:1812.10790.

[34] V. V. Gligorov and M. Williams, *Efficient, reliable and fast high-level triggering using a bonsai boosted decision tree*, JINST **8** (2013) P02013, arXiv:1210.6861.

[35] T. Likhomanenko *et al.*, *LHCb topological trigger reoptimization*, J. Phys. Conf. Ser. **664** (2015) 082025.

[36] T. Sjöstrand, S. Mrenna, and P. Skands, *A brief introduction to PYTHIA 8.1*, Comput. Phys. Commun. **178** (2008) 852, arXiv:0710.3820.

[37] I. Belyaev *et al.*, *Handling of the generation of primary events in Gauss, the LHCb simulation framework*, J. Phys. Conf. Ser. **331** (2011) 032047.

[38] D. J. Lange, *The EvtGen particle decay simulation package*, Nucl. Instrum. Meth. **A462** (2001) 152.

[39] N. Davidson, T. Przedzinski, and Z. Was, *PHOTOS interface in C++: Technical and physics documentation*, Comp. Phys. Comm. **199** (2016) 86, arXiv:1011.0937.

[40] I. M. Nugent *et al.*, *Resonance chiral lagrangian currents and experimental data for* $\tau^- \to \pi^-\pi^-\pi^+\nu_\tau$, Phys. Rev. **D88** (2013) 093012.

[41] Geant4 collaboration, J. Allison *et al.*, *Geant4 developments and applications*, IEEE Trans. Nucl. Sci. **53** (2006) 270; Geant4 collaboration, S. Agostinelli *et al.*, *Geant4: A simulation toolkit*, Nucl. Instrum. Meth. **A506** (2003) 250.

[42] M. Clemencic *et al.*, *The LHCb simulation application, Gauss: Design, evolution and experience*, J. Phys. Conf. Ser. **331** (2011) 032023.

[43] L. Anderlini *et al.*, *The PIDCalib package*, LHCb-PUB-2016-021, 2016.

[44] L. Breiman, J. H. Friedman, R. A. Olshen, and C. J. Stone, *Classification and regression trees*, Wadsworth international group, Belmont, California, USA, 1984.

[45] R. E. Schapire and Y. Freund, *A decision-theoretic generalization of on-line learning and an application to boosting*, Jour. Comp. and Syst. Sc. **55** (1997) 119.

[46] A. Blum, A. Kalai, and J. Langford, *Beating the hold-out: Bounds for k-fold and progressive cross-validation*, in *Proceedings of the Twelfth Annual Conference on Computational Learning Theory*, COLT '99, (New York, NY, USA), 203–208, ACM, 1999.

[47] M. Feindt and U. Kerzel, *The NeuroBayes neural network package*, Nucl. Instrum. Meth. **A559** (2006) 190.

[48] F. Beaujean, M. Chrzaszcz, N. Serra, and D. van Dyk, *Extracting angular observables without a likelihood and applications to rare decays*, Phys. Rev. **D91** (2015) 114012, arXiv:1503.04100.

[49] J. Gratrex, M. Hopfer, and R. Zwicky, *Generalised helicity formalism, higher moments and the $B \to K_{J_K}(\to K\pi)\bar{\ell}_1\ell_2$ angular distributions*, arXiv:1506.03970.

[50] A. Ali, P. Ball, L. T. Handoko, and G. Hiller, *A Comparative study of the decays $B \to (K, K^*)\ell^+\ell^-$ in standard model and supersymmetric theories*, Phys. Rev. **D61** (2000) 074024, arXiv:hep-ph/9910221.

[51] G. Kumar and N. Mahajan, *$B \to K^* l^+ l^-$: Zeroes of angular observables as test of standard model*, arXiv:1412.2955.

[52] BaBar collaboration, B. Aubert *et al.*, *Measurement of decay amplitudes of $B \to J/\psi K^*, \psi(2S)K^*$, and $\chi_{c1}K^*$ with an angular analysis*, Phys. Rev. **D76** (2007) 031102, arXiv:0704.0522.

[53] Belle collaboration, K. Chilikin *et al.*, *Observation of a new charged charmonium like state in $\bar{B}^0 \to J/\psi K^-\pi^+$ decays*, Phys. Rev. **D90** (2014) 112009, arXiv:1408.6457.

[54] LHCb collaboration, R. Aaij *et al.*, *Measurement of the polarization amplitudes in $B^0 \to J/\psi K^*(892)^0$ decays*, Phys. Rev. **D88** (2013) 052002, arXiv:1307.2782.

[55] D. Aston *et al.*, *A study of $K^-\pi^+$ scattering in the reaction $K^-p \to K^-\pi^+n$ at 11 GeV/c*, Nuclear Physics B **296** (1988) 493 .

[56] G. J. Feldman and R. D. Cousins, *Unified approach to the classical statistical analysis of small signals*, Phys. Rev. D **57** (1998) 3873, arXiv:physics/9711021.

[57] B. Sen, M. Walker, and M. Woodroofe, *On the unified method with nuisance parameters*, Statistica Sinica **19** (2009) 301.

[58] B. Efron, *Bootstrap methods: Another look at the jackknife*, Ann. Statist. **7** (1979) 1.

[59] U. Egede *et al.*, *New physics reach of the decay mode $\bar{B} \to \bar{K}^{*0}\ell^+\ell^-$*, JHEP **10** (2010) 056, arXiv:1005.0571.

[60] U. Egede, M. Patel, and K. A. Petridis, *Method for an unbinned measurement of the q^2-dependent decay amplitudes of $\overline{B}^0 \to \overline{K}^{*0}\mu^+\mu^-$ decays*, JHEP **06** (2015) 084, arXiv:1504.00574.

[61] C.-D. Lü and W. Wang, *Analysis of $B \to K_J^*(\to K\pi)\mu^+\mu^-$ in the higher kaon resonance region*, Phys. Rev. D **85** (2012) 034014, arXiv:1111.1513.

[62] LHCb collaboration, R. Aaij *et al.*, *Measurement of the $\overline{B}^0$–B^0 and $\overline{B}_s^0$–B_s^0 production asymmetries in pp collisions at $\sqrt{s} = 7$ TeV*, Phys. Lett. **B739** (2014) 218, arXiv:1408.0275.

[63] LHCb collaboration, R. Aaij *et al.*, *Measurement of the semileptonic CP asymmetry in B^0–$\overline{B}^0$ mixing*, Phys. Rev. Lett. **114** (2015) 041601, arXiv:1409.8586.

[64] LHCb collaboration, R. Aaij *et al.*, *Measurement of CP asymmetry in $D^0 \to K^-K^+$ and $D^0 \to \pi^-\pi^+$ decays*, JHEP **07** (2014) 041, arXiv:1405.2797.

[65] W. Altmannshofer and D. M. Straub, *New physics in $b \to s$ transitions after LHC Run 1*, Eur. Phys. J. **C75** (2015) 382, arXiv:1411.3161.

[66] S. Descotes-Genon, L. Hofer, J. Matias, and J. Virto, *On the impact of power corrections in the prediction of $B \to K^*\mu^+\mu^-$ observables*, JHEP **12** (2014) 125, arXiv:1407.8526.

[67] LHCb collaboration, R. Aaij *et al.*, *Measurement of form-factor-independent observables in the decay $B^0 \to K^{*0}\mu^+\mu^-$*, Phys. Rev. Lett. **111** (2013) 191801, arXiv:1308.1707.

[68] D. van Dyk *et al.*, *EOS ("delta456" release)*, doi: 10.5281/zenodo.159680.

[69] C. Bobeth, G. Hiller, D. van Dyk, and C. Wacker, *The decay $B \to K\ell^+\ell^-$ at low hadronic recoil and model-independent $\Delta B = 1$ constraints*, JHEP **01** (2012) 107, arXiv:1111.2558.

[70] A. Ali, G. Kramer, and G.-h. Zhu, *$B \to K^*\ell^+\ell^-$ decay in soft-collinear effective theory*, Eur. Phys. J. **C47** (2006) 625, arXiv:hep-ph/0601034.

[71] LHCb collaboration, R. Aaij *et al.*, *Test of lepton universality using $B^+ \to K^+\ell^+\ell^-$ decays*, Phys. Rev. Lett. **113** (2014) 151601, arXiv:1406.6482.

[72] Particle Data Group, C. Patrignani *et al.*, *Review of particle physics*, Chin. Phys. **C40** (2016) 100001.

[73] LHCb collaboration, R. Aaij *et al.*, *Measurements of the S-wave fraction in $B^0 \to K^+\pi^-\mu^+\mu^-$ decays and the $B^0 \to K^*(892)^0\mu^+\mu^-$ differential branching fraction*, JHEP **11** (2016) 047, Erratum ibid. **04** (2017) 142, arXiv:1606.04731.

[74] LHCb collaboration, A. A. Alves Jr. *et al.*, *The LHCb detector at the LHC*, JINST **3** (2008) S08005.

[75] D. Martínez Santos and F. Dupertuis, *Mass distributions marginalized over per-event errors*, Nucl. Instrum. Meth. **A764** (2014) 150, arXiv:1312.5000.

[76] K. S. Cranmer, *Kernel estimation in high-energy physics*, Comput. Phys. Commun. **136** (2001) 198, arXiv:hep-ex/0011057.

[77] LHCb collaboration, R. Aaij *et al.*, *Observation of $J/\psi p$ resonances consistent with pentaquark states in $\Lambda_b^0 \to J/\psi p K^-$ decays*, Phys. Rev. Lett. **115** (2015) 072001, arXiv:1507.03414.

[78] T. Skwarnicki, *A study of the radiative cascade transitions between the Upsilon-prime and Upsilon resonances*, PhD thesis, Institute of Nuclear Physics, Krakow, 1986, DESY-F31-86-02.

[79] B. Efron, *Bootstrap methods: Another look at the jackknife*, Ann. Stat. **7** (1979) 1.

[80] LHCb collaboration, R. Aaij *et al.*, *First observations of the rare decays $B^+ \to K^+\pi^+\pi^-\mu^+\mu^-$ and $B^+ \to \phi K^+\mu^+\mu^-$*, JHEP **10** (2014) 064, arXiv:1408.1137.

[81] D. Straub *et al.*, *flav-io/flavio v0.19*, doi: 10.5281/zenodo.292991.

[82] M. Pivk and F. R. Le Diberder, *SPlot: A Statistical tool to unfold data distributions*, Nucl. Instrum. Meth. A **555** (2005) 356, arXiv:physics/0402083.

[83] BaBar collaboration, J. P. Lees *et al.*, *Measurement of branching fractions and rate asymmetries in the rare decays $B \to K^{(*)}\ell^+\ell^-$*, Phys. Rev. **D86** (2012) 032012, arXiv:1204.3933.

[84] Belle collaboration, J.-T. Wei *et al.*, *Measurement of the differential branching fraction and forward-backward asymmetry for $B \to K^{(*)}\ell^+\ell^-$*, Phys. Rev. Lett. **103** (2009) 171801, arXiv:0904.0770.

[85] M. Bordone, G. Isidori, and A. Pattori, *On the Standard Model predictions for R_K and R_{K^*}*, Eur. Phys. J. **C76** (2016) 440, arXiv:1605.07633.

[86] S. Descotes-Genon, L. Hofer, J. Matias, and J. Virto, *Global analysis of $b \to s\ell\ell$ anomalies*, JHEP **06** (2016) 092, arXiv:1510.04239.

[87] B. Capdevila, S. Descotes-Genon, J. Matias, and J. Virto, *Assessing lepton-flavour non-universality from $B \to K^*\ell\ell$ angular analyses*, JHEP **10** (2016) 075, arXiv:1605.03156.

[88] B. Capdevila, S. Descotes-Genon, L. Hofer, and J. Matias, *Hadronic uncertainties in $B \to K^*\mu^+\mu^-$: a state-of-the-art analysis*, JHEP **04** (2017) 016, arXiv:1701.08672.

[89] N. Serra, R. Silva Coutinho, and D. van Dyk, *Measuring the breaking of lepton flavour universality in $B \to K^*\ell^+\ell^-$*, Phys. Rev. **D95** (2017) 035029, arXiv:1610.08761.

[90] D. van Dyk *et al.*, *EOS — A HEP program for flavor observables*, https://eos.github.io.

[91] A. Bharucha, D. M. Straub, and R. Zwicky, *$B \to V\ell^+\ell^-$ in the Standard Model from light-cone sum rules*, JHEP **08** (2016) 098, arXiv:1503.05534.

[92] W. Altmannshofer, C. Niehoff, P. Stangl, and D. M. Straub, *Status of the $B \to K^*\mu^+\mu^-$ anomaly after Moriond 2017*, arXiv:1703.09189.

[93] S. Jäger and J. Martin Camalich, *Reassessing the discovery potential of the $B \to K^* \ell^+ \ell^-$ decays in the large-recoil region: SM challenges and BSM opportunities*, Phys. Rev. **D93** (2016) 014028, arXiv:1412.3183.

[94] SLD collaboration, K. Abe *et al.*, *Measurement of the b quark fragmentation function in Z^0 decays*, Phys. Rev. **D65** (2002) 092006, arXiv:hep-ex/0202031, [Erratum: Phys. Rev. **D66** (2002) 079905].

[95] W. D. Hulsbergen, *Decay chain fitting with a Kalman filter*, Nucl. Instrum. Meth. **A552** (2005) 566, arXiv:physics/0503191.

[96] LHCb collaboration, R. Aaij *et al.*, *Measurement of the track reconstruction efficiency at LHCb*, JINST **10** (2015) P02007, arXiv:1408.1251.

[97] LHCb collaboration, R. Aaij *et al.*, *Measurement of the electron reconstruction efficiency at LHCb*, JINST **14** (2019) P11023, arXiv:1909.02957.

[98] Particle Data Group, P. A. Zyla *et al.*, *Review of particle physics*, Prog. Theor. Exp. Phys. **2020** (2020) 083C01.

[99] A. L. Read, *Presentation of search results: The CL_s technique*, J. Phys. **G28** (2002) 2693.

[100] G. Cowan, K. Cranmer, E. Gross, and O. Vitells, *Asymptotic formulae for likelihood-based tests of new physics*, Eur. Phys. J. **C71** (2011) 1554, arXiv:1007.1727, [Erratum: Eur. Phys. J. **C73** (2013) 2501].

[101] D. Bečirević, F. Jaffredo, J. P. Pinheiro, and O. Sumensari, *Lepton flavor violation in exclusive $b \to d \ell_i \ell_j$ and $b \to s \ell_i \ell_j$ decay modes*, Phys. Rev. **D110** (2024) 075004, arXiv:2407.19060.

[102] Belle collaboration, S. Wehle *et al.*, *Lepton-flavor-dependent angular analysis of $b \to k^* \ell^+ \ell^-$*, Phys. Rev. Lett. **118** (2017) 111801, arXiv:1612.05014.

[103] ATLAS Collaboration, M. Aaboud et al., *Angular analysis of $b_d^0 \to k^* \mu^+ \mu^-$ decays in pp collisions at $\sqrt{s} = 8$ TeV with the atlas detector*, JHEP **10** (2018) 047.

[104] CMS Collaboration, A. Hayrapetyan et al., *Angular analysis of the $b^0 \to k^*(892)^0 \mu^+ \mu^-$ decay in proton-proton collisions at $\sqrt{s} = 13$ TeV*, Phys. Lett. B **864** (2025) 139406.

[105] LHCb collaboration, R. Aaij *et al.*, *A comprehensive analysis of the decay $B^0 \to K^{*0} \mu^+ \mu^-$*, In preparation (2025) LHCb-PAPER-2025-041.

[106] A. Bharucha, D. M. Straub, and R. Zwicky, *$B \to v+$ in the standard model from light-cone sum rules*, Journal of High Energy Physics **2016** (2016) .

[107] D. M. Straub, *flavio: a python package for flavour and precision phenomenology in the standard model and beyond*, 2018.

[108] D. van Dyk *et al.*, *Eos: a software for flavor physics phenomenology*, The European Physical Journal C **82** (2022) .

[109] LHCb collaboration, R. Aaij *et al.*, *Differential branching fractions and isospin asymmetries of $B \to K^{(*)}\mu^+\mu^-$ decays*, JHEP **06** (2014) 133, arXiv:1403.8044.

[110] LHCb collaboration, R. Aaij *et al.*, *Angular analysis of the $B^+ \to K^{*+}\mu^+\mu^-$ decay*, Phys. Rev. Lett. **126** (2021) 161802, arXiv:2012.13241.

[111] LHCb collaboration, R. Aaij *et al.*, *Branching fraction measurements of the rare $B_s^0 \to \phi\mu^+\mu^-$ and $B_s^0 \to f_2'(1525)\mu^+\mu^-$ decays*, Phys. Rev. Lett. **127** (2021) 151801, arXiv:2105.14007.

[112] LHCb collaboration, R. Aaij *et al.*, *Angular analysis of the rare decay $B_s^0 \to \phi\mu^+\mu^-$*, JHEP **11** (2021) 043, arXiv:2107.13428.

[113] LHCb collaboration, R. Aaij *et al.*, *Measurement of lepton universality parameters in $B^+ \to K^+\ell^+\ell^-$ and $B^0 \to K^{*0}\ell^+\ell^-$ decays*, Phys. Rev. **D108** (2023) 032002, arXiv:2212.09153.

[114] LHCb collaboration, R. Aaij *et al.*, *Test of lepton universality in $b \to s\ell^+\ell^-$ decays*, Phys. Rev. Lett. **131** (2023) 051803, arXiv:2212.09152.

[115] LHCb collaboration, R. Aaij *et al.*, *Test of lepton universality using $\Lambda_b^0 \to pK^-\ell^+\ell^-$ decays*, JHEP **05** (2020) 040, arXiv:1912.08139.

[116] LHCb collaboration, R. Aaij *et al.*, *Tests of lepton universality using $B^0 \to K_S^0\ell^+\ell^-$ and $B^+ \to K^{*+}\ell^+\ell^-$ decays*, Phys. Rev. Lett. **128** (2022) 191802, arXiv:2110.09501.

[117] LHCb collaboration, R. Aaij *et al.*, *Test of lepton flavor universality with $B^+ \to K^+\pi^+\pi^-\ell^+\ell^-$ decays*, Phys. Rev. Lett. **134** (2025) 181803, arXiv:2412.11645.

[118] LHCb collaboration, R. Aaij *et al.*, *Measurement of the branching fraction ratio R_K at large dilepton invariant mass*, JHEP **07** (2025) 198, arXiv:2505.03483.

[119] CMS Collaboration, *Test of lepton flavor universality in $b^\pm \to k^\pm\mu^+\mu^-$ and $b^\pm \to k^\pm e^+e^-$ decays in proton-proton collisions at $\sqrt{s} = 13tev$*, Reports on Progress in Physics **87** (2024) 077802.

[120] LHCb collaboration, R. Aaij *et al.*, *Test of lepton flavour universality with $B_s^0 \to \phi\ell^+\ell^-$ decays*, Phys. Rev. Lett. **134** (2025) 121803, arXiv:2410.13748.

[121] T. Hurth, F. Mahmoudi, Y. Monceaux, and S. Neshatpour, *Data-driven analyses and model-independent fits for present $b \to s\ell\ell$ results*, 2025.

[122] M. Ciuchini *et al.*, *Constraints on lepton universality violation from rare b decays*, Phys. Rev. D **107** (2023) 055036.

[123] R. Frezzotti *et al.*, *Theoretical framework for lattice qcd computations of $b \to k\ell^+\ell^-$ and $\bar{B}_s \to \ell^+\ell^-\gamma$ decay rates, including contributions from "charming penguins"*, 2025.

[124] LHCb collaboration, R. Aaij *et al.*, *Comprehensive analysis of local and nonlocal amplitudes in the $B^0 \to K^{*0}\mu^+\mu^-$ decay*, JHEP **09** (2024) 026, Erratum ibid. **05** (2025) 208, arXiv:2405.17347.

[125] Belle II Collaboration, I. Adachi et al., *Evidence for $b^+ \to k^+\nu\overline{\nu}$ decays*, Phys. Rev. D **109** (2024) 112006, arXiv:2311.14647.

[126] The MEG II Collaboration, *The design of the meg ii experiment*, Eur. Phys. J. C **78** (2018) 380.

[127] The Mu3e Collaboration, *The mu3e experiment*, Nucl. Phys. B Proc. Suppl. (2020) .

[128] The Mu2e Collaboration, *Mu2e technical design report*, arXiv preprint (2014) arXiv:1501.05241.

[129] The COMET Collaboration, *Comet phase-i technical design report*, Prog. Theor. Exp. Phys. **2020** (2020) 033C01.

[130] The BESIII Collaboration, *Search for charged lepton flavor violation in $j/\psi \to e^\pm\mu^\mp$*, Phys. Rev. D **106** (2022) 072005.

[131] The Belle II Collaboration, *Prospects for charged lepton flavour violation searches in tau decays at belle ii*, Prog. Theor. Exp. Phys. (2024) 083C01.

[132] T. Fulghesu, *Search for Lepton Flavour violating decay$B0 \to K\star 0\tau \pm e$ with the LHCb experiment,contribution in Rare Decay trigger configuration andimplementation of isolation tools for the Upgrade of the detector*, theses, Sorbonne Université, 2024.

[133] LHCb collaboration, R. Aaij *et al.*, *Search for the lepton-flavour violating decays $B^0_{(s)} \to e^\pm\mu^\mp$*, JHEP **03** (2018) 078, arXiv:1710.04111.

[134] BaBar collaboration, B. Aubert *et al.*, *Search for the rare decay $B \to \pi l^+ l^-$*, Phys. Rev. Lett. **99** (2007) 051801, arXiv:hep-ex/0703018.

[135] BELLE collaboration, S. Choudhury *et al.*, *Test of lepton flavor universality and search for lepton flavor violation in $B \to K\ell\ell$ decays*, JHEP **03** (2021) 105, arXiv:1908.01848.

[136] LHCb collaboration, R. Aaij *et al.*, *Search for the lepton-flavour violating decays $B^0 \to K^{*0}\mu^\pm e^\mp$ and $B^0_s \to \phi\mu^\pm e^\mp$*, JHEP **06** (2023) 073, arXiv:2207.04005.

[137] LHCb collaboration, R. Aaij *et al.*, *Search for Lepton-Flavor Violating Decays $B^+ \to K^+\mu^\pm e^\mp$*, Phys. Rev. Lett. **123** (2019) 241802, arXiv:1909.01010.

[138] BaBar collaboration, B. Aubert *et al.*, *Measurements of branching fractions, rate asymmetries, and angular distributions in the rare decays $B \to K\ell^+\ell^-$ and $B \to K^*\ell^+\ell^-$*, Phys. Rev. **D73** (2006) 092001, arXiv:hep-ex/0604007.

[139] Belle collaboration, O. Seon *et al.*, *Search for Lepton-number-violating $B^+ \to D^- l^+ l'^+$ Decays*, Phys. Rev. D **84** (2011) 071106, arXiv:1107.0642.

[140] LHCb collaboration, R. Aaij *et al.*, *Search for the lepton-flavour-violating decays $B_s^0 \to \tau^\pm \mu^\mp$ and $B^0 \to \tau^\pm \mu^\mp$*, Phys. Rev. Lett. **123** (2019) 211801, arXiv:1905.06614.

[141] LHCb collaboration, R. Aaij *et al.*, *Search for the lepton-flavour violating decays $B^0 \to K^{*0} \tau^\pm \mu^\mp$*, JHEP **06** (2023) 143, arXiv:2209.09846.

[142] Belle collaboration, S. Watanuki *et al.*, *Search for the Lepton Flavor Violating Decays $B^+ \to K^+ \tau^\pm l^\mp (l = e, \mu)$ at Belle*, Phys. Rev. Lett. **130** (2023) 261802, arXiv:2212.04128.

[143] LHCb collaboration, R. Aaij *et al.*, *Search for the lepton-flavor violating decay $B_s^0 \to \phi \mu^\pm \tau^\mp$*, arXiv:2405.13103.

[144] Belle Collaboration, *Search for $B^0 \to \tau^\pm \ell^\mp$ ($\ell = e, \mu$) with a hadronic tagging method at Belle*, Phys. Rev. D **104** (2021) , arXiv:2108.11649.

[145] Belle collaboration, L. Nayak *et al.*, *Search for $B_s^0 \to \ell^\mp \tau^\pm$ with the Semi-leptonic Tagging Method at Belle*, JHEP **08** (2023) 178, arXiv:2301.10989.

[146] BaBar collaboration, *Search for the decay modes $B^\pm \to h^\pm \tau \ell$*, Phys. Rev. D **86** (2012) 012004.

[147] Belle Collaboration, *Search for the Lepton Flavor Violating Decays $B^+ \to K^+ \tau^\pm \ell^\mp$ ($\ell = e$, μ) at Belle*, Phys. Rev. Lett. **130** (2023) 261802.

[148] KTeV collaboration, E. Abouzaid *et al.*, *Search for lepton flavor violating decays of the neutral kaon*, Phys. Rev. Lett. **100** (2008) 131803, arXiv:0711.3472.

[149] A. Sher *et al.*, *An Improved upper limit on the decay $K^+ \to \pi^+ \mu^+ e^-$*, Phys. Rev. D **72** (2005) 012005, arXiv:hep-ex/0502020.

[150] NA62 collaboration, E. Cortina Gil *et al.*, *Search for Lepton Number and Flavor Violation in K^+ and π^0 Decays*, Phys. Rev. Lett. **127** (2021) 131802, arXiv:2105.06759.

[151] BNL collaboration, D. Ambrose *et al.*, *New limit on muon and electron lepton number violation from K0(L) —> mu+- e-+ decay*, Phys. Rev. Lett. **81** (1998) 5734, arXiv:hep-ex/9811038.

[152] BESIII collaboration, M. Ablikim *et al.*, *Search for the Lepton Flavor Violation Process $J/\psi \to e\mu$ at BESIII*, Phys. Rev. D **87** (2013) 112007, arXiv:1304.3205.

[153] LHCb collaboration, R. Aaij *et al.*, *Searches for 25 rare and forbidden decays of D^+ and D_s^+ mesons*, JHEP **06** (2021) 044, arXiv:2011.00217.

[154] LHCb collaboration, R. Aaij *et al.*, *Search for the lepton-flavour violating decay $D^0 \to e^\pm \mu^\mp$*, Phys. Lett. B **754** (2016) 167, arXiv:1512.00322.

[155] BaBar collaboration, J. P. Lees *et al.*, *Search for lepton-flavor-violating decays $D^0 \to X^0 e^{\pm}\mu^{\mp}$*, Phys. Rev. D **101** (2020) 112003, arXiv:2004.09457.

[156] Belle collaboration, S. Patra *et al.*, *Search for charged lepton flavor violating decays of Υ (1S)*, JHEP **05** (2022) 095, arXiv:2201.09620.

[157] BaBar collaboration, J. P. Lees *et al.*, *Search for Lepton Flavor Violation in $\Upsilon(3S) \to e^{\pm}\mu^{\mp}$*, Phys. Rev. Lett. **128** (2022) 091804, arXiv:2109.03364.

[158] ATLAS collaboration, G. Aad *et al.*, *Search for the charged-lepton-flavor-violating decay $Z \to e\mu$ in pp collisions at $\sqrt{s} = 13$ TeV with the ATLAS detector*, Phys. Rev. D **108** (2023) 032015, arXiv:2204.10783.

[159] CMS collaboration, A. Hayrapetyan *et al.*, *Search for the lepton-flavor violating decay of the Higgs boson and additional Higgs bosons in the $e\mu$ final state in proton-proton collisions at $\sqrt{s} = 13$ TeV*, Phys. Rev. D **108** (2023) 072004, arXiv:2305.18106.

[160] CMS collaboration, A. Tumasyan *et al.*, *Search for charged-lepton flavor violation in top quark production and decay in pp collisions at $\sqrt{s} = 13$ TeV*, JHEP **06** (2022) 082, arXiv:2201.07859.

[161] Belle collaboration, R. Dhamija *et al.*, *Search for charged-lepton flavor violation in $\Upsilon(2S) \to \ell^{\mp}\tau^{\pm}$ ($\ell = e, \mu$) decays at Belle*, JHEP **02** (2024) 187, arXiv:2309.02739.

[162] BaBar collaboration, J. P. Lees *et al.*, *Search for Charged Lepton Flavor Violation in Narrow Upsilon Decays*, Phys. Rev. Lett. **104** (2010) 151802, arXiv:1001.1883.

[163] ATLAS collaboration, G. Aad *et al.*, *Search for lepton-flavor-violation in Z-boson decays with τ-leptons with the ATLAS detector*, Phys. Rev. Lett. **127** (2022) 271801, arXiv:2105.12491.

[164] CMS collaboration, *Search for lepton-flavor violating decays of the Higgs boson in the $\mu\tau$ and $e\tau$ final states in proton-proton collisions at $\sqrt{s} = 13$ TeV pp collisions*, Physical Review D **104** (2021) .

[165] ATLAS collaboration, G. Aad *et al.*, *Search for charged-lepton-flavor violating $\mu\tau qt$ interactions in top-quark production and decay in pp collisions at s=13 TeV with the ATLAS detector at the LHC*, Phys. Rev. D **110** (2024) 012014, arXiv:2403.06742.

[166] ATLAS collaboration, G. A. et al. *Searches for lepton-flavour-violating decays of the higgs boson into $e\tau$ and $\mu\tau$ in $\sqrt{s} = 13$ tev pp collisions with the atlas detector*, Journal of High Energy Physics **2023** (2023) .

[167] C. A. Gottardo, *Search for charged lepton-flavour violation in top-quark decays at the LHC with the ATLAS detector*, PhD thesis, Bonn U., 2018, arXiv:1809.09048.

[168] The MEG Collaboration, *Search for the lepton flavour violating decay $\mu^+ \to e^+\gamma$ with the full dataset of the meg experiment*, Eur. Phys. J. C **76** (2016) 434.

[169] SINDRUM collaboration, U. Bellgardt *et al.*, *Search for the Decay $\mu^+ \to e^+e^+e^-$*, Nucl. Phys. B **299** (1988) 1.

[170] C. Dohmen *et al.*, *Test of lepton-flavour conservation in $\mu \to e$ conversion on titanium*, Physics Letters B **317** (1993) 631.

[171] SINDRUM II collaboration, W. H. Bertl *et al.*, *A Search for muon to electron conversion in muonic gold*, Eur. Phys. J. C **47** (2006) 337.

[172] J. Kaulard *et al.*, *Improved limit on the branching ratio of $\mu^- \to e^+$ conversion on titanium*, Physics Letters B **422** (1998) 334.

[173] BaBar collaboration, B. Aubert *et al.*, *Searches for Lepton Flavor Violation in the Decays $tau^\pm \to e^\pm\gamma$ and $tau^\pm \to \mu^\pm\gamma$*, Phys. Rev. Lett. **104** (2010) 021802, arXiv:0908.2381.

[174] K. Hayasaka *et al.*, *Search for Lepton Flavor Violating Tau Decays into Three Leptons with 719 Million Produced Tau+Tau- Pairs*, Phys. Lett. B **687** (2010) 139, arXiv:1001.3221.

[175] Belle collaboration, Y. Miyazaki *et al.*, *Search for Lepton-Flavor-Violating and Lepton-Number-Violating $\tau \to \ell hh'$ Decay Modes*, Phys. Lett. B **719** (2013) 346, arXiv:1206.5595.

[176] Belle collaboration, Y. Miyazaki *et al.*, *Search for Lepton Flavor Violating tau- Decays into \ell-K0s and \ell-K0sK0s*, Phys. Lett. B **692** (2010) 4, arXiv:1003.1183.

[177] Belle collaboration, Y. Miyazaki *et al.*, *Search for lepton flavor violating tau- decays into l- eta, l- eta-prime and l- pi0*, Phys. Lett. B **648** (2007) 341, arXiv:hep-ex/0703009.

[178] BaBar collaboration, B. Aubert *et al.*, *Search for Lepton Flavor Violating Decays $\tau^\pm \to \ell^\pm\pi^0$, $\ell^\pm\eta$, $\ell^\pm\eta'$*, Phys. Rev. Lett. **98** (2007) 061803, arXiv:hep-ex/0610067.

[179] Belle collaboration, N. Tsuzuki *et al.*, *Search for lepton-flavor-violating τ decays into a lepton and a vector meson using the full Belle data sample*, JHEP **06** (2023) 118, arXiv:2301.03768.

[180] PIONEER collaboration, W. Altmannshofer *et al.*, *PIONEER: Studies of Rare Pion Decays*, arXiv:2203. 01981 (2022) arXiv:2203.01981.